Hydrodynamic Lubrication with Magnetorheological Fluids

van der Meer, G.H.G.

DOI
10.4233/uuid:68482f82-5b95-4ba6-a579-e7ee479d9934

Publication date
2026

Document Version
Final published version

Citation (APA)
van der Meer, G. H. G. (2026). *Hydrodynamic Lubrication with Magnetorheological Fluids*. [Dissertation (TU Delft), Delft University of Technology]. https://doi.org/10.4233/uuid:68482f82-5b95-4ba6-a579-e7ee479d9934

Hydrodynamic Lubrication with Magnetorheological Fluids

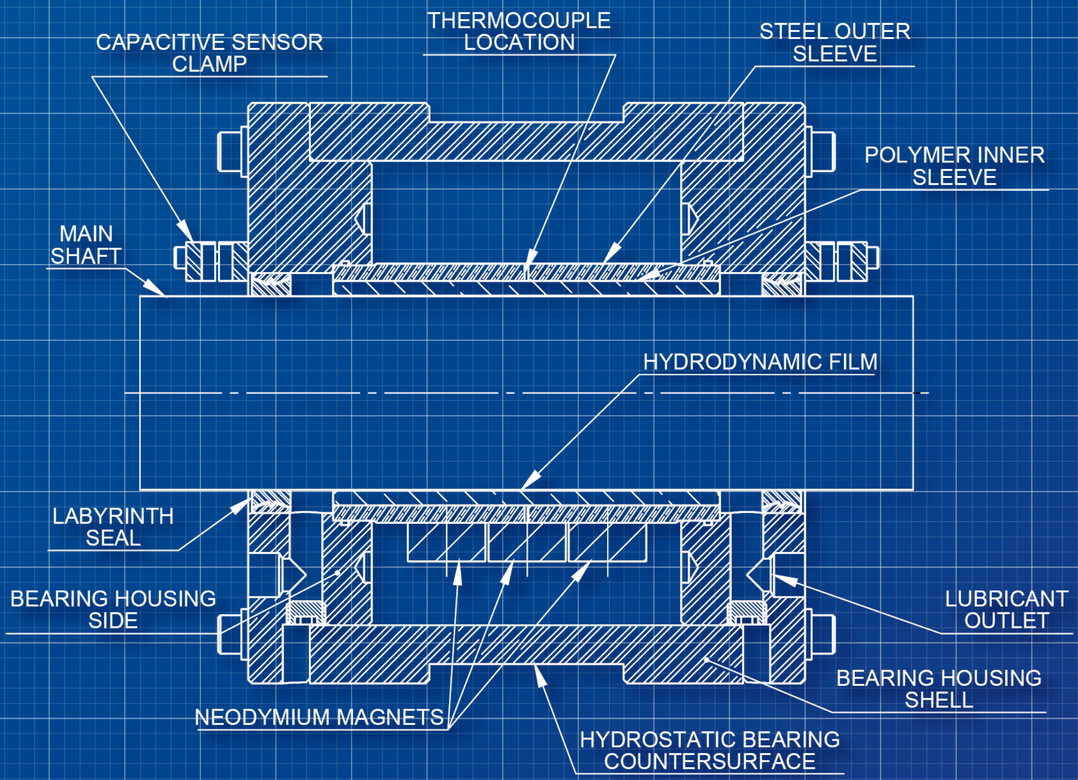

G.H.G. van der Meer

Hydrodynamic Lubrication with Magnetorheological Fluids

Dissertation

for the purpose of obtaining the degree of doctor
at Delft University of Technology
by the authority of the Rector Magnificus Prof. dr. ir. H. Bijl
Chair of the Board for Doctorates
to be defended publicly on
Wednesday 28 January 2026 at 12:30 o'clock

by

Gerben Hugo Geert VAN DER MEER

Master of Science in Mechanical Engineering,
Technische Universiteit Delft, Nederland,
born in Leiderdorp, Nederland.

This dissertation has been approved by the promotors.

Composition of the doctoral committee:

Rector Magnificus,	chairperson
Dr. ir. R.A.J. van Ostayen,	Technische Universiteit Delft, promotor
Prof. dr. ir. J.L. Herder,	Technische Universiteit Delft, promotor
Independent members:	
Prof. C.A. Dransfeld,	Technische Universiteit Delft
Dr. ir. W.P. Breugem,	Technische Universiteit Delft
Prof. dr. A. Almqvist,	Luleå University of Technology, Sweden
Prof. dr. ir. M.B. de Rooij,	Universiteit Twente
Prof. dr. ir. M. Langelaar,	Technische Universiteit Delft (reserve member)
Other members:	
Dr. hab.inż. M. Wodtke,	Gdańsk University of Technology, Poland

Keywords: magnetorheological fluid, lubrication, hydrodynamic journal bearing, Reynolds equation, shear-thinning, abrasive wear

Printed by:

Cover: Front - section view of the housing of the hydrodynamic bearing used in the experimental setup designed during the PhD. Back - technical drawing of one of the parts of the bearing housing

Style: TU Delft House Style, with modifications by Moritz Beller

ISBN 978-94-6384-888-6

Dit proefschrift is opgedragen aan oma en omi, voor hun liefde en steun.

Contents

Summary

Hydrodynamic journal bearings are typically used in pumps or motors to support rotating shafts with minimal added friction and wear. This is possible because the rotation of the shaft inside the stationary, lubricant-filled bearing causes a pressure build-up in that lubricant, which is capable of pushing the two bearing surfaces apart if the speed of the shaft is high enough (or if the radial load is low enough). However, at low speeds the bearing surfaces will remain in contact causing an increase in friction, and even worse, an increase in wear. Since the speed and load are generally determined by outside factors and cannot be selected for optimal bearing performance (a large container ship with a hydrodynamic bearing supporting the propeller shaft cannot enter a harbour at full speed), it is unavoidable that a hydrodynamic journal bearing will sometimes have to run under these unfavourable conditions. More viscous lubricant can be used to boost the pressure build-up, allowing the shaft to run at lower speeds before the bearing transitions to the high wear regime, but this will also increase friction and lead to a less efficient system.

A possible way around this issue could be the use of a magnetorheological (MR) fluid as lubricant. MR fluids are suspensions of iron microparticles which experience an increase in viscosity when magnetised. This process is fully reversible, effectively leading to a fluid with a controllable viscosity. Lubricating a bearing with this fluid could possibly allow the viscosity to be increased in the region of the bearing where most of the pressure is being generated, increasing the pressure build-up, while leaving the rest of the bearing demagnetised, thereby minimising the increase in friction. Alternatively, the bearing could be magnetised only at low speed or high load, when the increased viscosity is actually needed. With these concepts in mind, the main objective of this dissertation is to find out experimentally and numerically if MR-lubrication of a hydrodynamic journal bearing could improve its performance compared to standard lubricants.

The investigations described in this dissertation will show that the performance of an MR-lubricated bearing can indeed be switched from low friction at high speed, to more efficient pressure generation (and higher friction) at low speed by placing permanent magnets near the pressure generation region. The numerical model that has been developed also generally agrees with these experimental findings. It will also be shown that the performance of the tested MR-lubricated bearing is not clearly better than that of the reference bearing, and initial suspicions that the presence of the particles in the MR fluid would actually increase wear are confirmed as well. Experimental wear tests performed in collaboration with the university of Gdańsk have resulted in a selection of bearing sleeve materials with improved wear characteristics, though even then wear rates in the MR bearing remain somewhat larger. Based on all of these findings, magnetising an MR bearing with a constant magnetic field, independent of speed or load, does not result in improved performance. However, the results do seem to indicate that actively changing the magnetic field depending on the operating conditions (speed, load, etc...) could make the MR bearing much more competitive. Active magnetic field control is therefore recommended as a main focus for follow-up research.

Samenvatting

Hydrodynamische glijlagers worden vaak gebruikt in pompen of motoren om met minimale extra wrijving en slijtage de roterende as te ondersteunen. Dit is mogelijk omdat de rotatie van de as in het met smeermiddel gevulde lager (dat stil staat) een drukopbouw veroorzaakt in dat smeermiddel, waardoor de twee lageroppervlakken uit elkaar worden geduwd als de snelheid van de as hoog genoeg is (of als de radiale belasting laag genoeg is). Echter, bij lage snelheden blijven de lageroppervlakken in contact, wat leidt tot een toename van de wrijving en, nog ernstiger, een toename van slijtage. Aangezien snelheid en belasting meestal worden bepaald door externe factoren en niet kunnen worden gekozen voor optimale lagerprestaties (een groot containerschip met een hydrodynamisch lager dat de schroefas ondersteunt, kan niet met volle snelheid een haven binnenvaren), is het onvermijdelijk dat een hydrodynamisch glijlager soms onder deze ongunstige omstandigheden moet werken. Een meer viskeus (stroperiger) smeermiddel kan worden gebruikt om de drukopbouw te verhogen waardoor de as op lagere snelheid kan draaien voordat het in contact komt met het lager, maar dit zal ook de wrijving verhogen en zal leiden tot een minder efficiënt systeem.

Een mogelijke oplossing voor dit probleem zou het gebruik van een magnetoreologische (MR) vloeistof als smeermiddel kunnen zijn. Een MR-vloeistof is een suspensies van microdeeltjes ijzer waarvan de viscositeit toeneemt wanneer ze wordt gemagnetiseerd. Dit proces is volledig omkeerbaar, wat in feite leidt tot een vloeistof met een instelbare viscositeit. Het smeren van een lager met deze vloeistof zou het mogelijk kunnen maken om de viscositeit te verhogen in het gebied waar de meeste druk wordt gegenereerd, waardoor de drukopbouw zou toenemen, terwijl de rest van het lager gedemagnetiseerd blijft zodat de toename van wrijving wordt geminimaliseerd. Een andere optie is om het lager alleen te magnetiseren bij lage snelheid of hoge belasting, wanneer de verhoogde viscositeit daadwerkelijk nodig is om de lageroppervlakken uit elkaar te houden. Met deze concepten in het achterhoofd is het hoofddoel van dit proefschrift als volgt: het experimenteel en numeriek onderzoeken of MR-smering van een hydrodynamisch glijlager de prestaties kan verbeteren ten opzichte van standaard smeermiddelen.

Het onderzoek dat in dit proefschrift wordt beschreven toont aan dat de prestaties van een MR-gesmeerd lager inderdaad kunnen worden veranderd door de sterkte van het magnetisch veld in de buurt van het drukopbouwgebied te verhogen door middel van permanente magneten. Op deze manier verandert het typische gedrag van het lager van lage wrijving (bij hoge snelheid), naar efficiëntere drukopbouw (en hogere wrijving). Het ontwikkelde numerieke model komt over het algemeen ook overeen met deze experimentele bevindingen. Het is ook aangetoond dat de prestaties van het geteste MR-lager niet duidelijk beter zijn dan die van het referentielager, en daarnaast bevestigde deze tests het aanvankelijke vermoeden dat de aanwezigheid van de deeltjes in de MR-vloeistof de slijtage eigenlijk zou verhogen, in plaats van verlagen. Experimentele slijtagetests, uitgevoerd in samenwerking met de universiteit van Gdańsk, hebben geleid tot materialen

met verbeterde slijtage-eigenschappen, hoewel de slijtage in het MR-lager nog steeds iets hoger blijft. Op basis van al deze bevindingen moet worden geconcludeerd dat het magnetiseren van een MR-lager met een constant magnetisch veld, onafhankelijk van snelheid of belasting, niet leidt tot verbeterde prestaties. De resultaten lijken echter wel aan te geven dat het actief aanpassen van het magnetisch veld op basis van de bedrijfsomstandigheden (snelheid, belasting, etc.) het MR-lager veel interessanter zou kunnen maken. Actieve regeling van het magnetisch veld wordt daarom aanbevolen als een veelbelovende richting voor vervolgonderzoek.

1

Introduction

Bearings are machine elements that reduce friction between moving parts and they are found both in daily life and throughout industry, where they are used to improve the efficiency and reliability of all kinds of machines and devices. One specific type of bearing is the hydrodynamic journal bearing, which uses a thin film of oil to support a rotating shaft. These bearings are capable of bearing high loads at relatively low speeds while experiencing low friction and minimal wear. They are typically used in pumps or motors, and are frequently installed as stern tube bearings in ships, where they support the main shaft that connects the propeller to the engine [1]. These bearings are also being considered for use in wind turbines, since the currently used rolling element bearings cannot be scaled up indefinitely to support the increasingly larger size of these turbines [2].

Looking at the working principles of hydrodynamic journal bearings in more detail shows that the rotating shaft is contained in a (usually) stationary sleeve, with the two components separated from one another by a thin film of pressurised lubricant. This pressure is being generated by the combination of relative motion between the two bearing surfaces and the non-constant thickness of the film (see figure 1.1a). The limits of the performance of these journal bearing as a function of the operating conditions can be plotted in a Stribeck curve [3, 4], which is shown schematically in figure 1.1b. The Stribeck curve shows the friction in the hydrodynamic bearing as a function of the Hersey number, which is proportional with the dynamic fluid viscosity η and the rotational speed of the shaft n, and inversely proportional with the projected load $W/(L \cdot D)$ (with bearing length L and bearing diameter D). When the shaft and sleeve are fully separated by the fluid film the bearing is in the regime of hydrodynamic lubrication, which is characterised by low friction and minimal wear, and occurs when speeds are high or loads are low. Reducing the speed or increasing the load will decrease the minimum film thickness, until the first roughness peaks of the two bearing surfaces come into contact. At that point, the bearing transitions to mixed lubrication where load capacity is generated by both lubricant pressure and asperity contact, leading to increased friction. This is called the transition point. Continuing to lower speed or increase load will eventually lead to full contact between the bearing surfaces, which is called boundary lubrication and is characterised by high

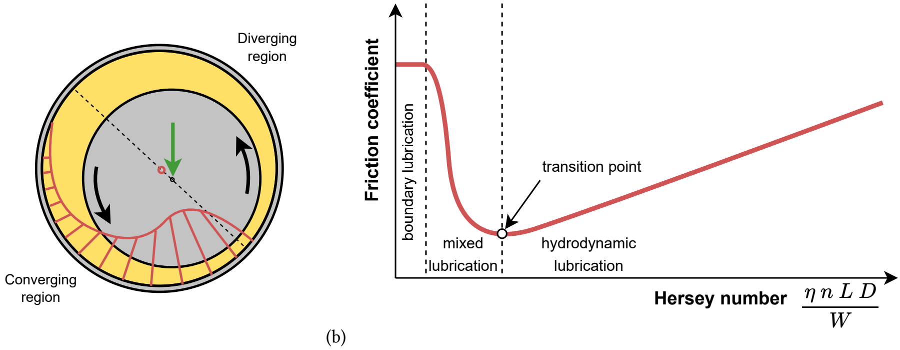

(a) (b)

Figure 1.1: The working principles of a hydrodynamic bearing explained: a) A schematic representation of a hydrodynamic journal bearing. The dotted line is drawn between the centre of the bearing sleeve (hollow red dot) and the centre of the shaft (solid black dot), the curved arrows indicate the direction of rotation of the shaft, and the vertical green arrow indicates the direction of the load on the shaft. On the left of the dotted line the fluid film converges, resulting in compression of the lubricant and the development of the pressure profile indicated in red. On the right side the film diverges, which under typical operating conditions will result in cavitation and therefore in pressures that are generally close to atmospheric pressure. The resulting asymmetric pressure profile provides a net upward force on the shaft, forming the load capacity of the bearing. b) A typical Stribeck curve which shows the friction coefficient as a function of the Hersey number. Note that the Stribeck curve can alternatively also be plotted as a function of just the shaft speed n, changing the transition point into a transition speed.

friction and wear. Clearly, a good hydrodynamic journal bearing should operate in the hydrodynamic regime for the majority of its lifespan, at Hersey numbers above the transition point, to maximise energy efficiency and minimise wear.

The range of loads and speeds for which the bearing should operate in the hydrodynamic regime is generally determined by the application, leaving the bearing geometry and lubrication selection to the designer. Over the years, there have been many developments on different geometries that optimise certain aspects of the bearing (examples are tilting pad bearings, bearings with non-circular bores, deformable bearings, etc... [3]), but while there has also been a lot of research on lubricants, the basic principle of lubricant selection has remained the same. The viscosity of the lubricant is a trade-off between the desired film thickness and an acceptable level of friction, and is generally considered to be a given quantity that varies with effects like temperature and pressure but cannot be changed once the lubricant has been chosen. Nonetheless, it can be imagined that there are advantages to having more control over the viscosity of the lubricant in the bearing. For example, figure 1.1a shows that most of the pressure that keeps the bearing surfaces apart is being generated near the bottom of the bearing. The lubricant at the top of the bearing (where the film thickness is largest) barely contributes to the pressure generation, but it does still increase the amount of friction. Perhaps a hypothetical bearing where the lubricant viscosity is larger near bottom of the bearing than at the top could have almost the same load capacity, but with lower friction. Another example, if a journal bearing usually operates at high speed (in the hydrodynamic regime), but sometimes also has to operate at low speed, it may be decided to use a relatively viscous lubricant to ensure the bearing is in the hydrodynamic regime at all times. This will minimise wear, but will result

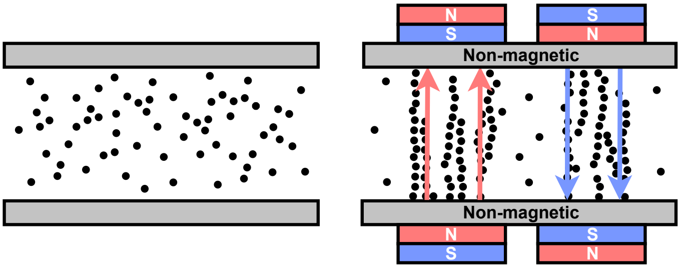

Figure 1.2: The formation of particle structures (chains) in an MR fluid contained between two non-magnetic surfaces. The figure on the left shows the unmagnetised suspension, the figure on the right the particle chains that are held in place by the uniform magnetic fields created by the magnets.

in higher friction during normal high-speed operation. A hypothetical bearing where the viscosity could be increased when the speed decreases could perhaps combine low friction at high speed with thick films at low speed. Obviously, neither of these two hypothetical bearings can be created with traditional Newtonian lubricating oils. But perhaps there are some options with an alternative lubricant. Magnetorheological fluids, also called MR fluids or MRFs, consist of a suspension of generally 20-30 vol% iron microparticles in a carrier fluid (frequently a mineral oil) [5, 6]. Under most circumstances, these fluids behave somewhat like most other suspensions, but when they are placed inside an external magnetic field they undergo a dramatic transformation. The magnetic field magnetises the particles, causing them to be attracted to one another and leading to the formation of particle structures (generally particle chains) along the magnetic field lines (see figure 1.2). This transformation occurs in only a few milliseconds and is completely reversible, removing the magnetic field will dissolve the particle structures and will lead to the original suspension. The presence of these structures has a large effect on the fluid rheology[1]. When the MR fluid is at rest, or experiences only a small amount of shear stress, the structures are actually strong enough to trap the carrier fluid in between themselves, which at a macro scale causes the MR fluid to seemingly become a solid. In this state, the MR fluid is sometimes represented with a viscoelastic or viscoplastic model, but more commonly it is simply seen as a solid with a yield stress [11], with the yield stress being the minimum shear stress required for the carrier fluid to start moving through the structures. Once large enough shear stresses have caused the carrier fluid to start moving, the structures still impede its flow, resulting in an increase of the apparent viscosity at a macro scale (compared to the unmagnetised state of the MR fluid). The magnitude of this increase scales with the strength of the applied magnetic field and decreases the stronger the fluid is being sheared, since the growing hydrodynamic forces on the particle structures will cause their gradual breakdown, bringing more and more particles back into suspension [12]. This effect makes an MR fluid strongly shear-thinning, which is shown in the viscos-

---

[1] MR fluids should not be confused for ferrofluids, which are colloidal suspensions of iron nanoparticles that generally do not experience a change in rheology when magnetised [7, 8]. However, it is important to realise that whether or not a suspension of magnetisable particle can change its rheology does not only depend on the particle size, but also on aspects like particle concentration and the strength of the external magnetic field [9, 10].

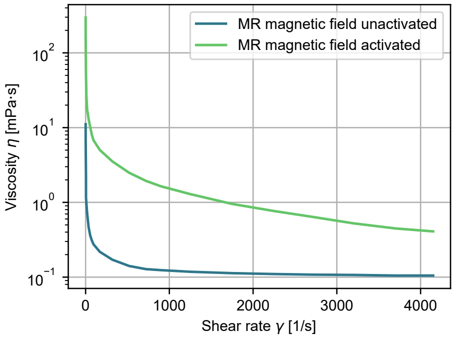

Figure 1.3: Viscosity as a function of shear rate for a representative MR fluid with and without an external magnetic field applied to it. It is clear that the MR fluid is strongly shear-thinning under all circumstances, even when not magnetised. This is caused by the inclusion of thixotropic (shear-thinning) anti-sedimentation additives, used because of the density mismatch between iron and oil [13–15].

ity plot in figure 1.3.

This unique variable rheology of MR fluids has led to research into to several applications. In the past, MR fluids have mostly been used in low shear situations, where the viscosity increase due to the magnetic field is largest. This has for example resulted in MR clutches, brakes, and dampers [16], with the latter having found use in the suspension of high-end cars [17, 18]. Other applications such as MR force-feedback devices or magnetorheological elastomers have also gotten some interest [19], as well as the use of MR fluids as lubricant in hydrodynamic bearings. As was hinted at earlier, the potential to change the viscosity of the lubricant inside the bearing with a variable that is independent from the normal operation of the bearing (a magnetic field) is very enticing.

1.1 Problem statement

In spite of the potential of a hydrodynamic bearing with variable fluid film viscosity, the body of work on MR-lubricated bearings is relatively small and almost all research evaluates journal bearings where an attempt is made to magnetise the entire fluid film, which is then compared with the unmagnetised bearing and/or the same bearing lubricated with oil. Both numerical [20–24] and experimental [25–29] papers have been published, and in general the conclusions are the same: when magnetised, the bearing shows thicker films/higher load capacity (and sometimes higher stiffness and damping is mentioned), but also (significantly) increased hydrodynamic friction at high speeds. In the opinion of the author these results are not all that exciting, it is clear that magnetised MR fluid has high viscosity even when used as a lubricant, and this has the expected effect of increasing film thickness and friction. But by magnetising the entire fluid film at all times the main distinguishing feature of MR lubrication, the possibility of varying viscosity at different locations in the bearing films, or as a function of the operating conditions, is not used to the fullest. There has been one attempt to locally magnetise an MR-lubricated journal bearing near minimum film, but the resulting bearing still showed very high friction (and very thick films) [30]. Other than this one paper however, the author of this dissertation knows of no attempts to properly explore the possibilities offered by MR lubrication, or attempts to show whether MR lubrication can be a practical alternative (with acceptable friction) to lubrication with standard lubricating oils.

1.2 Research objectives

The main objective of this dissertation is to investigate (both numerically and experimentally) the use of MR fluid as a lubricant for hydrodynamic journal bearings, with the aim of discovering whether MR lubrication can offer improved performance compared to traditional lubricating oils. In this context performance refers to the ability of the bearing to generate thick films (or low transition speeds) with low high-speed hydrodynamic friction, and it will be used in this capacity throughout the dissertation. Note the mention of 'transition speeds' instead of 'transition points' (which were introduced in figure 1.1b). Since MR fluids are shear-thinning and the shear stress varies throughout the film of a journal bearing, the viscosity of an MR film will vary throughout the bearing even when unmagnetised. The Hersey number, which is calculated with a single value for the viscosity in the entire bearing, is therefore no longer well defined. As a result, the rest of this dissertation will show Stribeck curves as a function of the shaft speed n only, changing the transition point into a transition speed.

There seem to be two promising options for starting the investigation into MR lubrication, either using local magnetisation of the fluid film, or (full) magnetisation as a function of the operating conditions (active control). Local magnetisation may be more interesting to start with since it has the potential to passively reduce friction (compared to literature) with minimal effect on the film thickness. Therefore, local magnetisation will be investigated first, leaving active control as an option to investigate later. Next to this, there are some other aspects of MR lubrication that will require attention. The first is the non-Newtonian shear-thinning nature of an MR fluid, which makes it difficult to predict the behaviour of the bearing with standard Newtonian Reynolds equation–based models. Similar models that incorporate the effects of shear-dependent viscosity do exist, but are more computationally complex and therefore take much longer to run (minutes instead of seconds). Making such a model more computationally efficient would make it easier to design interesting experiments, and would allow for larger scale optimisation studies. The second aspect that requires attention is wear of the bearing due to MR lubrication. It is to be expected that lubricating a bearing with a fluid containing hard microparticles will lead to increased (abrasive) wear, and there is some experimental evidence that this is indeed the case [30]. It is therefore necessary to investigate the severity of wear due to MR lubrication, and to find methods of mitigating this additional wear if needed. Finally, with an initial experimental result showing the feasibility of local magnetisation, with a fast model, and with an acceptable level of wear, it will be possible to start an in-depth investigation into optimal magnetic fields to apply to MR-lubricated bearings, hopefully answering the main question about which improvements MR lubrication can offer over oil lubrication.

In summary, several research objectives have been formulated to work towards the main objective, with a focus on investigating potential issues and on exploring the unique capabilities of a lubricant consisting of a magnetically activated suspension of hard particles:

1. Minimise the friction increase of an MR-lubricated bearing by locally magnetising the fluid film, without losing the low-speed film thickness increase.

2. Develop a fast numerical model capable of taking the shear-thinning characteristics of MR fluids into account.

3. Experimentally evaluate the mode and impact of shaft and journal wear caused by the MR lubrication, and find ways of mitigating the additional (abrasive) wear compared to traditional oil-lubricated bearings. This research objective will be investigated in close collaboration with researchers from the university of Gdańsk.

4. Using the findings from the previous investigations, take steps towards numerically optimising the magnetic field used to activate the MR lubricant in the thin film, and verify the resulting performance experimentally for a range of operating conditions.

1.3 Structure of the dissertation

The chapters of this dissertation generally follow the structure laid out by the set of objectives formulated above, with the exception of chapter 6. Chapter 2 shows that the friction increase associated with MR lubrication in literature can be minimised by diluting the MR fluid and by locally magnetising the fluid film. However, this was also found to result in a relatively small decrease in transition speed. Chapter 3 presents the implementation of a shear-thinning Reynolds equation–based numerical model, with a focus on reducing the computational complexity of the problem, as preparation for further experimental tests. Chapter 4 examines the wear issues observed in chapter 2 in more detail, and shows that the wear in an MR-lubricated journal bearing can indeed be severe depending on the bearing materials. Several possible solutions are investigated and alternative (less stiff) bearing sleeve materials are found to be the most promising. With the results from the previous three chapters taken into account, chapter 5 describes the results of a comprehensive investigation into the performance of an MR-lubricated journal bearing for several magnetic fields, and shows that it is possible to optimise the shape and strength of the applied magnetic field. Chapter 6 presents the performance of MR-lubricated rubber bearing, which has promising wear performance but turns out to be barely affected by the activation of a magnetic field. Finally, chapter 7 provides an all-encompassing discussion of the findings from the previous chapters, and reflects on what these findings mean for the main objective of the dissertation.

2

Proof of Concept

It is known from literature that magnetising an MR-lubricated hydrodynamic journal bearing will result in thicker films, but also in higher friction. To make MR lubrication useful for a larger range of applications, it would be beneficial if it were possible to minimise this increase in friction, ideally without significantly reducing the film thickness increase. This chapter therefore explores the use of an MR fluid with fewer particles, in combination with a weaker magnetic field applied locally near minimum film. With these measures are expected to reduce fluid viscosity, and therefore to lower friction.

This chapter previously appeared as *G. H. G. van der Meer, F. Quinci, W. Litwin, M. Wodtke, and R. A. J. van Ostayen, 'Experimental comparison of the transition speed of a hydrodynamic journal bearing lubricated with oil and magnetorheological fluid', Tribology International, vol. 189, p. 108976, Nov. 2023.*

Please note that the addendum at the end of this chapter was not part of the original publication, and compares the shear-thinning numerical model described in chapter 3 with the Newtonian model presented in this chapter.

Abstract

A journal bearing test bench is used to find the transition speed between the hydrodynamic and mixed lubrication regimes for a modified magnetorheological (MR) fluid. It is shown that the transition speed of the bearing can be reduced by applying a local magnetic field near minimum film when it is lubricated with the MR fluid, and that this will only marginally increase friction. The lubricating performance of the MR fluid is compared to that of a reference oil, and all experimental results are compared with a Finite Element model based on the Reynolds equation.

2.1 Introduction

Hydrodynamic journal bearings are used to support high speed rotating shafts through a thin film of pressurised lubricant, separating the bearing surfaces and reducing friction and wear [3, 31]. This pressure generation is the result of the relative motion between the shaft and bearing, and scales with the speed of the shaft. At low speeds the pressure generation will be insufficient to carry the load, causing a transition from the high speed hydrodynamic lubrication regime to the low speed mixed or even boundary lubrication regime. In applications where the shaft frequently has to start and stop, this not only increases power consumption, but can reduce the lifetime of the bearing as well due to increased wear. For those applications it is desired to reduce the transition speed, the minimum speed where the bearing can still operate in the hydrodynamic regime, as much as possible.

Several methods exist for improving the low speed performance of hydrodynamic journal bearings. One effective way of separating the surfaces is by using a hydrostatic or hybrid bearing, where at low speeds the oil film is created with high pressure lubricant provided by an external pump [32]. This allows for low friction operation of the bearing at all speeds, however, if the pump were to fail the performance of the bearing would deteriorate, causing an unexpected increase in friction and wear. Another technique that can be used to increase pressure generation and load capacity at all speeds is the use of textured surfaces. However, these are susceptible to wear during boundary lubrication and can be difficult to design correctly, leading to a decrease in performance if the operating conditions are unfavourable [33, 34]. A third technique, which is also the focus of this research, is the use of so-called 'smart' lubricants that experience a change in rheological properties when exposed to an external field [35].

One of these smart lubricants are the magnetorheological (MR) fluids. An MR fluid consists of a mineral carrier oil with a large concentration of iron microparticles in suspension, usually amounting to about 70 to 80% of the total mass, as well as a number of additives [13]. When a magnetic field is applied to the fluid the particles will interact and form structures. These structures trap the oil and have the effect of turning the fluid into a viscoplastic solid at low shear stresses, while at higher shear stresses the structures are partially broken apart, leading to a higher effective viscosity that scales with increasing magnetic field strength. When the magnetic field is removed, the particles lose their magnetisation and the structures dissipate within a few milliseconds, returning the viscosity to its original value [5, 6, 15].

Due to the complicated non-Newtonian behaviour of these fluids, there exists a large amount of literature focused on developing analytical or numerical models [11]. For a lubricated contact using MR fluid, this can be done with a continuum approach which requires the use of one of several rheological models. Generally, either the Bingham plastic or Herschel-Bulkley model is used, but multiple other models exist as well [11, 36]. Both models include the viscoplastic behaviour of an MR fluid at low shear stress using a yield stress that depends on the magnetic field strength. Above the yield stress, the Bingham plastic assumes a linear relation between shear stress and shear rate, while the Herschel-Bulkley model also includes the effects of shear-thinning. Shear-thinning should be taken into account when the shear rate is high (order of magnitude $> 1 \times 10^4 \mathrm{s}^{-1}$) [37, 38], which is generally the case in high speed hydrodynamic journal bearings. For modelling a bearing

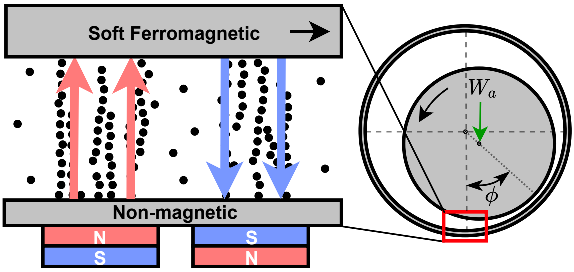

Figure 2.1: A schematic figure (not to scale) of an MR-lubricated journal bearing with a local magnetic field applied just before the location of minimum film. The magnetic field moves from the left magnet to the shaft, and then through the shaft and back to the magnet on the right. This figure is just for illustration, the actual magnetic field that was used during the experiments is discussed in section 2.2.3.

lubricated with an MR fluid, the rheological model is usually combined with either the Navier-Stokes equations [21, 39], or the Reynolds equation [40, 41], which is a simplified form of the Navier-Stokes equations that can be used for thin film flows [42].

On the experimental side, MR fluids have been used most successfully in active dampers [43], even resulting in some commercial applications [17, 44]. However, the use of these fluid in bearings has also gotten some attention, although it should be noted that only a limited number of experimental investigations could be found in literature. Hesselbach and Abel-Keilhack [26] used MR lubrication in a hydrostatic bearing with the aim of achieving a constant bearing gap for variable load. By varying the magnetic field at constant load they could obtain large changes in gap size with relatively small magnetic fields. Based on these findings, they concluded that very high stiffness could be achieved in a closed-loop system with a constant bearing gap, which was later attempted experimentally in [45]. A hydrodynamic journal bearing lubricated with MR fluid was investigated by Urreta et al. [27], who found that for the same configuration of magnetic coils, a magnetisable carbon steel shaft resulted in higher load capacity and a more stable locus than a non-magnetic stainless steel shaft. They mention that this increase in load capacity could be used to widen the operating range of a hydrodynamic bearing, reducing the transition speed. Bompos and Nikolakopoulos [25] looked at the stability of oil and MR-lubricated rotor systems, and found that compared to oil lubrication the activated MR fluid increased stiffness and damping, while reducing the diameter of the shaft orbits at low load. Vaz et al. [28] found experimentally that the high viscosity of activated MR fluid not only increases load capacity, but also friction force. Several numerical investigations also cite this as the main drawback of MR lubrication [20, 21, 39]. This friction force increase of MR fluid compared to standard lubricant is problematic, since it will increase the power consumption of the system. A promising method of limiting the friction increase while still increasing load capacity might be to locally magnetise the MR lubricant film (see figure 2.1), instead of magnetising the entire film as is usually done [46]. Quinci et al. [30] tested this concept experimentally and compared it with oil lubrication, but still recorded high friction losses for the MR fluid. They did note that the standard commercial MR fluid that was used was not optimal for their specific application, and had a very high base and magnetised viscosity compared to the base viscosity of the oil and MR fluid. They suggested creating an MR fluid tailor-made for hydrodynamic lubrication.

In summary, literature demonstrates that MR fluid can be used as a lubricant in hydrodynamic journal bearings in order to increase the load capacity, which at low speeds results in a reduction of the transition speed. However, the main drawback is the increased friction coefficient compared to standard lubricant due to the higher viscosity of MR fluids [20, 21, 28, 39]. While it has been suggested [30, 46] that it might be possible to reduce the friction coefficient with MR lubrication by locally magnetising the film and by optimising the MR fluid to decrease its viscosity, the experimental verification of this hypothesis does not yet exist. Therefore, this paper presents for the first time in literature the experimental and numerical results of a hydrodynamic journal bearing lubricated with a locally magnetised low viscosity MR fluid. Our research shows that this approach will indeed result in less friction than when using a reference lubricant, without the loss of the magnetically induced load capacity increase at low speeds.

2.2 Materials and methods

The experimental measurements in this research were performed using a custom-built setup for testing a hydrodynamic journal bearing. With standard mineral oil lubrication (from now on the ”reference measurements”) and MR lubrication (from now on the ”MR measurements”) the shaft locus, coefficient of friction and bearing temperature were measured for different speeds, with the aim of identifying the transition speed of the bearing system. These experimental results were compared with the numerical results from a model based on the 2D Reynolds equation. This section provides the details of the setup and experimental procedure, as well as the lubricant properties and the structure of the numerical model.

2.2.1 Experimental setup

A photo of the experimental setup is shown in figure 2.2, the main properties of the setup and experimental conditions can be found in table 2.1. The setup consists of a 50mm shaft (1) supported by two self-aligning ball bearings (2), with the housing that contains the hydrodynamic journal bearing (3) centred in between the ball bearings. The shaft is driven by a 5.5kW AC electric motor (4) that is controlled via a frequency inverter, with velocity feedback provided by an incremental encoder mounted on the shaft inside the motor housing. A pneumatic jack is used to generate a constant radial load, which is measured with a Futek LCF455 load cell (5) mounted on the piston (accuracy about ±30N), and can be changed by modifying the air pressure in the jack. The jack is mounted on a small shaft parallel to the main shaft (1) which is supported by two ball bearings, to prevent it from constraining the movement of the housing around the main shaft. A hydrostatic bearing (6) supplied by a hydraulic pump then transfers the load from the jack to the bearing housing, creating a hydrostatic oil film in between those two components. This allows for accurate friction measurements using a moment arm and a 100lb Futek LSB201 load cell (7). Following the data sheet [47] and assuming rectangular probabilities, this load cell has a standard combined uncertainty of ±0.39N. The friction force in the bearing is determined from these measurements by calculating the bearing torque (multiplying the load cell force with the distance between the load cell and the centre line of the bearing)

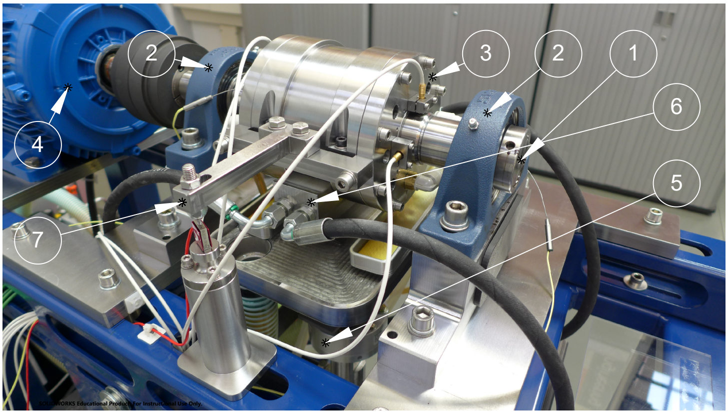

Figure 2.2: The setup used to conduct the measurements. 1 - main shaft, 2 - support bearings, 3 - bearing housing, 4 - electric motor, 5 - load cell, 6 - hydrostatic bearing, 7 - moment arm.

and dividing it by the bearing radius. Assuming an applied load of 2.5kN, this translates to a standard deviation on the measured friction coefficient of ±0.0012. The uncertainty due to the dimensional tolerances of the housing and moment arm were found to be negligible compared to the uncertainty of the sensor, and were therefore not included in the final calculation. The lubricant of the hydrodynamic bearing (oil or MR fluid) is pumped from a reservoir with a separate cavity pump, a positive displacement type pump selected for its ability to pump fluids with high particle content. The bearing is connected to the pump with flexible silicon tubes to limit the influence of the tubes on the friction measurement.

Overview of the bearing

A schematic overview of the bearing housing is shown in figure 2.3. Permanent magnets were used to locally magnetise the MR fluid, and one of the main considerations during the design of the bearing housing was that it should be possible to create any magnetic pattern in the film, without replacing or moving the bearing bush. For that reason, only the edges of the bearing bush (a & b) are used to support it in the C45 steel flanges (d) of the housing. The resulting open space (marked with 'open' in the figure) can be utilised to place the permanent magnets in any desired pattern using disposable 3D-printed support structures (not shown). To limit deformations of the relatively soft bronze bearing bush (a) due to the hydrodynamic pressure buildup in the bearing, it is press-fitted inside a stiffer AISI 304 steel bush (b). The housing is completed with two half-cylindrical C45 steel shells (c1 & c2), which can be removed to access the magnets while the bearing is installed on the shaft. As a result, it is only necessary to remove the bearing from the shaft in order to clean it when switching lubricants.

Lubricant enters the bearing through two inlet holes at $\phi = 90^\circ$ and $\phi = -90^\circ$ ($\phi = 0^\circ$ is the rest position of the shaft, see figure 2.3 for the coordinate system), with a groove distributing the lubricant in the axial direction. The lubricant exits the bearing at both axial ends where it can return to the reservoir. Aluminium contactless labyrinth seals (e) are used to reduce leakage, these were selected to prevent the seals from affecting the friction measurement. The bearing sleeve temperature was measured using eight 1mm

Table 2.1: Overview of the bearing properties and operating conditions

Property	Symbol	Value
Shaft diameter	D	50mm
Bearing length	L	100mm
Nominal radial clearance	h_0	100µm
Bearing surface roughness	Ra	0.4µm
Shaft surface roughness	Ra	0.4µm
Lubrication groove radius/length		1mm/50mm
Moment arm length		200mm
Rotational speed	n	0 to 500rpm
Applied load/Specific pressure	W_a/p_m	2.5kN/0.5MPa
Average lubricant temperature	T	32°C
Lubricant pump flow rate	Q_{in}	0.3L min^{-1}
Magnet remanence	B_r	1.29-1.32T
Magnets diameter/length		20mm/20mm
Centre-to-centre distance magnets	L1	20.8mm
Distance magnets-film	L2	8mm

OD type K thermocouples (accuracy about ±1.5K) installed in radially drilled holes 2mm below the bearing inner surface, with one additional thermocouple measuring fluid temperature inside one of the two inlets (not shown). The expected temperature of the fluid film will probably be slightly higher than the temperature measured by the thermocouples. However, taking into account the high thermal conductivity of the bronze bearing sleeve and the relatively light operating conditions of the test, it is expected that the difference between the fluid film and sleeve temperatures will be small. Finally, two Micro-Epsilon capaNCDT6200 amplifiers control four Micro-Epsilon CS05 capacitive distance sensors (accuracy about ±0.15µm, sensors not shown), that are mounted on the housing using clamps (f) to measure the locus of the shaft. Two sensors are installed 90° apart on either side of the housing, the locus is determined by averaging the results from both sides.

2.2.2 Lubricant properties

For the reference measurements Castrol MHP 153 (SAE 30) was used, which is a lubricating oil designed specifically for maritime applications (such as stern tube bearing lubrication). The MR measurements were performed using a modified version of the commercially available MR fluid MRHCCS4-A designed by Liquids Research Ltd. At request, the commercial fluid was modified by Liquids Research Ltd. to reduce the viscosity of the MR fluid to below that of the reference oil at high shear rates. In addition, the mass fraction of the 1 to 2µm particles was reduced from 70 to 20%, and the ratios of the various additives were modified. The effective viscosity of both the MR and reference lubricants was validated for different shear rates and temperatures using an Anton Paar MRC 302 rheometer with a cone type spindle. The viscosity of the MR fluid was also measured with magnetic fields of different strength applied. The results are shown in figure 2.4.

Figure 2.4a clearly shows the strong shear thinning properties of the MR fluid, especially compared to the standard lubricant (which is also slightly shear-thinning). When

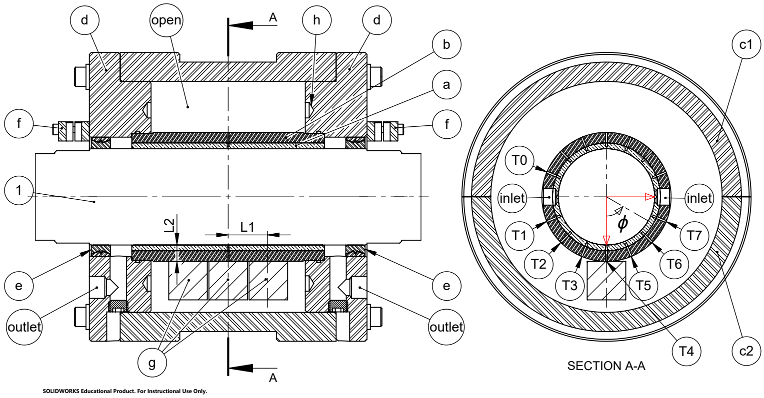

Figure 2.3: Schematic cross-section of the bearing housing. 1 - main shaft, a - bearing bush, b - reinforcement bush, c1&c2 - housing shells, d - housing flanges, e - labyrinth seals, f - capacitive sensor clamps, g - permanent neodymium magnets, h - notch, T0-T7 - thermocouples. The coordinate system that was used is shown in the cross-section on the right, the shaft rotates in the positive ϕ direction. Not shown is the non-magnetic 3D-printed structure that fills the space marked with 'open' and is used to keep the magnets in place. This structure is fixed in the housing using the four notches.

a magnetic field is applied, the viscosity of the MR fluid increases rapidly, especially at lower shear rates. However, shear rates in the bearing are expected to be relatively high (order of magnitude $1 \times 10^4 \mathrm{s}^{-1}$), at which point the MR viscosity without magnetic field is about half that of the reference lubricant. With a magnetic field of $160 \mathrm{kA\,m}^{-1}$ the viscosity at high shear rates is increased approximately by a factor 2, and it is clear that the shear-thinning effect becomes stronger. For comparison, the unmodified MR fluid is only 10% less viscous than the reference lubricant at high shear rates, and its viscosity increases by a factor 7 when magnetised at $160 \mathrm{kA\,m}^{-1}$. At low shear rates the difference between the modified and unmodified MR fluid is even larger. At $1000 \mathrm{s}^{-1}$ the viscosity of the modified MR fluid increases by a factor 15 when a $160 \mathrm{kA\,m}^{-1}$ magnetic field is applied, while the viscosity of the unmodified MR fluid increases by a factor 40. Figure 2.4b shows that both the standard lubricant and the MR fluid show a decrease in viscosity for an increase in temperature. With the magnetic field activated this decrease becomes less strong, because the influence of the magnetised particle structures on the viscosity starts dominating the influence of the carrier oil [48]. Finally, figure 2.4c shows the magnetic response of the MR lubricant. Here it can be seen that at higher magnetic field strengths the particles reach saturation, causing the curve to flatten out.

Bearing sleeve temperature

The viscosity measurements with varying shear rate and varying field strength were both performed at constant temperature of 32°C. This temperature was chosen based on the film temperatures measured by the thermocouples during the Stribeck measurements, figure 2.5 shows some representative temperature profiles. Please take into account that no heat exchanger was used to keep the lubricant reservoir at a constant temperature during the measurements.

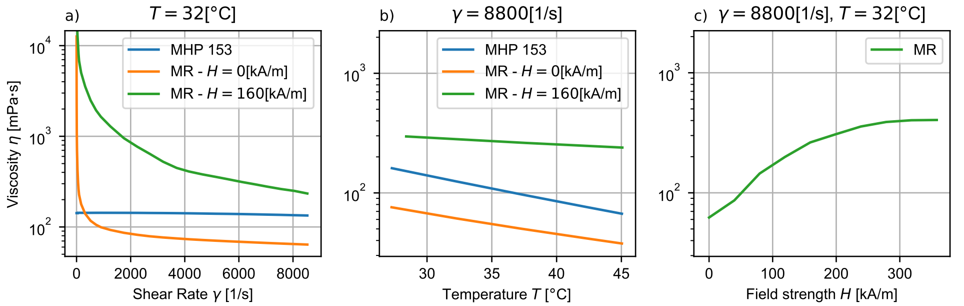

Figure 2.4: a) Effective viscosity vs shear rate for both lubricants and different magnetic fields (constant temperature). b) Effective viscosity vs temperature for both lubricants and different magnetic fields (constant shear rate). c) Effective viscosity vs magnetic field strength for the MR lubricant (constant temperature and shear rate). Take note that only subfigures b) and c) use the same scale for the y-axis.

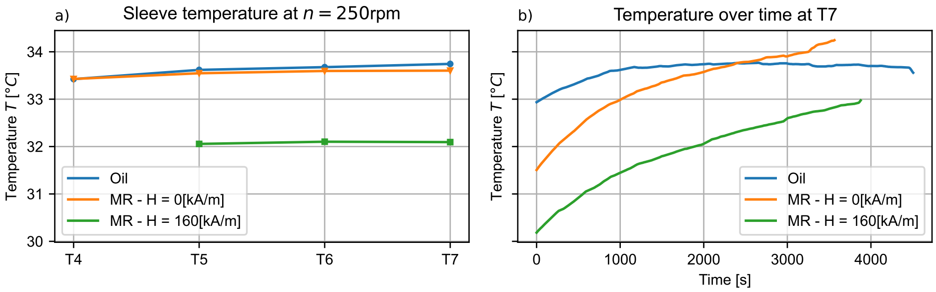

Figure 2.5: a) The bearing sleeve temperature near minimum film for all lubricants. The temperature profiles are shown for only one speed per lubricant (250rpm corresponds to $t = 2100$s), these results are representative of the profiles at all speeds. Thermocouple T4 is missing for the measurement with activated MR fluid, since a permanent magnets was placed at that location instead. b) Sleeve temperature over time for the different lubricants as measured by thermocouple T7, which recorded the highest temperatures of all thermocouples.

Figure 2.5a shows the bearing sleeve temperature profiles in the lower right quadrant of the bearing at high speed ($n = 500$rpm) for both the reference and MR measurements (see figure 2.3 for the thermocouple locations). For all lubricants, the variation in film temperatures inside the bearing is seen to be small, the variation is less than 1°C. Figure 2.5b shows the temperature over time in thermocouple T7, again for both measurements. Here it can be seen that the temperature in the oil-lubricated bearing mostly stabilises after about 1000s, while the temperature in the MR-lubricated bearings continues to rise during the Stribeck measurements, leading to a temperature increase of slightly less than 3°C over the course of the experiment. It is not known why the temperature does not stabilise during the time frame of the test when using MR lubrication, but it might be related to the different thermal properties the two fluids, as well as the different amounts of fluid in the reservoir (see section 2.2.4).

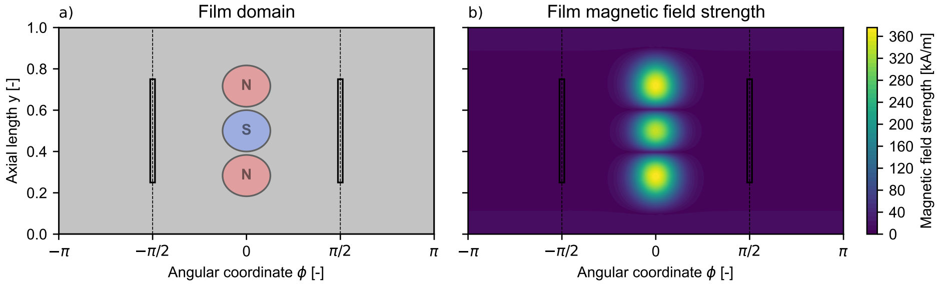

Figure 2.6: a) The unfolded fluid film of the journal bearing, with the magnets and inlets shown at respectively $\phi = 0$ and $\phi = -\pi/2$ & $\phi = \pi/2$. The distance (out-of-plane) between the magnet surface and the film is 8mm, the pole that is turned towards the film is indicated with 'N' (north) or 'S' (south). b) The corresponding norm of the magnetic field strength profile in the fluid film in $\mathrm{kA\,m^{-1}}$. The profile is taken at the middle of the film.

2.2.3 Magnetic field properties

For the MR measurements with magnetic field, a relatively simple magnetic pattern was used. Based on some simple initial numerical calculations, three cylindrical N42 neodymium magnets were placed in a line along the axial direction at an angle of $\phi = 0°$ as can be seen in figure 2.6a. Because the bearing bush is non-magnetic, a fairly uniform magnetic field is formed locally between the magnets and the steel shaft. Furthermore, it was found that by reversing the polarity of the central magnet with respect to the other two, the field strength in the rest of the film could be reduced even further.

The resulting magnetic field was calculated with the "Magnetic Fields, No Currents (mfnc)" interface of the AC/DC module of the commercial FEM software package COMSOL Multiphysics® 6.1. This interface implements Gauss' law for the magnetic field using the scalar magnetic potential, with cubic order shape functions. The 3D computational domain can be seen in figure 2.7, only one quarter of the system is modelled since it is symmetric. The parts that are highlighted in the figure (C45 housing and shaft) are assumed to be soft ferromagnetic and are modelled with a magnetisation curve (curve data taken from measurements in [49]). The influence of the housing on the magnetic field in the film was found to be relatively minor (especially close to the magnets), which is why the housing geometry was simplified by removing all internal features (inlets, outlets, bolt holes, etc...) in order to reduce the computational complexity of the problem. All other parts are assumed to be non-magnetic and have a relative permeability of 1 (air domain), or are not modelled (bearing bush). The permanent magnets are modelled with the remanent flux density magnetisation model (see table 2.1 and figure 2.6 for magnet strength and orientation respectively). An unstructured tetrahedral mesh was generated for the computational domain using the "extremely fine" mesh preset, resulting in a mesh with 158 733 elements with a quadratic order shape function. The standard solver (Newton-Raphson iteration with under-relaxation) was used with a relative tolerance of 1×10^{-3} in order to calculate the solution for a total of 731 371 degrees of freedom. These settings were confirmed by a mesh convergence study. Figure 2.6b shows a profile of the magnetic field strength in the middle of the film (the change in magnetic field strength over the film thickness is negligible), where it is clear that the strongest magnetic field is located

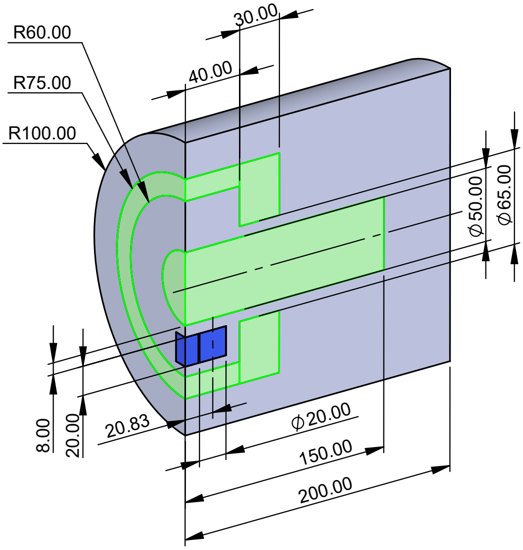

Figure 2.7: The 3D computational domain used to calculate the magnetic field in the fluid film. The soft ferromagnetic shaft and housing are highlighted in green, the magnets in dark blue, and the air in grey. Dimensions are in millimetres.

around $\phi = 0$, and that the magnetic field is negligibly small almost everywhere else. There is a small increase in magnetic field strength near the edges of the bearing ($y = 0$ & $y = 1$) where it is supported by the (ferromagnetic) steel flanges of the housing, but this effect is small as well.

2.2.4 Experimental procedure

All measurements were performed under identical experimental conditions, only changing the lubricant or the magnetic field depending on the measurement being conducted. The goal of these measurements was to identify the critical transition speed where the bearing changes from the hydrodynamic regime to the mixed or boundary lubrication regime, which was done by generating Stribeck curves at a constant load (2.5kN/0.5MPa).

Before every single Stribeck measurement, the setup was warmed up by letting it run at the target load and at maximum speed (500rpm) until the lubricant temperature in the tank reached 26°C. Depending on the lubricant, the ambient conditions, and the volume of lubricant in the tank, this took anywhere between 1 and 3 hours. The lubricant volume was 7L for the standard lubricant, but due to its high cost only 1.5L of the MR fluid were used at a time.

After the warm up, the Stribeck measurement was conducted by reducing the speed from 500 to 300rpm in steps of 50rpm, and then from 300 to 0rpm in steps of 25rpm. After every step the speed was kept constant for 5min to allow for stabilisation of the temperature in the film. If at any point during this test, the coefficient of friction (CoF) became larger than 0.02 for more than 1min, the bearing was assumed to have entered mixed or boundary lubrication and the measurement was stopped. During every step, LabVIEW was used to read data from all sensors at a frequency of 100Hz, apart from the thermocouples which were read at 3Hz. For the final 10 seconds of every step, data from the capacitive sensors was read 500 times per shaft revolution (e.g., 1875Hz at 225rpm) to enable an accurate calculation of the shaft locus.

Finally, after the Stribeck curve had been recorded the clearance circles were measured (without removing the applied load) to be able to place the shaft locus in the bearing [50]. This means that the capacitive sensors were used to record the maximum clearance of the shaft in the bearing for all angular coordinates ϕ, by rotating the bearing housing 360° around the shaft. For this process, the moment arm and tubing were removed, and only the hydrostatic bearing was left turned on. The clearance circle was then constructed by least-squares fitting a circle through 12 points recorded by the capacitive sensors at evenly spaced angles.

2.2.5 Numerical modelling

The hydrodynamic performance of the bearing in the experimental setup has also been compared with a FEM numerical model made using COMSOL® Multiphysics 6.1 [51]. The aim was to compare the reference measurements with a numerical model validated in literature, and to see if this model could correctly predicted the trends of the MR measurements in the hydrodynamic regime. The mixed and/or boundary lubrication regimes are not included in the model, which means that the transition speed cannot be determined exactly. The model that was used is based on 2D Reynolds equation combined with the JFO boundary conditions to include cavitation. Because the difference in temperature in the film was found to be small during the experiments (as discussed in section 2.2.2), it was assumed that an effective (constant) film temperature of 32°C could be used, which is the average film temperature over time for all measurements. The effect of shear-thinning on the viscosity was not taken into account either. The reasoning for this is that the shear thinning effect of the MR fluids (especially without magnetic field) is less pronounced at the relatively high shear rates expected to be found in the bearing. At shear rates close to zero shear-thinning is much stronger, and MR yield stress would also have to be taken into account. In the current model the viscosity at a shear rate of $\gamma = 8800\text{s}^{-1}$ is used for all speeds, as well as the magnetic field dependency from figure 2.4c.

Equation 2.1 shows the Reynolds equation as found in [52], with pressure p, cavitation mass fraction f_c, film thickness h, viscosity η and shaft surface speed u. In order to include cavitation, a variable transformation is used to replace both p and f_c with functions of a new variable ξ (equations 2.2 & 2.3). By assuming that at any point in the computational domain, the lubricant is either in a full film region ($p > 0$, $f_c = 1$) or in a cavitated region ($p = 0$, $f_c < 1$), the Reynolds equation can be solved for a single variable (ξ) that represents either the pressure or the mass fraction, depending on its sign.

$$\frac{\partial}{\partial x}\left(-\frac{h^3 f_c}{12\eta}\frac{\partial p}{\partial x} + \frac{h f_c u}{2}\right) + \frac{\partial}{\partial y}\left(-\frac{h^3 f_c}{12\eta}\frac{\partial p}{\partial y}\right) = 0 \tag{2.1}$$

$$p = (\xi \geq 0)\xi \tag{2.2}$$

$$f_c = 1 + (\xi < 0)c_f\xi \tag{2.3}$$

By entering equations 2.2 & 2.3 in the Reynolds equation, and by adding artificial diffusion in the x- and y-directions using the transformation constant c_f ($c_f = h^2/(3\eta h_e)$ with mesh element size h_e), the Reynolds equation is reduced to equation 2.4. For a detailed derivation and discussion of this cavitation algorithm, and the calculation of the transformation constant, the reader is referred to [52].

$$\frac{\partial}{\partial x}\left(-\frac{h^3}{12\eta}\frac{\partial\xi}{\partial x}+\frac{hf_c u}{2}\right)+\frac{\partial}{\partial y}\left(-\frac{h^3}{12\eta}\frac{\partial\xi}{\partial y}\right)=0 \tag{2.4}$$

The implementation of the model is extended in a two ways. First of all, the steady state shaft locus is determined by solving equations 2.5 and 2.6[1] for the film pressure p, with F_x and F_y the horizontal and vertical load capacities respectively.

$$F_x = \iint_S p\sin\phi\,\mathrm{d}A = 0 \tag{2.5}$$

$$F_y = \iint_S p\cos\phi\,\mathrm{d}A = W_a \tag{2.6}$$

The second extension is a simple equation for calculating the inlet pressure p_{in}. Since a positive displacement pump is used for transporting the lubricant, it is not possible to assume a constant inlet pressure for all speeds of the shaft, like with a pressure-driven flow. Instead, the flow coming out of the pump (with volume flow rate Q_{in}) will be divided over inlets 1 and 2 (with volume flow rates Q_1 and Q_2), with the ratio Q_1/Q_2 being a function of the speed. This is modelled with equation 2.7, which is solved for p_{in}.

$$Q_1 + Q_2 - Q_{in} = 0 \tag{2.7}$$

The volume flow rates Q_1 and Q_2 are obtained by integrating the flow rates q_x and q_y (from the continuity equation) over the boundaries of the inlets.

Finally, the friction coefficient f is determined using equation 2.8, with the integrand evaluated at the stationary surface. This surface corresponds to the inner surface of the hydrodynamic bearing, which is connected to the moment arm used for measuring friction in the experimental setup (number 7 in figure 2.2).

$$f = \frac{\iint \tau_{xz}\big|_{z=0}\,\mathrm{d}A}{W_a} \tag{2.8}$$

Software implementation

The Reynolds equation (eq. 2.4) is implemented as a General Form PDE in COMSOL® with cubic order Lagrangian shape functions, and equations 2.5-2.7 are added as global equations. The pressure is set to 0 (atmospheric pressure) at the open edges of the bearing ($y = 0$ ad $y = 1$) using a Dirichlet boundary condition, and similarly the pressure at the edges of the inlet is set to the value of p_{in} with a Dirichlet boundary condition as well. A

---

[1] *Footnote not present in original publication* - A small mistake was made in writing down equations 2.5 and 2.6, the surface integral is written as $\iint_S$ which means the differentials should be written as dS instead of dA.

periodic boundary condition is used for the edges of the computational domain at $x = -\pi$ and $x = \pi$. The computational domain (shown in figure 2.6a) is discretised using a structured quad mesh with a maximum element size equal to the diameter of the inlet grooves, resulting in 3950 quad elements and a total of 35 941 degrees of freedom to be solved for. The solution process uses a segregated solver that is based on Newton-Raphson iteration with under-relaxation and is assumed to be converged when the relative tolerance is lower than 1×10^{-6}. During the solution process the first step is to calculate an initial solution by solving the Reynolds equation individually (without equations 2.5-2.7) at the maximum speed of 500rpm. After that all four equations are solved at the same time, and a parameter sweep is used to reduce the speed in steps of 25rpm. The sweep is set to stop once the speed reaches the transition speed that was found experimentally, the transition speed is not calculated by the model. All of these settings were confirmed to give mesh convergence.

2.3 Results and discussion

In this section the results of the reference measurements with oil, and the MR measurements with and without magnetic field are presented and discussed. All three sets of measurements were performed four times under the same operating conditions, with the figures in this section showing the average of those four repetitions for the Stribeck curve and the shaft locus (including eccentricity and attitude angle plots).

2.3.1 Stribeck curve

The experimental and numerical Stribeck curves as a function of shaft rpm are shown in figure 2.8 for the reference and MR measurements. The experimental curves in figure 2.8a show good repeatability, especially in the hydrodynamic regime where the error margins are approximately equal in size for all lubricants. These error margins show the maximum and minimum friction values that were recorded during the four repetitions, and looking at all measurements the largest difference is less than 0.0014 (for the reference measurement). In the mixed regime the differences between the repeated measurements are much larger, which could be related to the stochastic nature of mixed lubrication. The transition between the hydrodynamic and mixed regimes is well-defined for the reference measurement, but it is much more gradual for the MR measurements. This could be explained by the presence of the particles in the MR fluid, which have varying diameters. When the speed of the shaft is decreased, at first only the largest particles will cause contact between the bearing and the shaft, but when the speed is lowered further this will occur more and more often and for smaller particles. This could lead to the gradual friction increase observed in the experiments.

Looking at the data in more detail, it is clear that the oil-lubricated reference bearing displays the lowest transition speed at around 50rpm (with the transition speed defined as the speed where the coefficient of friction (CoF) is minimal). However, while the MR measurements with and without magnetic field show a substantial transition speed increase compared to the reference measurement, the transition speed of the MR measurement with a magnetic field present is lower than that of the measurement without magnetic field. The difference in transition speed is about 50rpm, or a decrease of about 25% go-

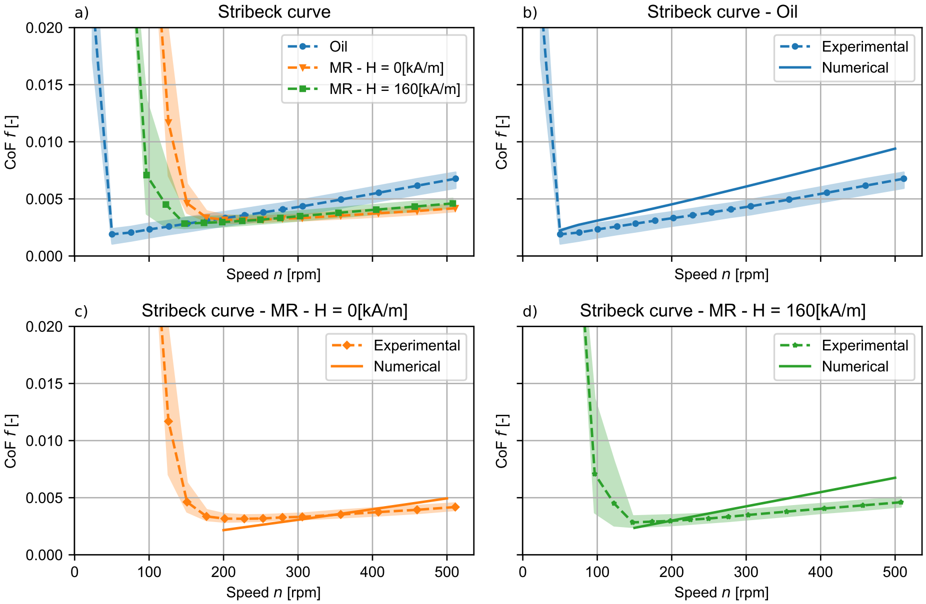

Figure 2.8: a) Experimental Stribeck curves for the reference and MR measurements, showing the difference in transition speed between the tests. The maximum and minimum friction values recorded during the repeated measurements are indicated by the shaded regions, while the average value is indicated by the dotted line. b-d) The experimental Stribeck curves together with the numerically calculated friction coefficients in the hydrodynamic regime (solid lines), shown respectively for b) oil lubrication, c) MR lubrication without magnetic field and d) MR lubrication with a magnetic field[2].

ing from around 200rpm without magnetic field to around 150rpm with field. This clearly shows that the applied magnetic pattern from figure 2.6 successfully increases the load capacity of the bearing at low speeds, although it should be noted that even then, the transition speed of the oil-lubricated reference bearing is around 66% lower still.

When examining the CoF in the hydrodynamic regime, however, something interesting can be seen. Starting at speeds larger than about 225 to 250rpm, the CoF of both of the MR measurements drops below the CoF from the reference measurements. At 500rpm, this results in an average CoF of 0.0047 for MR-lubrication with magnetic field, which is almost 30% lower than the average of 0.0065 recorded with oil lubrication. At higher speeds, this difference will become even larger. Meanwhile, the effect on the CoF of applying the magnetic field to the MR-lubricated bearing is limited, resulting in an average increase of only 14% compared to the situation without magnetic field.

The explanation for why the MR measurements show increased transition speeds and decreased CoFs is simple. As can be seen in figure 2.4, the base viscosity of the MR fluid (at high shear rates) is about half that of the standard lubricant. Lubricating a bearing with a lower viscosity lubricant results in a lower load capacity (and therefore a higher transition

---

[2] *Footnote not present in original publication* - Please note that due to a difference in definitions (average instead of maximum field strength), the magnetic field of 160kA m^{-1} that appears in figures 2.8, 2.9, and 2.10 in this chapter is identical to the magnetic field of 370kA m^{-1} that appears in chapter 5.

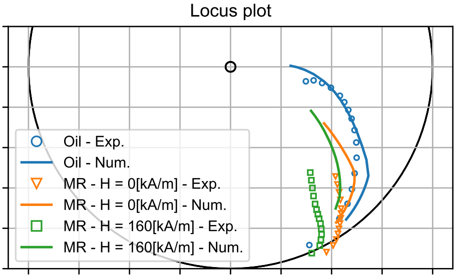

Figure 2.9: The experimental (Exp.) and numerical (Num.) shaft loci for the reference and MR measurements. The small black circle indicates the centre of the bearing, the larger black circle indicates the inner bearing surface.

speed), but also in lower friction, which is exactly what is being shown by the current results. This explanation is confirmed by the numerical results in figure 2.8b, which were calculated using the viscosity data from figure 2.4 and show the same trends. In fact, the fluid viscosity was the only difference between the simulations for oil lubrication and MR lubrication without magnetic field, which are shown in figures 2.8b and 2.8c respectively. There are some deviations between the friction values in the simulations and experiments, specifically, at high speeds the simulations seem to predict larger friction values than were found experimentally. This can likely be attributed to the Newtonian and isothermal approximations that were used during the simulations, but this will be discussed in more detail in section 2.3.2.

The results that were obtained could not have been achieved with a standard commercial MR fluid. Prior research on hydrodynamic lubrication with these fluids has generally concluded that while they increase load capacity, the increase in friction can be quite high and is generally undesirable [21, 22, 39]. Furthermore, the friction issue is exacerbated by the fact that most often the entire fluid film is magnetised. By locally magnetising the film, additional parameters controlling the shape, strength, and position of the magnetic pattern are introduced, which can be tweaked to influence both the load capacity and friction changes [30, 46]. Combine this with a lower viscosity MR fluid with fewer particles (described in section 2.2.2), and the current research shows that the result can be an MR-lubricated bearing that experiences less friction (at high speeds in the hydrodynamic regime) than its oil-lubricated counterpart, while still allowing for a transition speed decrease through the application of a magnetic field. It should also be noted that the specific modified MR fluid and magnetic pattern used in this research could still be optimised further. For example, by increasing the viscosity (base, magnetised, or both) of the MR fluid, or by increasing the strength and magnetised area of the magnetic pattern, it might be possible to create an MR-lubricated bearing that has both a lower transition speed than, and lower or comparable friction to, a bearing lubricated with mineral oil.

2.3.2 Shaft locus

Next to the friction coefficient, the experimental and numerical shaft loci were also obtained for both the reference and MR measurements, as shown in figure 2.9. The shaft locus (the position of the shaft inside the bearing) is plotted as a function of the shaft

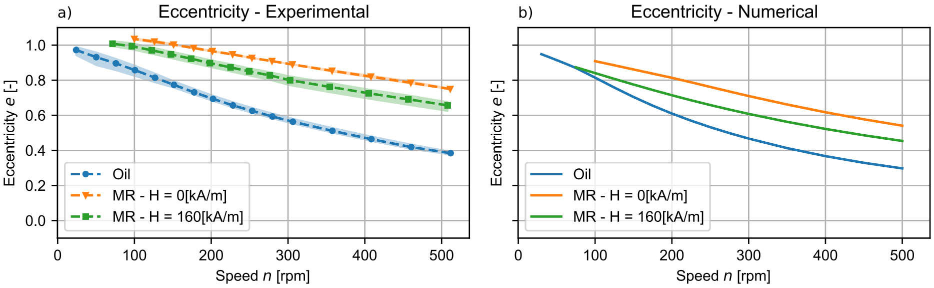

Figure 2.10: The a) experimental and b) numerical eccentricity values for the reference and MR measurements. In subfigure a, the maximum and minimum eccentricity values recorded during the repeated measurements are indicated by the shaded regions, while the average value is indicated by the dotted line.

speed, and for all measurements the points closest to the bearing centre correspond to the highest speed ($n = 500$rpm), while the points on the clearance circle correspond to speeds at or below the transition speed. The locus gives an indication of the film thickness for a specific speed, the closer it is to the centre of the bearing, the thicker the film.

Looking at the experimental results, the shaft locus measurements make sense considering the friction coefficient results discussed in the previous section. The higher viscosity mineral oil used for the reference measurements resulted in a lower transition speed due to an increased load capacity, which translates to thicker films compared to MR lubrication. This can also be seen in figure 2.10, which shows that for all speeds, the eccentricity is lower with oil lubrication. Similarly, comparing the MR measurements with and without magnetic field shows that applying the magnetic field also lowers the eccentricity, again corresponding to the transition speed decrease seen in figure 2.8.

The same general trends are shown by the numerical results. The agreement between experiment and simulation is quite good for the reference measurement, with the numerical locus roughly following the same path as the experimental locus. The numerical model does predict lower eccentricities, especially at higher speeds, which might be caused by the isothermal approximation for the fluid film as was mentioned in the last section. If thermal effects were taken into account, the higher heat generation at higher speeds would results in lower viscosities and therefore higher eccentricities and lower friction values. The accuracy of the model is less good for the MR measurements, with the model underpredicting eccentricity and overpredicting attitude angle, but the general trend of higher eccentricity and lower attitude angle for MR lubrication (compared to oil lubrication) can still be seen. The larger deviations of the numerical model for the MR measurements are not surprising, since the model does not take shear-thinning into account, which is much more important for MR fluid than for oil as can be seen in figure 2.4. Taking this non-Newtonian effect into account would likely result in lower viscosity near the region of minimum film, where the shear rate is relatively high due to the small film thickness. The overall effect would then be a lower load capacity, and likely a better match with the experimental results.

One thing of note in the locus plot, is that the simulation predicts an attitude angle larger than 90° for oil lubrication at the highest speed of 500rpm. This seems to be related to the combination of a relatively low load (2.5kN/0.5MPa), together with the positive displacement pump that supplies a constant flow of lubricant to the two inlets at 90° and −90°. Due to the constant flow rate, the numerical model predicts a relatively high inlet pressure, and for the highest speed this pressure is even similar in value to the film pressure at minimum film. This is likely the cause of the relatively high attitude angles, since modelling the bearing with constant pressure inlets that provide oil at ambient pressure, results in attitudes angles well below 90°. While it is known that a high speed, lightly loaded bearing operating close to 90° can suffer from unstable whirling of the shaft [3, 53], this was not observed during any of the measurements.

An attempt was made to perform measurements at higher loads as well (1 - 2MPa), but it was quickly discovered that this resulted in severe wear to the bearing, even after only one or two Stribeck measurements at these loads. This wear resulted in a groove in axial direction near the location of minimum film with a depth of up to 10μm, which was enough to noticeably modify the shape of the locus at low speeds. For this reason, these results were discarded. The damage was likely caused by abrasive wear due to the presence of the iron microparticles in the contact zone, which is a known phenomenon [54, 55]. This would also explain why the eccentricity at low speed became slightly larger than 1 for both MR measurements (figure 2.10a). Apparently, even at the relatively low load of 0.5MPa that was used during the tests, some wear did build up over the course of multiple separate Stribeck measurements with MR lubrication, resulting in a small groove. This phenomenon is currently being investigated by the authors.

2.4 Conclusion

The current research has shown experimentally that it is possible to lubricate a hydrodynamic journal bearing with a magnetorheological (MR) fluid, and at the same time obtain friction values lower than that of the reference oil lubricated bearing. This was done without losing the capability to reduce the transition speed of the MR-lubricated bearing by applying a local magnetic field near minimum film. This is in contrast to literature, where it is generally reported that MR-lubricated bearings have much lower transition speeds, but also much larger friction values due to the high viscosity of MR fluids. The results in this research were obtained by locally magnetising the fluid film, and by lubricating the bearing with a modified version of a commercial MR fluid with reduced particle content and lowered base viscosity. This modified MR fluid is also less viscous (without magnetic field) than the reference oil that was tested, explaining why the oil lubricated bearing has a lower transition speed, but also experiences more friction. These results were confirmed by the numerical finite element model made in COMSOL® Multiphysics, which predicts the same trends as were observed in the experiments. The accuracy of this model could further be improved by taking shear thinning into account using the generalised Reynolds equation.

Overall, it can be concluded that MR fluid lubrication of journal bearings does not necessarily have to increase the friction coefficient of the bearing. The next step would therefore be to try and find a combination of an MR fluid and a localised magnetic field that results in both a lowered transition speed and a minimal friction increase, combining the benefits of the traditional MR fluids with a strong magnetic response and the modified MR fluid with lower viscosity.

Addendum – shear-thinning model

After the publication of the investigation described in this chapter, development was started on an improved numeral model capable of taking the shear-thinning characteristics of an MR fluid into account. This model will be presented in the next chapter, and was used for the remainder of the project (specifically in chapter 5). The model was also applied to the bearing discussed in this chapter, those results will be presented in this addendum and will be compared to experimental results and the original Newtonian model. In this model, the shear-thinning viscosity of the MR fluid as a function of the shear stress $\vec{\tau}$ is given by the Herschel-Bulkley relation (equation 2.9). Here the parameters K, m, and τ_y depend on the magnetic field strength H as in equation 2.10, which is derived in section 5.2.3. The values of the constants in this second equation are shown in table 2.2 for the MR fluid used in this chapter.

$$\begin{aligned} \eta &= \frac{K^{\frac{1}{m}} |\vec{\tau}|}{f\left(|\vec{\tau}| - \tau_y\right)^{\frac{1}{m}}} \\ f &= \begin{cases} 1 & \text{if} \quad |\vec{\tau}| \geq \tau_y \\ 0 & \text{if} \quad |\vec{\tau}| < \tau_y \end{cases} \end{aligned} \tag{2.9}$$

$$C = c_1 \operatorname{erf}(c_2 (H - c_3)) + c_4 \tag{2.10}$$

Figure 2.11 shows the experimental and (Newtonian) numerical Stribeck curves and eccentricity values previously presented in figures 2.8 and 2.10, as well as the curves resulting from the new shear-thinning model. Comparing all of these curves clearly shows that the shear-thinning model offers an improvement over the Newtonian model in all aspects, with both the friction coefficients and eccentricities lying closer to the experimental values. The improvements are larger for the case with the local magnetic field applied (figures 2.11b and d) than the case without a magnetic field (figures 2.11a and c), this could be due to the isothermal approximation which is still used for the shear-thinning model. Specifically, when the temperatures of the MR fluid increase, the viscosity will reduce less quickly when a magnetic field is applied to the fluid (see figure 2.4). As a result, if the film temperature was higher during the experiments than what is currently assumed in the models, the shear-thinning model would predict a larger increase in eccentricity for the unmagnetised case. The exact same effect has also been observed in later experiments,

Table 2.2: Coefficient values for the magnetic field strength–dependent Herschel-Bulkley viscosity fit of the diluted MR fluid at 32°C used in this chapter.

C	Unit	c_1	c_2	c_3	c_4
τ_y	Pa	1527	8.560×10^{-6}	2.151×10^{4}	1424
K	$\text{Pa} \cdot \text{s}^m$	0.5078	5.590×10^{-6}	2.244×10^{5}	0.6139
m	-	0.06504	1.587×10^{-5}	7.901×10^{4}	1.169

and will be discussed in more detail in section 5.3.3. Next to the film temperature, the wear groove in the experimentally tested bearing sleeve (discussed at the end of section 2.3.2) also explains part of the difference between the model and experiments, but this is true for the Newtonian model as well.

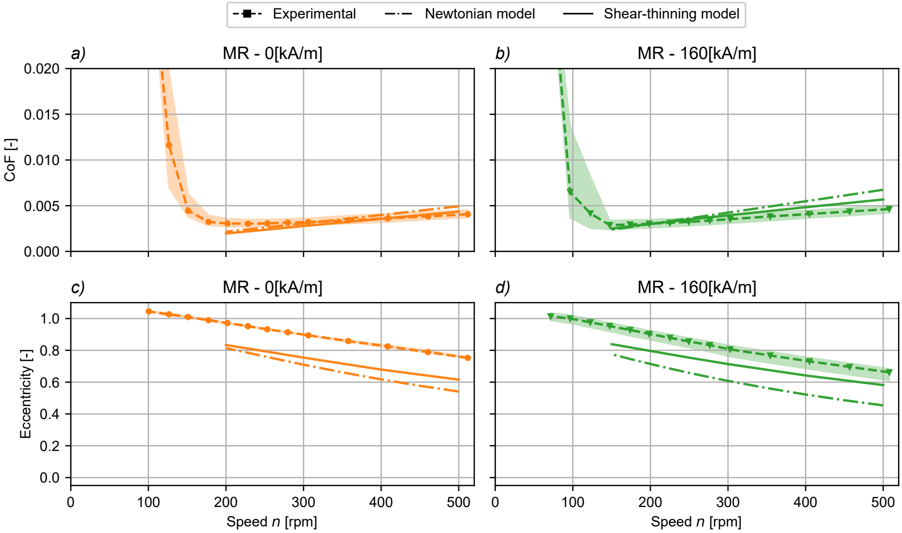

Figure 2.11: Stribeck curves (subfigures a and b) and eccentricity values (subfigures c and d) for the reference and MR measurements, as well as the results of the Newtonian and shear-thinning models.

3

Modelling MR fluids

In the previous chapter the MR-lubricated bearing was modelled with the standard Reynolds equation, assuming a Newtonian lubricant. However, literature and the rheometer viscosity measurements have shown that MR fluids are strongly non-Newtonian, with shear-thinning characteristics that change with the strength of the applied magnetic field. Reynolds equation–based models that can include these effects are already available, but take much longer to solve than the standard Reynolds equation due to several integral terms that are solved numerically for every iteration of the solution process. This chapter presents a method for analytically evaluating these integral terms, resulting in a faster solution process without any loss of accuracy. This new procedure will allow for faster predictions of the results of changes made to the MR fluid or magnetic field, and for easier optimisation studies.

This chapter previously appeared as *G. H. G. van der Meer and R. A. J. van Ostayen, 'Efficient solution method for the Reynolds equation with Herschel–Bulkley fluids', Tribology International, vol. 204, p. 110460, Apr. 2025.*

Abstract

Thin film lubrication problems frequently involve lubricants with non-Newtonian characteristics, and a relatively simple viscosity model that can describe several non-Newtonian fluids is the Herschel-Bulkley relation. This relation can model solid-like properties of a lubricant at low shear stress using a yield stress, while at higher shear stress values shear-thinning or thickening can be included. In literature, this viscosity model has been combined with various governing equations to solve the non-Newtonian thin film problem, resulting in models that range from full 3D CFD simulations, to 1D Reynolds equation based methods. However, something that all of these approaches have in common is that they are either computationally expensive, can only be used for 1D geometries, or use non-exact, regularised versions of the Herschel-Bulkley model for reasons of numerical stability. This paper therefore introduces a method for solving a thin film problem with a non-regularised Herschel-Bulkley lubricant using the 2D generalised Reynolds equation, and this approach is shown to be fast without compromising on accuracy. The increased speed will allow the model to be used more efficiently in complex simulations or design optimisation scenarios.

3.1 Introduction

The increasing demands placed on bearing systems, such as stern tube bearings found in ships, require hydrodynamic bearings that can function at higher loads and with lower friction, for both lower and higher speeds. For these increasingly stringent goals to be met, fast and accurate numerical models that can for example be used in design optimisation studies, are essential. One aspect of a good model is a proper understanding of the behaviour of the lubricant, which is frequently assumed to be Newtonian. However, even more traditional oils and greases can display non-Newtonian behaviour [56, 57], and these non-Newtonian effects are even more important when considering newer 'smart' lubricants, such as magnetorheological fluids [35]. It is clear that Newtonian models do not suffice in these cases, and non-Newtonian effects will have to be taken into account to obtain an accurate model.

In order to include the non-Newtonian effects of the lubricant, a viscosity model is needed which describes the relation between the shear stress and the shear rate of the lubricant. Many different empirical viscosity models for non-Newtonian fluids can be found in literature. Three of the simpler models, all with only 2 or 3 parameters, are the Bingham plastic model, the Ostwald–de Waele model or power law model, and the Herschel-Bulkley model. A Bingham plastic is a fluid with a yield stress, which means that the fluid is considered a solid when the internal stress is below the yield stress, and that the fluid behaves like a Newtonian fluid otherwise. The part of the fluid flow domain that behaves like a solid is also called the plug or the core. This Bingham plastic model is quite popular due to its simplicity, and has for example been used to model grease-lubricated bearings [58, 59], as well as magneto- and electro-rheological lubricants [6, 11]. An overview containing a large number of other applications from various fields has been created by Bird et al. [60]. In contrast to the Bingham plastic, a power law fluid does not have a yield stress, but is one of the simpler models that includes the effects of a shear-dependent viscosity. It has frequently been applied to model a wide variety of shear-thinning (pseudoplastic) and shear-thickening (dilitant) lubricants [61, 62]. Finally, the Herschel-Bulkley model combines the Bingham plastic and power law characteristics and can therefore represent a fluid with both a yield stress and a shear-dependent viscosity. Depending on the lubricant, using this more general model can lead to a better match between simulations and experiments, but it will results in more complex numerical models that are less likely to converge [63–65].

Next to the viscosity model itself, a modelling approach is needed to combine the viscosity model with either the Reynolds equation or the Navier-Stokes equations. A number of different approaches can be found in literature to do this for bearing systems.

One approach is to derive modified Reynolds equations for the different cases of core formation of a Bingham plastic (i.e. a core sticking to one of the bearing surfaces, a floating core, or no core formation at all). This was first done by Wada et al. who derived implicit 2D Reynolds equations for a Bingham plastic, that they applied to a step bearing and a journal bearing [66–68]. Later on, Tichy managed to derive explicit Reynolds equations for the different core cases of a 1D Bingham plastic flow [69]. The disadvantage of these methods is that it can be difficult to find explicit Reynolds equations for all cases of core formation, especially in 2D flows. The advantage is that once the equations have been found, convergence is fast.

Another approach that is commonly used is based on the generalised Reynolds equation introduced by Dowson [70]. Because this more general variant of the standard Reynolds equation allows for viscosity variations over the height of the lubricant film, it can be used to properly account for non-Newtonian effects. An oft-cited paper that implements this method in 2D for a Bingham plastic was published by Dorier and Tichy [40]. By using the generalised Reynolds equation they did not have to define separate equations for the different core cases, however, they did have to implement a regularisation of the Bingham plastic model to prevent convergence issues due to the discontinuity in the viscosity caused by the yield stress. Many similar publications, also ones using power law models and regularised variants of the Herschel-Bulkley relation, can be found in literature [23, 63, 71–74]. It should be noted that while this approach does not require multiple equations for the different core cases, a (slightly) modified version of the original problem is being solved in case a yield stress is used, because of the regularisation that has to be applied to those viscosity models. It is also known that regularisation of yield stress viscosity models can lead to incorrect predictions for the location of the core [75]. Furthermore, the solution process is computationally expensive for this approach, due to several integral terms in the generalised Reynolds equation that are evaluated numerically in most papers. Lampaert and van Ostayen found analytical solutions for these integrals in the case of a Bingham plastic, drastically reducing the required computation time [76]. By tracking the location of the core they also managed to circumvent the need for regularisation, while still only having one equation for all cases of core formation.

A final approach of including non-Newtonian effects in lubrication problems is to use CFD, solving the full 3D Navier-Stokes equations. This has been done by several researchers for various viscosity models, and generally gives good results [21, 39, 77]. The obvious disadvantage is that this method requires solving the Navier-Stokes equations, which is very computationally expensive.

In summary, there is quite a large body of research on the inclusion of non-Newtonian effects in the modelling of lubricating films. However, as far as the authors have been able to find, there is a lack of fast, 2D Reynolds equation based implementations using non-regularised viscosity models (other than Bingham plastic). The goal of this paper is therefore to show that it is possible to speed up the solution process of the generalised Reynolds equation in combination with an exact, non-regularised Herschel-Bulkley viscosity model, following a method similar to the one employed by Lampaert and van Ostayen [76]. To make the resulting model more relevant to real world (journal) bearings, mass-conserving cavitation will be taken into account as well.

3.2 Method

In this paper, the generalised Reynolds equation introduced by Dowson [70] is used as the basis for modelling a laminar thin film flow of a Herschel-Bulkley fluid. The method section will first introduce the characteristics of these specific non-Newtonian fluids, followed by a derivation of the generalised Reynolds equation. Next, a more efficient way of solving this equation in combination with a Herschel-Bulkley fluid is derived. Finally, the numerical implementation in COMSOL Multiphysics® [51] will be discussed and validated.

The bearing geometry that will be analysed in this paper is shown in figure 3.1.

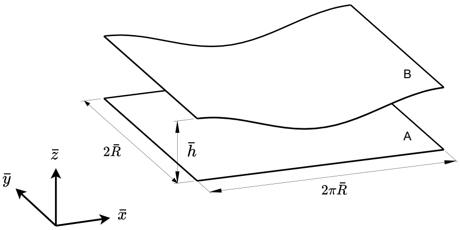

Figure 3.1: Schematic overview of the problem geometry, in this case for a journal bearing. The two surfaces are marked as A and B.

3.2.1 Herschel-Bulkley viscosity model

The governing equations and boundary conditions in this paper are made dimensionless using the groups below. The quantities with a bar (e.g. $\bar{x}$) have dimensions, the quantities without bar are dimensionless. Note that similar notation is used for 2D vectors with an x and y component, which are indicated with an arrow (e.g. $\vec{\tau}$).

$$x = \frac{\bar{x}}{\bar{R}},\quad y = \frac{\bar{y}}{\bar{R}},\quad z = \frac{\bar{z}}{h\bar{h}_0},\quad h = \frac{\bar{h}}{\bar{h}_0},\quad \eta = \frac{\bar{\eta}}{\bar{\eta}_0},\quad u = \frac{\bar{u}}{\bar{u}_0},$$

$$p = \frac{\bar{h}_0^2}{\bar{\eta}_0\bar{u}_0\bar{R}}\bar{p},\quad \tau = \frac{\bar{h}_0}{\bar{\eta}_0\bar{u}_0}\bar{\tau} = T_\tau\bar{\tau},\quad q = \frac{1}{\bar{h}_0\bar{u}_0}\bar{q}$$

Here x and y denote the in-plane coordinates, z the coordinate normal to the lubrication film, h the local film height, η the viscosity, u the fluid velocity, p the pressure, τ the shear stress, and q the flow rate. The z-coordinate is defined to be between 0 (for lower surface a) and 1 (for upper surface b). These quantities were made dimensionless using several constants, where $\bar{R}$ is the shaft radius, $\bar{h}_0$ the nominal film thickness, and $\bar{\eta}_0$ and $\bar{u}_0$ are reference values for the viscosity and velocity respectively.

The Herschel-Bulkley model is a non-Newtonian viscosity model that describes a fluid that has a yield stress and is either shear-thinning or shear-thickening for shear stresses above this critical yield stress. For this model the relation between the shear stress $\vec{\bar{\tau}}$ and the velocity gradient (the shear rate) $\partial\vec{\bar{u}}/\partial\bar{z}$ is described by equation 3.1, with the three parameters being the yield stress $\bar{\tau}_{yld}$, the consistency index $\bar{K}$, and the flow index m. When the shear stress is lower than the yield stress ($|\vec{\bar{\tau}}| < \bar{\tau}_{yld}$) the fluid is considered to be solid, and shear stress larger than the yield stress leads to viscous flow. The type of viscous flow is determined by the flow index, with the fluid showing pseudoplastic (shear-thinning) behaviour for $m < 1$, and dilatant (shear-thickening) behaviour for $m > 1$.

For $\bar{\tau}_{yld} \neq 0$ and $m = 1$ the Herschel-Bulkley model reduces to the Bingham plastic model. For $\bar{\tau}_{yld} = 0$ and $m \neq 0$ the model reduces to a power law model. Finally, when both $\bar{\tau}_{yld} = 0$ and $m = 1$, the model reduces to the Newtonian model.

$$|\vec{\bar{\tau}}| = \bar{\tau}_{yld} + \bar{K}\left|\frac{\partial\vec{\bar{u}}}{\partial\bar{z}}\right|^m \tag{3.1}$$

The Herschel-Bulkley model can be rewritten using equation 3.2, where both the shear stress factor f (equation 3.3) and the apparent viscosity η (equation 3.4) will be given as functions of the shear stress magnitude. This will prove useful later on in the derivation. The equations are made dimensionless at the same time.

$$f\vec{\tau} = \frac{\eta}{h}\frac{\partial \vec{u}}{\partial z} \tag{3.2}$$

$$\begin{aligned} f &= \left(1 - \frac{\tau_{yld}}{|\vec{\tau}|}\right)^{\frac{1}{m}} f^{*}\left(|\vec{\tau}|\right) \\ f^{*}\left(|\vec{\tau}|\right) &= \begin{cases} 1 & \text{if} \quad |\vec{\tau}| \geq \tau_{yld} \\ 0 & \text{if} \quad |\vec{\tau}| < \tau_{yld} \end{cases} \end{aligned} \tag{3.3}$$

$$\eta = \frac{\bar{K}^{\frac{1}{m}}}{\bar{\eta}_0}\left|\frac{\vec{\tau}}{T_\tau}\right|^{1-\frac{1}{m}} \tag{3.4}$$

3.2.2 Generalised Reynolds equation

This section presents the derivation of a generalised Reynolds equation that can be used to solve non-Newtonian lubrication problems. Following the derivation of Dowson [70], the linear momentum equation for a laminar thin film flow with negligible body and inertial forces is given by equation 3.5. In this equation $\vec{p}$ is the pressure, $\vec{\tau}$ is the shear stress, and $\vec{\nabla} = [\partial/\partial x, \partial/\partial y]$ is the gradient operator. Note that the dimensionless film thickness h appears only due to the non-dimensionalisation chosen in this paper.

$$\vec{\nabla} p = \frac{1}{h}\frac{\partial \vec{\tau}}{\partial z} \tag{3.5}$$

Integrating once over the film thickness coordinate z leads to an expression for the shear stress $\vec{\tau}$ (equation 3.6), with $\vec{\tau}_c$ the as of yet unknown integration constant.

$$\vec{\tau} = zh\vec{\nabla} p + \vec{\tau}_c \tag{3.6}$$

The next step is to substitute for $\vec{\tau}$ in this equation using equation 3.2, and to integrate over z again. Combined with the standard no-slip boundary conditions for the flow velocity ($\vec{u} = \vec{u}_a$ at $z = 0$ and $\vec{u} = \vec{u}_b$ at $z = 1$), this leads to equations 3.7 and 3.8 which represent the flow velocity $\vec{u}$ and the constant part of the shear stress $\vec{\tau}_c$ respectively ($\vec{\tau}_c$ is also the shear stress at $z = 0$). Note that it should also be possible to include slip boundary conditions without fundamentally changing the derivation that follows. For this, the reader is referred to [78], where Navier slip is added to the generalised Reynolds equation.

$$\vec{u} = h^2\vec{\nabla} p \int_0^z \frac{f}{\eta} z\,\mathrm{d}z + h\vec{\tau}_c \int_0^z \frac{f}{\eta}\,\mathrm{d}z + \vec{u}_a \tag{3.7}$$

$$\vec{\tau}_c = \frac{\vec{u}_b - \vec{u}_a}{hF_0} - h\frac{F_1}{F_0}\vec{\nabla} p \tag{3.8}$$

The flow factor integrals F_0 and F_1 that appear in equation 3.8 are defined by equation 3.9, where n can be either 0, 1 for F_0 and F_1, or 2 for F_2 which is used in the relations that follow.

$$F_n = \int_0^1 \frac{f}{\eta} z^n \mathrm{d}z \tag{3.9}$$

The flow rate through a cross-section of the film $\vec{q}$ can be obtained by integrating the flow velocity $\vec{u}$ over the channel height. Using integration by parts and substituting for $\vec{\tau}_c$ results in equation 3.10.

$$\vec{q} = -h^3 \left(F_2 - \frac{F_1^2}{F_0} \right) \vec{\nabla} p + h \left(1 - \frac{F_1}{F_0} \right) \vec{u}_b + h \frac{F_1}{F_0} \vec{u}_a \tag{3.10}$$

Finally, substituting for $\vec{q}$ in the mass balance equation (equation 3.11) will result in the generalised Reynolds equation. Here ψ is the lubricant fraction that is used to take cavitation into account.

$$\vec{\nabla} \left(\psi \vec{q} \right) = 0 \tag{3.11}$$

Cavitation algorithm

In this paper, cavitation is modelled using the mass-conservative JFO boundary conditions [52]. These boundary conditions are implemented with a variable transformation that is used to replace both p and ψ with functions of a new variable ξ (equations 3.12 & 3.13). By assuming that at any point in the fluid film, the lubricant is either in a full film region ($p > 0$, $\psi = 1$) or in a cavitated region ($p = 0$, $0 \leq \psi < 1$), the Reynolds equation can be solved for a single variable ξ that represents either the pressure or the lubricant fraction, depending on its sign.

$$p = (\xi \geq 0)\xi \tag{3.12}$$

$$\psi = 1 + (\xi < 0) c_f \xi \tag{3.13}$$

A numerical stabilisation technique is required to properly solve the generalised Reynolds equation in combination with this cavitation algorithm. For that reason artificial diffusion will be used in both the streamline and crosswind directions (x and y). The amount of cavitation can be controlled with the transformation constant c_f. Appendix 3.A discusses the implementation of the numerical stabilisation algorithm, as well as an optimal value for c_f, resulting in equation 3.14 when assuming isotropic diffusion.

$$\vec{\nabla} \left(-h^3 \left(F_2 - \frac{F_1^2}{F_0} \right) \vec{\nabla} \xi + \psi h \left(1 - \frac{F_1}{F_0} \right) \vec{u}_b + \psi h \frac{F_1}{F_0} \vec{u}_a \right) = 0 \tag{3.14}$$

3.2.3 Analytical evaluation of flow factors integrals

The generalised Reynolds equation (equation 3.11) is sufficient to determine the pressure profile for a thin film flow of a non-Newtonian lubricant. This equation has to be solved together with the flow factor integrals (equation 3.9), since these integrals depend on the shear stress and therefore on the pressure gradient. As was discussed in the introduction, this calculation has been performed previously for various viscosity models, both

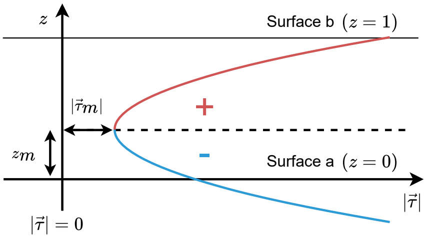

Figure 3.2: A schematic representation of the shear stress magnitude $|\vec{\tau}|$ over the film height. The minimum shear stress $|\vec{\tau}_m|$ and the z-coordinate of the minimum shear stress z_m are indicated. The red part of $|\vec{\tau}|$ (above $z = z_m$) corresponds to the positive solutions of equation 3.20, the blue part (below $z = z_m$) corresponds to the negative solutions.

with and without cavitation. However, in almost all of these papers the calculation of the flow factor integrals seems to be performed using numerical integration, and an analytical solution has only been found for Bingham fluids [76]. Since these integrals have to be evaluated at every single point in the domain, for every iteration of the solver, this is a fairly computationally expensive part of the calculation. In this section it will be shown that it is also possible to analytically evaluate the three flow factor integrals F_0, F_1 and F_2 for a Herschel-Bulkley fluid, removing the need for slow numerical integration.

In order to analytically evaluate the flow factor integrals, they have to be written to a different form. Currently these integrals, as given by equation 3.9, are integrated over the film thickness coordinate z. For the analytical evaluation it is necessary to rewrite them such that the integration is performed over the shear stress $|\vec{\tau}|$. This is done in equation 3.15, where $|\vec{\tau}_b|$ and $|\vec{\tau}_a|$ are the shear stress magnitudes on the upper and lower surfaces respectively.

$$F_n = \int_{|\vec{\tau}_a|}^{|\vec{\tau}_b|} \frac{f}{\eta} z^n \frac{\partial z}{\partial |\vec{\tau}|} \mathrm{d}|\vec{\tau}| \tag{3.15}$$

Evaluating equation 3.15 requires z as a function of $|\vec{\tau}|$, as well as the partial derivative $\partial z/\partial \tau$. To find these quantities, the shear stress magnitude should be determined first. This can be done using equation 3.6, and results in equation 3.16.

$$|\vec{\tau}|^2 = z^2 h^2 |\vec{\nabla} p|^2 + 2zh(\vec{\nabla} p \cdot \vec{\tau}_c) + |\vec{\tau}_c|^2 \tag{3.16}$$

With the (square of the) shear stress magnitude known, the z-coordinate of the minimum shear stress z_m can be determined (equation 3.17), as well as the minimum shear stress magnitude $|\vec{\tau}_m|$ (equation 3.18). See figure 3.2 for a visual representation of the shear stress magnitude and the minimum shear stress. Note that this transformation is ill-defined when $|\vec{\nabla} p| \longrightarrow 0$, which is the case (most notably) in the cavitation region. This case will be treated at the end of this section.

$$z_m = -\frac{\vec{\nabla} p \cdot \vec{\tau}_c}{h|\vec{\nabla} p|^2} \tag{3.17}$$

$$|\vec{\tau}_m|^2 = |\vec{\tau}_c|^2 - \frac{(\vec{\nabla}p \cdot \vec{\tau}_c)^2}{|\vec{\nabla}p|^2} \tag{3.18}$$

Equation 3.16 for the shear stress magnitude can now be rewritten using equations 3.17 and 3.18, resulting in equation 3.19.

$$|\vec{\tau}|^2 = |\vec{\tau}_m|^2 + h^2(z - z_m)^2|\vec{\nabla}p|^2 \tag{3.19}$$

Rewriting equation 3.19 then leads to z as a function of $|\vec{\tau}|$, which can be used to calculate the partial derivative $\partial z/\partial|\vec{\tau}|$ (equations 3.20 and 3.21 respectively). Because the shear stress magnitude is symmetric around the minimum shear stress, both equations have two solutions.

$$z = z_m \pm \frac{1}{h|\vec{\nabla}p|}\left(|\vec{\tau}|^2 - |\vec{\tau}_m|^2\right)^{1/2} \tag{3.20}$$

$$\frac{\partial z}{\partial|\vec{\tau}|} = \pm\frac{1}{h|\vec{\nabla}p|}\frac{|\vec{\tau}|}{\left(|\vec{\tau}|^2 - |\vec{\tau}_m|^2\right)^{1/2}} \tag{3.21}$$

Equations 3.20 and 3.21 can now be substituted into the flow factor integrals (equation 3.15). However, z and its derivative are both multivalued functions of $|\vec{\tau}|$, which means that these functions have two solutions for every value of $|\vec{\tau}|$. As a results, the bounds of the integral in equation 3.15 are not uniquely defined and the integral cannot be evaluated directly. The following paragraphs describe how to modify the integral such that it can be evaluated.

Since the shear stress magnitude has a minimum (equations 3.16 through 3.19), it is known that $|\vec{\tau}_m| \leq |\vec{\tau}| < \infty$. Therefore, instead of integrating directly from $|\vec{\tau}_a|$ to $|\vec{\tau}_b|$ as in equation 3.15, it is better to split the integral at $|\vec{\tau}_m|$, resulting in equation 3.22.

$$F_n = \int_{|\vec{\tau}_m|}^{|\vec{\tau}_b|} \frac{f}{\eta} z^n \frac{\partial z}{\partial|\vec{\tau}|}\mathrm{d}|\vec{\tau}| - \int_{|\vec{\tau}_m|}^{|\vec{\tau}_a|} \frac{f}{\eta} z^n \frac{\partial z}{\partial|\vec{\tau}|}\mathrm{d}|\vec{\tau}| \tag{3.22}$$

Looking at equation 3.20 with the knowledge that $|\vec{\tau}_m| \leq |\vec{\tau}| < \infty$, it is clear that the positive solutions corresponds to $z_m \leq z < \infty$, and the negative solutions to $-\infty < z \leq z_m$. This means that for the integrals in equation 3.22, the sign of z and $\partial z/\partial|\vec{\tau}|$ depends only on the z-coordinate of the surface represented by the upper bound of the integrals. Taking the situation in figure 3.2 as an example, here upper surface b lies above z_m, meaning that the first integral in equation 3.22 requires the positive solutions of z and $\partial z/\partial|\vec{\tau}|$. Meanwhile, the second integral requires the negative solutions, since lower surface a lies below z_m.

For this reason, equation 3.22 can be rewritten to equations 3.23 through 3.27. Equation 3.26 shows that the ± signs from equations 3.20 and 3.21 have been replaced with the sgn function, which is equal to 1 for a positive argument, and −1 for a negative argument.

$$F_0 = f_0 \tag{3.23}$$

$$F_1 = f_1 + z_m f_0 \tag{3.24}$$

$$F_2 = f_2 + 2z_m f_1 + z_m^2 f_0 \tag{3.25}$$

$$f_n = \left(\frac{1}{h|\vec{\nabla} p|}\right)^{n+1} \left(\mathrm{sgn}(1 - z_m)^{n+1} g_n\left(|\vec{\tau}_b|\right) - \mathrm{sgn}(0 - z_m)^{n+1} g_n\left(|\vec{\tau}_a|\right)\right) \tag{3.26}$$

$$g_n(\tau) = \int_{|\vec{\tau}_m|}^{\tau} \frac{f}{\eta} |\vec{\tau}| \left(|\vec{\tau}|^2 - |\vec{\tau}_m|^2\right)^{\frac{n-1}{2}} \mathrm{d}|\vec{\tau}| \tag{3.27}$$

One final step that is necessary for the analytical evaluation of the flow factor integrals given by equation 3.27 concerns the lower bound of the integrals, $|\vec{\tau}_m|$. Since a Herschel-Bulkley fluid has a yield stress, it is possible for the minimum shear stress to be lower than the yield stress ($|\vec{\tau}_m| < \tau_{yld}$). However, for the analytical evaluation to be possible, the assumption has to be made that both bounds of the integral are larger than τ_{yld}. To ensure this, and knowing that $f = 0$ for any $|\vec{\tau}| < \tau_{yld}$ (equation 3.3), the lower bound of equation 3.27 will be replaced by $|\vec{\tau}_p|$ which is defined by equation 3.28.

$$|\vec{\tau}_p| = \begin{cases} |\vec{\tau}_m| & \text{if} \quad |\vec{\tau}_m| \geq \tau_{yld} \\ \tau_{yld} & \text{if} \quad |\vec{\tau}_m| < \tau_{yld} \end{cases} \tag{3.28}$$

Using equation 3.28 and substituting for f and η (from equations 3.3 and 3.4 respectively), equations 3.26 and 3.27 can now be changed to equations 3.29 and 3.30.

$$f_n = \frac{T_\tau \bar{\eta}_0}{(\bar{K} T_\tau)^{\frac{1}{m}}} \left(\frac{1}{h|\vec{\nabla} \vec{p}|}\right)^{n+1} \left(\mathrm{sgn}(1 - z_m)^{n+1} g_n\left(|\vec{\tau}_b|\right) - \mathrm{sgn}(-z_m)^{n+1} g_n\left(|\vec{\tau}_a|\right)\right) \tag{3.29}$$

$$g_n(\tau) = \int_{|\vec{\tau}_p|}^{\tau} \left(|\vec{\tau}| - \tau_{yld}\right)^{\frac{1}{m}} \left(|\vec{\tau}|^2 - |\vec{\tau}_m|^2\right)^{\frac{n-1}{2}} f^*(\tau) \, \mathrm{d}|\vec{\tau}| \tag{3.30}$$

Note that equation 3.30 contains the f^* term from equation 3.3. As a results, if either $|\vec{\tau}_a|$ or $|\vec{\tau}_b|$ is smaller than the yield stress τ_{yld}, the corresponding integral $g_n(\tau)$ will be equal to zero. In a real bearing this would be the situation where the solid part of the fluid adheres to the surface where the shear stress is lowest.

The integral given by equation 3.30 has been integrated analytically using a software package for symbolic mathematical computation [79]. The indefinite variant of equation 3.29 was evaluated for $n = 0$, 1 and 2, resulting in equations 3.31, 3.32 and 3.33 respectively.

$$g_0(\tau) = \left[\frac{\left(|\vec{\tau}| - \tau_{yld}\right)^{1+\frac{1}{m}}}{1 + \frac{1}{m}} \left(\frac{1}{\tau_{yld}^2 - |\vec{\tau}_m|^2}\right)^{\frac{1}{2}} \mathrm{AppellF1}\left(1 + \frac{1}{m}, \frac{1}{2}, \frac{1}{2}, 2 + \frac{1}{m}, x', y'\right) \right] \Bigg|_{|\vec{\tau}_p|}^{\tau} \tag{3.31}$$

$$g_1(\tau) = \frac{\left(|\vec{\tau}| - \tau_{yld}\right)^{1+\frac{1}{m}}}{1 + \frac{1}{m}} \Bigg|_{|\vec{\tau}_p|}^{\tau} \tag{3.32}$$

$$g_2(\tau) = \left[\frac{\left(|\vec{\tau}| - \tau_{yld}\right)^{1+\frac{1}{m}}}{1 + \frac{1}{m}} \left(\frac{1}{\tau_{yld}^2 - |\vec{\tau}_m|^2}\right)^{-\frac{1}{2}} \mathrm{AppellF1}\left(1 + \frac{1}{m}, -\frac{1}{2}, -\frac{1}{2}, 2 + \frac{1}{m}, x', y'\right) \right] \Bigg|_{|\vec{\tau}_p|}^{\tau} \tag{3.33}$$

$$\begin{aligned} x' &= \frac{-|\vec{\tau}| + \tau_{yld}}{|\vec{\tau}_m| + \tau_{yld}} \\ y' &= \frac{|\vec{\tau}| - \tau_{yld}}{|\vec{\tau}_m| - \tau_{yld}} \end{aligned} \tag{3.34}$$

These analytical evaluations of the integrals are valid considering the following assumptions:

1. $\tau_{yld} \geq 0$
2. $|\vec{\tau}_m| \geq 0$
3. $|\vec{\tau}| \geq \tau_{yld}$
4. $|\vec{\tau}| \geq |\vec{\tau}_m|$

Finally, before continuing with the analysis of the resulting equations, it should be noted that the analytical evaluation of the flow factor integrals is not possible in the limit where $|\vec{\nabla}p| \longrightarrow 0$. However, it is not necessary either, since in this case the shear stress is constant ($|\vec{\tau}| = |\vec{\tau}_c|$, see equation 3.16), which means f and η are constant as well and can be moved outside of the integral in equation 3.9. The integral then becomes trivial to solve, resulting in equation 3.35, which can be used to calculate the flow factors in the cavitation region.

$$F_n = \frac{1}{n}\frac{f(|\vec{\tau}_c|)}{\eta(|\vec{\tau}_c|)} \quad \text{if} \quad |\vec{\nabla}p| = 0 \tag{3.35}$$

Appell F1 function

It turns out that while the analytical evaluation for g_1 is trivial, the evaluations for g_0 and g_2 are more complicated. These depend on the Appell hypergeometric function of the first kind, AppellF1($\alpha, \beta, \beta', \gamma, x', y'$), which is well-defined by an infinite series [80]. In literature, Appell functions have for example been found in the solution of integrals appearing in Feynman diagrams from quantum mechanics [81], and in the Watson integrals that characterise lattice random walks in biology [82].

Implementing the Appell F1 function using the infinite series is a complex procedure, since the series is only convergent for $|x'| < 1$ and $|y'| < 1$. Additional mathematical analysis is required to evaluate this series for other values of x' and y', and only one example of such an implementation could be found in literature [83]. An alternative method has been used in this paper, which solves a simple integral representation [84, 85] of the Appell function 3.36. In this equation Γ is the standard gamma function.

$$\text{AppellF1}(\alpha, \beta, \beta', \gamma, x', y') = \frac{\Gamma(\gamma)}{\Gamma(\alpha)\Gamma(\gamma-\alpha)} \int_0^1 w^{\alpha-1} w^{\gamma-\alpha-1} (1 - wx')^{-\beta} (1 - wy')^{-\beta'} \,\mathrm{d}w \tag{3.36}$$

This integral is valid as long as the conditions below are satisfied, which is the case for all positive values of the flow index m (see equations 3.31 and 3.33).

1. $\Re(\alpha) > 0$
2. $\Re(\gamma - \alpha) > 0$

A disadvantage of the integral representation is that numerical integration will be required to solve the Appell function. The analytical evaluation of the flow factor integrals is therefore no longer fully analytical, seemingly defeating its purpose. However, the Appell function is a known and well-defined mathematical function (in contrast to the flow factor integrals themselves). The use of the integral representation and numerical integration to calculate it, is therefore purely a limitation imposed by the poor availability of faster Appell function implementations based on the infinite series.

In order to show the potential of the analytical evaluation of the flow factor integrals in combination with a fast Appell function, lookup table approximations of the function were created. Two Appell function lookup tables are required, one for equation 3.31 where $\beta = \beta' = 0.5$, and one for equation 3.33 where $\beta = \beta' = -0.5$. For the creation of these lookup tables, the flow index m was assumed to be constant (different values of m will therefore require the lookup tables to be recalculated). The remaining arguments, x' and y', can vary between $-\infty < x' \leq 1$ and $-\infty < y' < \infty$ respectively (see equation 3.34). For the lookup tables the range of these variables will be limited to $-1 \times 10^{-4} < x' \leq 1$ and $-1 \times 10^{-4} < y' < 1 \times 10^{-4}$, which was found to be sufficient for the simulations carried out in this paper (equation 3.36 will be solved numerically at runtime for values of x' and y' outside of this range). The tables contain 240 by 480 values (for x' and y' respectively), which logarithmically approach the singular point (1,1) to within 1×10^{-6}. Cubic spline interpolation is used to find values that are not contained in the table. Finally, this results in two 2D lookup tables of x' and y' which are both valid for a single value of m. Accessing these tables takes a fraction of the time that is required for numerical integration, and will therefore allow for fast solutions to the generalised Reynolds equation.

3.2.4 Software implementation

The system of equations that describe a Herschel-Bulkley lubrication film are solved using the commercial FEM software package COMSOL Multiphysics® 6.1 [51]. Two variants of this model are solved in this paper. Both variants solve the generalised Reynolds equation (equation 3.14) for the pressure p, this equation is implemented in COMSOL using a General Form PDE. In addition, the first variant, the numerical variant, solves equation 3.9 for the flow factor integrals F_0, F_1 and F_2. The integrals are evaluated using COMSOL's numerical integration routine `integrate`. The second variant, the analytical variant, instead solves equation 3.9 together with equations 3.23 through 3.25 for F_0, F_1 and F_2. In this case the integral is evaluated analytically, and the resulting Appell functions are evaluated using lookup tables (see section 3.2.3). In both cases Dirichlet boundary conditions are used to set the pressure on the outer edges of the computational domain to zero. Furthermore, the symmetry of the bearing along the midline ($y = 0.5$) is used to find the pressure for only one half of the bearing.

The same solver strategy with two steps is used for both variants. In both cases, equation 3.14 is solved in step 1 for a Newtonian fluid, with $F_0 = 1$, $F_1 = 1/2$ and $F_2 = 1/3$. This Newtonian solution is then used as an initial guess for the Herschel-Bulkley solver in step 2, which solves for both the generalised Reynolds equation and the flow factor integrals at the same time. The flow factor integral derivatives are not included in the Jacobian matrix[1], which was found to result in much better convergence. The solver therefore simply

---

[1] In COMSOL this can be achieved with the `nojac` operator.

Table 3.1: Overview of the two sets of operating conditions used for the validation of the model, as well as the conditions for the test case used to compare the numerical and analytical variants of the model.

	Figure 3.3	Figure 3.4	Test case	Unit
$\bar{D}$	100	50	50	mm
L/D	4/3	1	1	-
$\bar{h}_0$	145.5	235	100	µm
$\bar{K}\&\bar{\eta}_0$	0.0127	-	0.1	Pa s
τ_{yld}	0	0.8	0.25	-
m	1	1	1.2	-
$\bar{\omega}$	48.1	-	26.2	rad/s
ϵ	0.61	0.31 - 0.71	0.3 - 0.7	-
ϕ	0	0	$\pi/4$	-
$\bar{p}_{cav}$	72 139.79	-	101 325	Pa

uses the flow factor function values from the previous step. A Newton-Raphson solver with under-relaxation is used for both steps, in step 1 the relaxation factor is determined automatically by COMSOL, in step 2 it is kept constant at a value of 0.2. Convergence is assumed when the relative solution and residual errors are smaller than 1×10^{-3}. The computational domain is discretised with a structured quadrilateral mesh, and unless mentioned otherwise the edge length of the elements is set equal to $h_e = 0.01$ (100x50 elements), which was found to be sufficient in mesh convergence checks using decreasing element size. Quadratic Lagrange shape functions are used.

The Appell function that is required for the analytical variant is calculated by solving equation 3.36 using the `integral` function of MATLAB [86]. The script that performs this calculation is based on an existing user-submitted implementation [87], and can be found at [88]. The lookup tables of the Appell function are made using the `griddedInterpolant` function in MATLAB. The resulting tables are created separately, before the model is solved, and are saved as .mat files. When the model is solved with COMSOL, the 'LiveLink for MATLAB' functionality can be used to call a MATLAB script that loads the lookup tables and returns the requested values of the Appell function.

3.2.5 Model validation

To validate the correct implementation of the equations, the numerical variant of the model will be compared with results found in literature for hydrodynamic journal bearings. No papers discussing the use of the isothermal Reynolds equation with a Herschel-Bulkley fluid model have been found, neither with nor without cavitation. For that reason the cavitation and non-Newtonian aspects of the model will be validated separately. In both cases the dimensionless film thickness h will be given by equation 3.37, where ϵ is the eccentricity of the shaft and ϕ the attitude angle.

$$h = 1 + \epsilon \cos(x - \phi) \tag{3.37}$$

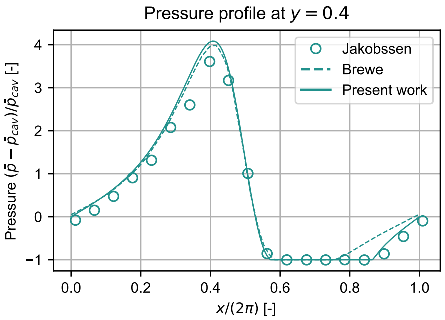

Figure 3.3: The pressure profile in a journal bearing lubricated with a Newtonian fluid and with cavitation taken into account. The operating conditions are shown in table 3.1. To match the dimensionless groups used in the figures from the references, the pressure is scaled with the cavitation pressure, $\bar{p}_{cav}$.

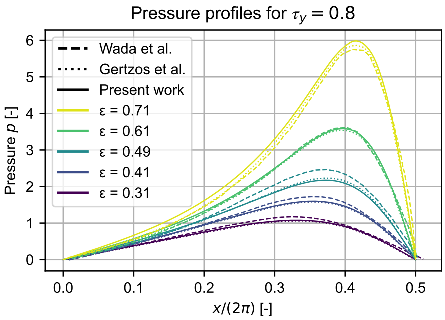

Figure 3.4: The pressure profiles for several eccentricities in a journal bearing lubricated with a Bingham fluid with cavitation implemented with the half-Sommerfeld boundary condition. The operating conditions are shown in table 3.1.

Figure 3.3 shows the pressure profile near the centreline of a journal bearing lubricated with a Newtonian lubricant, the operating conditions are shown in table 3.1. The model result is compared with the numerical result of Brewe[89] (who modelled cavitation using Elrod's algorithm [90]) and the experimental result of Jakobssen and Floberg [91]. The pressure profile determined by the numerical variant of the model shows good agreement with both results, and was found to be mesh convergent.

The second validation was performed for a journal bearing lubricated with a Bingham fluid, which is identical to a Herschel-Bulkley fluid with the flow index m equal to 1. The pressure profiles calculated by the numerical variant of the model for several eccentricities are shown in figure 3.4, the operating conditions can be found in table 3.1. For comparison, the numerical results obtained by Wada et al. and Gertzos et al. are shown [39, 66]. They implemented cavitation using the half-Sommerfeld condition, for that reason the cavitation implementation of the model was disabled and the pressure profiles are only shown for the full film region of the bearing ($0 \le x \le 0.5$). Agreement between the model and the results from literature is good, and the model was once again found to be mesh convergent.

3.3 Results and discussion

To show that the analytical variant of the model gives the same results as the numerical variant, but does so much faster, both models will be applied to the same test case. The operating conditions for this test case can be found in table 3.1, the test case describes a journal bearing at several different eccentricities lubricated with a Herschel-Bulkley fluid. The film thickness is once again given by equation 3.37. Figure 3.5 shows the resulting pressure profiles at the midline of the bearing for five different eccentricity values, and figure 3.6 shows the full 2D pressure profile for one of these eccentricities. The differences between the results of the numerical and analytical variants of the model are very

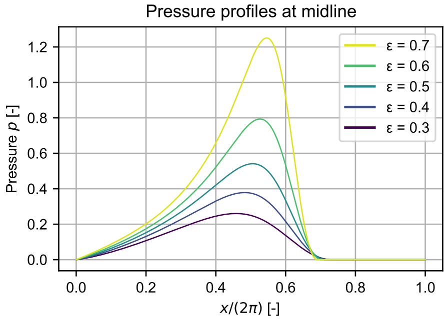

Figure 3.5: The pressure profiles for several eccentricities in a journal bearing lubricated with a Herschel-Bulkley fluid with cavitation taken into account. The operating conditions are shown in table 3.1.

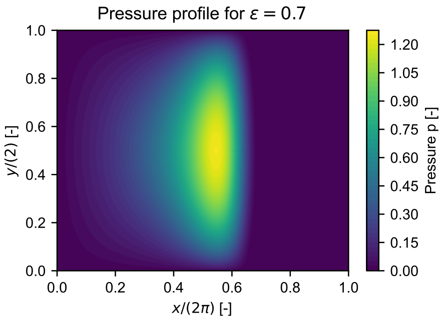

Figure 3.6: The 2D pressure profile for an eccentricity of 0.7, as calculated for a journal bearing lubricated with a Herschel-Bulkley fluid with cavitation taken into account. The operating conditions are shown in table 3.1.

Table 3.2: The relative differences in peak pressure and load capacity between the numerical and analytical variants of the model.

Eccentricity ε	0.3	0.4	0.5	0.6	0.7
Relative difference in peak pressure	1.55×10^{-5}	0.675×10^{-5}	0.118×10^{-5}	0.313×10^{-5}	0.113×10^{-5}
Relative difference in load capacity	3.268×10^{-7}	4.088×10^{-7}	1.200×10^{-7}	0.623×10^{-7}	1.290×10^{-6}

small, and cannot be distinguished using figure 3.5. For that reason the figure shows only the pressure profiles of one model variant, and the relative differences between the two variants are shown in table 3.2 for the peak pressure and load capacity, with the load capacity W being determined using equation 3.38[2].

$$W = \left(\left(\iint_S p \cos(x) \, \mathrm{d}A \right)^2 + \left(\iint_S p \sin(x) \, \mathrm{d}A \right)^2 \right)^{\frac{1}{2}} \tag{3.38}$$

The values in the table confirm that the differences between the variants are indeed small, though they are not zero. This can be explained by the limited accuracy of both the lookup tables, and of the numerical integration routine used in the numerical variant of the model. The accuracy of both could be increased to reduce these differences, but this would result in increasing storage sizes for the lookup tables, and increasingly long calculation times for the integration routine.

All results shown up to this point were calculated for a mesh size of $h_e = 0.01$, as was mentioned in section 3.2.4. To check if the results produced with this mesh size are accurate, it is necessary to establish whether the models are mesh-convergent. This is done using the load capacity, by comparing the FEM results of both model variants with a good estimate of the exact result. This estimate is obtained with Aitken's extrapolation method (also known as Aitken's δ^2-process), which uses three successive values in a converging

---

[2] *Footnote not present in original publication* - A small mistake was made in writing down this equation, the surface integral is written as $\iint_S$ which means the differentials should be written as $\mathrm{d}S$ instead of $\mathrm{d}A$.

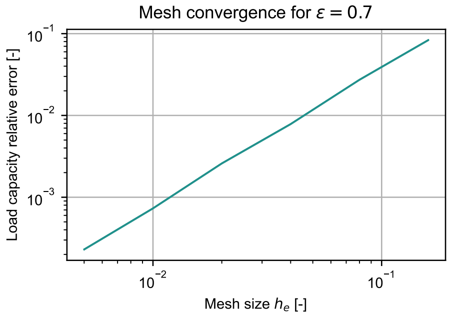

Figure 3.7: The relative error between the FEM-calculated load capacity and an estimate of the exact load capacity, as a function of the mesh size for an eccentricity of $\epsilon = 0.7$. Only the line for the analytical variant of the model is shown.

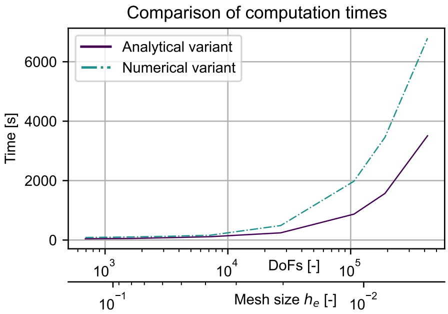

Figure 3.8: The computational time required to solve the analytical and numerical variants of the model for five different eccentricities. The x-axis indicates the number of degrees of freedom, as well as the corresponding mesh size.

series to calculate an improved estimate of the first value [92]. With this method, the relative error between the FEM-calculated load capacity and the Aitken estimate can be determined as a function of the mesh size. This error can be found in figure 3.7, proving that the models are indeed mesh-convergent, and that the results are sufficiently accurate with a mesh size of 0.01.

The previous results have shown that the analytical and numerical variants produce effectively identical pressure profiles. The only comparison left is therefore to check whether the analytical variant is faster, as was claimed at the start of this paper. The required computational times for both variants can be found in figure 3.8 as a function of the mesh size and the number of degrees of freedom. This figure shows the time required to solve the test case from table 3.1 for the five different eccentricity values from table 3.2. It is easily seen that the analytical variant of the model is indeed faster than the numerical variant, with the computational time being reduced by about a factor 2, independent of mesh size. This demonstrates that the approach used in this paper, where the flow factor integrals appearing in Dowson's generalised Reynolds equation were evaluated analytically for a Herschel-Bulkley fluid model, is an effective way of reducing the required computational time without losing any accuracy.

3.4 Conclusion

This paper presents a method for efficiently solving the pressure profile in a thin film flow of a non-Newtonian lubricant. Specifically, the 2D generalised Reynolds equation has been used to include shear-dependent viscosity effects, which were modelled with the Herschel-Bulkely model, allowing for both a yield stress as well as shear-thinning or shear-thickening effects. Similar studies exist in literature, however, those studies generally use computationally expensive numerical integration to evaluate several viscosity-dependent integrals that appear in the generalised Reynolds equation. Furthermore, the Herschel-Bulkley model is frequently regularised, to prevent convergence issues due to the discontinuity in the viscosity caused by the yield stress. It has been shown in this paper that these integrals can also be evaluated analytically, and without the use of regularisation. The resulting expressions depend on the so-called Appell F1 function, a well-defined but relatively obscure mathematical function. Due to a lack of fast and robust implementations of this function, pre-calculated lookup tables were used instead, which only have to be recalculated when the fluid properties are changed. The results produced by the final model (which includes mass-conserving cavitation) agree with literature, and show that the model produces effectively identical pressure profiles for both the numerically and analytically evaluated integrals without regularisation. The only difference being that the analytical variant does so about twice as fast, independent of mesh size. This decrease in computation time means that the model can be used more efficiently than the existing models, for example in design optimisation studies.

3.A Generalised Reynolds equation with cavitation

The cavitation algorithm used in this paper requires numerical stabilisation, otherwise the convection-dominated nature of the cavitated region will result in oscillations in the pressure solution. A simple and effective stabilisation technique is artificial diffusion (AD), which was used by Alakhramsing et al. to stabilise the standard Reynolds equation[52]. This paper follows their derivation, but applies it to the generalised Reynolds equation instead. Furthermore, isotropic diffusion will be used, with the diffusion coefficient for the x-direction (streamline) being applied to the y-direction (crosswind direction) as well. The amount of diffusion added to the crosswind direction will therefore be larger than necessary, but while the effect on the pressure solution was found to be minimal, convergence of the solver was much improved.

As was mentioned in the main text, a new variable ξ is used to model both the pressure p and the lubricant fraction ψ. The equations defining these relationships are repeated below.

$$p = (\xi \geq 0)\xi \tag{3.A.1}$$

$$\psi = 1 + (\xi < 0)c_f\xi \tag{3.A.2}$$

Using equation 3.A.1 to substitute for the pressure in the generalised Reynolds equation (equations 3.10 and 3.11) results in equation 3.A.3 in the x-direction. Here $u_{x,a}$ and $u_{x,b}$ are the x components of $\vec{u}_a$ and $\vec{u}_b$ respectively, and an artificial diffusion term k_{AD} is added to the cavitated region where $\xi < 0$.

$$\frac{\partial}{\partial x}\left(-\left(h^3\left(F_2 - \frac{F_1^2}{F_0}\right)(\xi \geq 0) + k_{AD}(\xi < 0)\right)\frac{\partial \xi}{\partial x} + \psi h\left(1 - \frac{F_1}{F_0}\right)u_{x,b} + \psi h\frac{F_1}{F_0}u_{x,a}\right) = 0 \tag{3.A.3}$$

The remainder of this derivation will focus on finding an optimal value for k_{AD} such that all oscillations are suppressed, without the introduction of excessive damping. The coefficient k_{AD} will be defined by equation 3.A.4.

$$k_{AD} = h_e u_{AD} \tag{3.A.4}$$

Here h_e is the typical size of the mesh elements, and u_{AD} the convection coefficient from equation 3.A.3. This term is defined by equation 3.A.5, where c_f is a transformation constant and c_{AD} is given by equation 3.A.6.

$$u_{AD} = hc_{AD}\left(\xi < 0\right)c_f \tag{3.A.5}$$

$$c_{AD} = \left(1 - \frac{F_1}{F_0}\right)u_{x,b} + \frac{F_1}{F_0}u_{x,a} \tag{3.A.6}$$

Equation 3.A.3 could now be solved by tweaking the amount of cavitation using c_f. However, it is known that the oscillations in the pressure solution will be the largest in the cavitated region near the reformation boundary. The minimal value for c_f should therefore be determined on this boundary. One way of doing this is to equate the flow rates at the reformation boundary as calculated in both the cavitated and full film regions ($q_{x,cav}$ and $q_{x,full}$ respectively, see equation 3.A.7). Substituting for $q_{x,cav}$ and $q_{x,full}$ results in equation 3.A.8, where it should be noted that $\xi \geq 0$ and $\psi = 1$ in the full film region.

$$q_{x,cav} = q_{x,full} \tag{3.A.7}$$

$$hc_{AD}\psi = -h^3\left(F_2 - \frac{F_1^2}{F_0}\right)\frac{\partial\xi}{\partial x} + hc_{AD} \tag{3.A.8}$$

One method for solving this equation is to expand the derivatives using numerical differences, as shown in equation 3.A.9. Here ξ_r is defined at point r in the cavitated region close to the reformation boundary, and ξ_{r+1} is defined at the neighbouring downstream point $r+1$ which lies in the full film region close to the boundary.

$$hc_{AD}(1 + c_f\xi_r) = -h^3\left(F_2 - \frac{F_1^2}{F_0}\right)\frac{\xi_{r+1} - \xi_r}{h_e} + hc_{AD} \tag{3.A.9}$$

Solving equation 3.A.9 for c_f results in equation 3.A.10. Since $\xi_{r+1} \geq 0$ in the full film region and $\xi_r < 0$ in the cavitated region, the minimum value of c_f that is required for numerical stability is given by equation 3.A.11.

$$c_f = \left(F_2 - \frac{F_1^2}{F_0}\right)\frac{h^2\left(1 - \frac{\xi_{r+1}}{\xi_r}\right)}{h_e c_{AD}} \tag{3.A.10}$$

$$c_f \geq \left(F_2 - \frac{F_1^2}{F_0}\right)\frac{h^2}{h_e c_{AD}} \tag{3.A.11}$$

This minimum value for c_f can now be applied to equation 3.A.3, using equations 3.A.4 and 3.A.5. Finally, repeating this process for the y-direction (crosswind direction) will results in equation 3.14. Note that the boolean terms that were still present in equation 3.A.3 have dropped out due to this choice of c_f.

4

Wear tests of MR-lubricated journal bearings

From the start of the project it has been clear that abrasive wear due to the presence of hard iron particles in the MR fluid was likely going to be problematic, especially during mixed or boundary lubrication. And indeed, the initial experimental tests described in chapter 2 already showed unacceptable levels of wear at higher loads, despite the fact that the bearing ran in the hydrodynamic regime for the vast majority of the time. This chapter therefore presents the results of a comprehensive study into the wear behaviour of MR-lubricated journal bearings for varying loads, fields, sleeve materials, and MR lubricants, with the aim of finding ways to reduce the wear rate to a level comparable with that of a standard oil-lubricated bearing.

Please note that the paper this chapter is based on is the result of a close collaboration with prof. dr hab. inż. Wojciech Litwin and dr hab. inż. Michał Wodtke from the University of Gdańsk. The wear tests (sections 4.4.1 through 4.4.5) were executed in Gdańsk, while the SEM analysis of the worn surfaces and particles (sections 4.4.6 and 4.4.7) was performed in Delft.

This chapter previously appeared as *M. Wodtke, W. Litwin, G. van der Meer, and R. van Ostayen*, 'Wear tests of hydrodynamic journal bearings lubricated with magnetorheological fluid', Wear, p. 206404, Oct. 2025.

Abstract

This research aimed to study the wear amount and mechanism of a hydrodynamic journal bearing lubricated with magnetorheological (MR) fluid. The effects of bearing load, hard particle content in the MR fluid, magnetic field activation, and bearing sleeve material were experimentally investigated. Results revealed that the standard bronze sleeve experienced extreme wear with MR lubrication, two orders of magnitude higher than for oil lubrication, while the friction coefficient was almost 6 times higher, probably due to severe third-body abrasion. The least amount of wear among all tested materials was observed with a more flexible polymer sleeve, which showed 3.5 times more wear than the oil-lubricated bearing and a smaller increase in friction coefficient, around 2.6 times, as well as the formation of a possibly protective layer of crushed particles in the converging region of the film. The results suggest that polymers, and possibly also softer materials such as rubber, are a promising alternative for bearings lubricated with MR fluids under low-speed and high-load conditions.

4.1 Introduction

Magnetorheological (MR) fluids fall under the category of smart materials. They comprise a homogeneous suspension, consisting of dispersed magnetic medium (particles) in a non-magnetic carrier (e.g., water or mineral oil) and additives. What makes MR fluids unique is that their rheological properties can be actively and rapidly changed by activating a magnetic field (adjusting magnetic flux density). The magnetic field causes the formation of magnetic particle chain structures in the fluid which significantly increase its viscosity and can cause a transition from fluid-like to solid-like properties [16, 93].

Due to strong development and research efforts, MR fluids found applications in many different mechanical devices, e.g., viscous couplings and clutches [94, 95], dampers [96, 97], or brakes [98, 99]. One mechanical component that can exploit the benefits of MR fluid capabilities is the fluid-film bearing. Depending on the application, they can operate with the principle of a hydrodynamic wedge, or with the squeeze effect or hydrostatic effect, using common hydraulic oils as a lubricant to separate mating surfaces. This is one of their biggest advantages, since the fluid completely separates the sliding surfaces of the components and friction takes place inside the lubricant instead of between the sliding surfaces in the form of dry or mixed friction. Here it is important to note that fluid friction is the desirable type of friction due to low losses and lack of wear. The application of MR fluids as a lubricant in fluid-film bearings is one of the possible solutions for smart (intelligent) bearings [100–102]. The operating characteristics of smart bearings can be actively controlled or adjusted depending on the forces acting on the system, or the sliding velocity in the system. In the case of a MR bearing, changing the lubricant viscosity during operation by activating and adjusting the magnetic field brings a very attractive possibility to eliminate one of the biggest limitations of hydrodynamic bearings application, namely the very limited load-carrying capability at low-speed operation. By locally activating a magnetic field, it is possible to increase locally the viscosity in the lubricating film, thereby increasing the minimum film thickness. This to ensure more favourable conditions for the safety of bearing operation at high loads and low shaft speeds.

Experimental investigations of MR journal bearing properties for steady-state operation have generally confirmed the theoretical findings [27, 28]. However, they revealed one limitation concerning journal speed; for high-speed values and thus for high values of MR fluid shear rates, the MR effect is significantly reduced (due to the shear-thinning effect) compared with the viscous effect [27, 37]. In [29] the possibility of eliminating this disadvantage by using a special MR bearing design with a floating ring for enhanced stiffness and damping of the bearing system was investigated. The experimental results showed that this bearing type remained controllable even when rotating at 1200rpm. The MR effect was investigated in a thrust bearing configuration in steady-state mode to validate the theoretical model and predict the axial force as a result of the magnetic field [103]. The application of MR fluid was also experimentally investigated in the hydrostatic mode of lubrication. In [104], using an electromagnet, the magnetic field was applied locally at the outer edges of the hydrostatic bearing. This caused an increase in resistance in the MR fluid flow at the fluid film outlet zone, mimicking the behaviour of geometric textures, which resulted in a pressure profile shape in the MR fluid film similar to the profile in a geometrically textured hydrostatic bearing.

The authors of this paper also conducted experimental research on journal bearings lubricated with MR fluid on two separate test stands with differing shaft diameters (50 and 100mm). Their results demonstrated that MR-lubricated hydrodynamic bearings can potentially solve problems of oil-lubricated bearings at high loads and low shaft speeds by ensuring locally tuned MR fluid viscosity [30]. It was also shown that applying a local magnetic field near the minimum film thickness can reduce losses to even lower values than those of the reference oil-lubricated bearing, while retaining a (small) increase in minimum film thickness [105]. However, after both investigations, clear signs of abrasive wear were noticed on the sliding surfaces of the MR-fluid lubricated bearing components. MR fluids are made of base oil and ferromagnetic, hard particles, which can influence bearing wear resistance, especially in mixed lubrication mode. This can be a huge disadvantage for MR bearings operating under low speed and high load, or for MR bearings experiencing frequent start/stop cycles. Others researches have also investigated wear problems for other sliding pairs utilising MR fluids, e.g. for O-ring sealings [106].

The effect of hard particles on lubrication performance has been investigated in the literature, as summarised in the works of Khonsari and Booser [107], and Nikas [108]. Their results showed that the particles dispersed in the lubricant worsen hydrodynamic performance by increasing friction losses, temperature, and wear on the sliding surface, which justifies the significance of proper filtration for the operation of lubricated surfaces [109]. The specific impact of iron particles dispersed in the lubricant (usually mineral oil) has been investigated experimentally as well [110–112]. The lubricant for such a case, in terms of the composition, was similar to MR fluid; however, it differed significantly in the iron particle content and size. Iron particle contamination in the reported tests varied from a handful of particles of large size (5 to 30 particles with sizes up to 1.4mm, [110]) to 40-50μm particles with a 0.05% concentration by weight [111, 112]. In contrast, the concentration of iron particles for MR fluid can reach 70% by weight with an average particle size of only a couple of microns.

The wear mechanism of MR-fluid lubricated contacts has been studied extensively [54, 55, 113–117]; however, they did so only experimentally on the sample level using different contact configurations on tribometers. Their results provided many valuable findings, such as that measured wear and coefficient of friction for MR fluid-lubricated contacts were higher than for hydraulic oil [55] or that an increase in particle content in the MR fluid increased friction losses [54]. On the other hand, some contradictory conclusions concerning the effect of the magnetic field activation on tribological properties of MR-fluid lubricated sliding contacts were formulated in [113] and [114]. In [113], using a pin-on-disc tribometer, the MR fluid under a magnetic field shows better friction and wear properties compared to the absence of a magnetic field, while in the results of [114], utilising a four-ball tribological tester, the opposite trend was noticed. Most likely, these differences were due to the different geometry of the tested sliding pairs. Moreover, the effect of mating surface material [113] and material of the particles [115] on tribological performance was also studied, as well as comparative investigations with the tribological properties of other smart fluids, e.g. ferrofluids [116]. Finally, different types of solid lubricants added to silicone-based MR-fluid (e.g. PTFE, boron nitride, MoS2 or graphite) were also investigated for the tribological performance using a four-ball geometry tribometer [117]. The results show that when MoS2 was added to the MR fluid, the highest reduction in frictional force was obtained, while the addition of PTFE resulted in the least wear of the test samples. Several investigations also noticed that due to operation in mixed friction under tribological tests, not only were tested samples worn, but iron particles dispersed in MR fluid deformed and changed their initial shapes [54, 55, 113, 118]. Wear of the MR fluid can also be an additional limitation for the long-term operation of the MR-bearing system operating under mixed friction mode.

The literature lacks wear test investigations under MR-fluid lubrication carried out on the component of interest in this paper, namely using hydrodynamic bearings. According to the authors' previous experimental results, this is one of the biggest challenges limiting the possibility of applying MR-lubricated bearings in low-speed conditions. This paper intents to fill that knowledge gap and reports the results of comprehensive tribological research on hydrodynamic bearings lubricated with MR fluid.

4.2 Goal of the research

This research aims to study the wear properties (wear mechanism and wear amount) of the components of a hydrodynamic bearing under varied bearing loads and operated with different MR lubricants, both with and without an activated magnetic field. Moreover, it aims to identify bearing sleeve materials capable of reducing the wear amount under MR lubrication to a level comparable to that of oil-lubricated bearings. For this comprehensive research project, an experimental study was conducted on a bearing system lubricated with standard and customised MR fluid. The research program involved long-time start / stop tests to assess the wear of the shafts and sleeves of the bearings. The wear assessment was based on the sliding surface geometry measurements before and after the tests. The sliding surfaces of the bearing sleeves and shaft journals were also examined using a scanning electron microscope (SEM) with integrated energy dispersive X-ray spectroscopy (EDS) to investigate the wear mechanisms and to check for possible material transfer between the two mating surfaces, and between the mating surfaces and the particles. SEM was also used to investigate the size and shape of the particles dispersed in the MR-fluid before and after the wear tests.

4.3 Method

4.3.1 Lubricant properties

The wear tests were carried out using three different lubricants, one mineral oil that was used as a reference, and two hydrocarbon-based MR fluids with different particle concentrations. For the reference measurements a standard maritime lubricating oil, Castrol MHP 153 (SAE 30), was used. The MR measurements were carried out with the standard MR fluid MRHCCS4-A with 70% particle concentration by weight [119], as well as a variant of the same fluid with 20% particle concentration by weight, which was designed at request by the same manufacturer. From now on these MR fluids will be referred to as 'MR 70%' and 'MR 20%' respectively. The particle size distributions for both MR fluids were measured as well, see section 4.3.4 for the methodology and section 4.4.6 for the results. Do note that a different batch of smaller particles was used to create the MR 20% fluid, and that the manufacturer indicated qualitatively that these particles were of a higher hardness than the particles used in the MR 70% fluid.

Figure 4.1 shows several viscosity plots for these three lubricants. Figure 4.1a shows

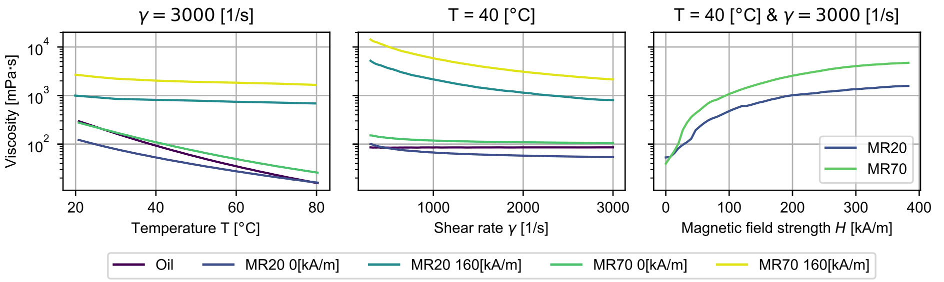

(a) Viscosity as a function of temperature for a constant shear rate.

(b) Viscosity as a function of shear rate for a constant temperature.

(c) Viscosity as a function of magnetic field strength for a constant temperature and shear rate.

Figure 4.1: Viscosity measurements for the three lubricants used in this paper.

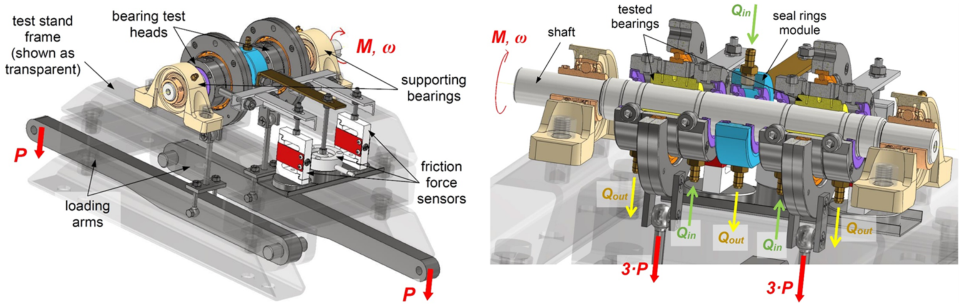

(a) General view showing the friction measurement and loading systems

(b) Detailed view (cross section)

Figure 4.2: Tests stand applied for wear tests.

viscosity as a function of temperature, for the MR fluids curves both with and without a magnetic field present are shown (figure 4.1). Furthermore, since the MR fluids are strongly shear-thinning, figure 4.1b shows the viscosity of all lubricants as a function of shear rate. Finally, figure 4.1c shows the change in viscosity when uniform magnetic fields of different strengths are applied to the two MR fluids. All viscosity measurements were performed with an Anton Paar MRC 302 rheometer with a cone on plate geometry.

4.3.2 Wear test setup

The custom-designed and built test rig for the wear test of the journal bearings with a 30mm diameter shaft is presented in figure 4.2. Two tested journal sliding bearings and a seal rings module were installed on the main shaft. Supporting roller element bearings guided the main shaft in self-alignment housings. The lever system with the ratio 3:1 exerted a radial load (3P) with the weights (P) on the bearings under test through additional ball bearings (marked in orange). This ensured that frictional losses in tested bearings could be measured (assuming that the small friction in the ball bearings can be neglected). Two force sensors with beams connected to testing bearing heads were used to meas-

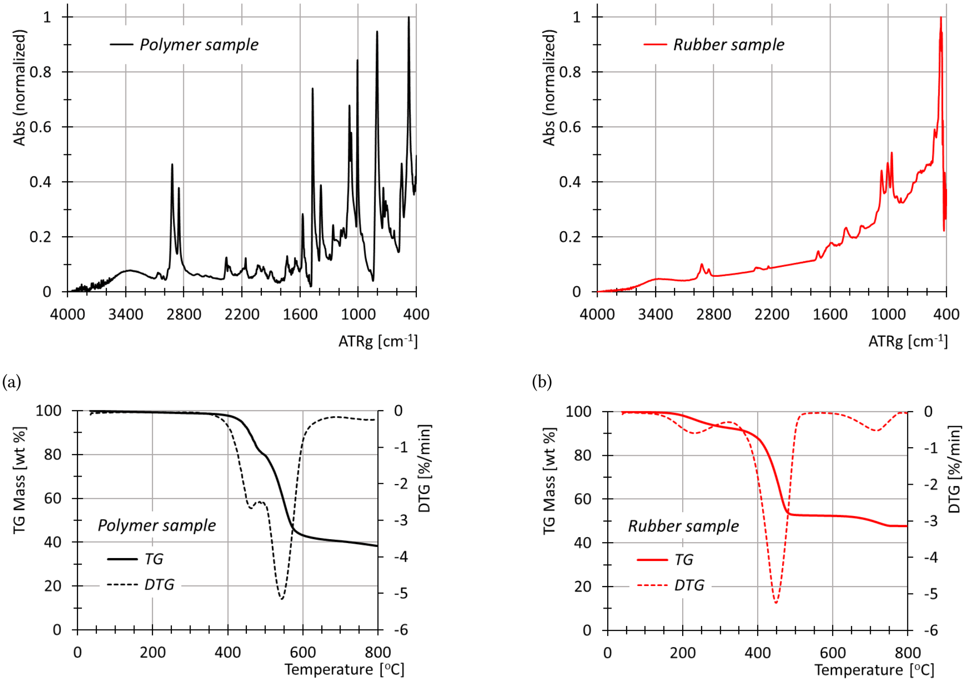

(a)

(b)

(c)

(d)

Figure 4.3: FTIR (a & b) and TG and DTG (c & d) curves of tested bearing material samples.

ure friction losses under operation (see figure 4.2a). The measured friction forces were losses in the tested bearing (yellow in figure 4.2b) and its sealing (violet colour). Sealing losses were measured using a separate force sensor and a cantilever beam connected to the seal module containing lip seals of the same design as those applied to test heads. This measurement was used as a correction to obtain friction in the tested bearings. During the tests, bearing temperature was monitored using two 1mm diameter K-type thermocouples. Thermocouples were inserted into blind holes drilled radially close to the bearing ends on its loaded side, with measuring tips positioned 2mm below the sliding surface (see figure 4.5a).

A peristaltic pump with a small tank (1L) equipped with a mixer (to keep the lubricating MR fluid homogenous) was used to feed bearings. The lubricant was pumped separately to both heads (see figure 4.2b); Qin = $40\,\mathrm{mL\,min^{-1}}$) and the seal module (to ensure similar conditions for the sealing operation). The lubricant was supplied to the heads from one end of the bearing. It flowed axially through the bearings, with two open lubrication grooves (axial) located in the horizontal plane. The lubricant was discharged on the other bearing side and collected in a tank. One wear test consisted of 8600 cycles of start / stop tests with a data recording frequency of 1Hz (mean value of 1k samples per second). Each cycle lasting 15 seconds contained forced start-up, steady state operation and free run shutdown. Since the effect of material on the MR fluid-lubricated bearing system wear

Table 4.1: Data on the bearings, materials and operational conditions.

Diameter of the shaft / Length of the bushing	30mm / 30mm
Bearing clearance (@ 20°C)	0.15mm
Radial load (3P) [N] / specific pressure [MPa]	1800N / 2MPa or 900N / 1MPa
Shaft material / surface roughness	AISI 1045 - Carbon steel / Ra=0.32µm
Bearing sleeve material / surface roughness	Bronze CuSn7Zn4Pb7-C (2.1090) / Ra=0.63µm Polymer inserts / Ra=1.25µm Rubber (8 axial grooves evenly distributed)
Single cycle shaft speed	Cycle time 15s 2s start-up (0 ↗ 1000rpm) 10s steady-state (at 1000rpm) 3s free shut down (1000rpm ↘ 0) 1s of time interval between cycles
Friction torque – strain gauge sensor with amplifier, range 0-222N, accuracy ±0.05% R.O. Bearing temperature - K-type thermocouples, accuracy 1.5 K	

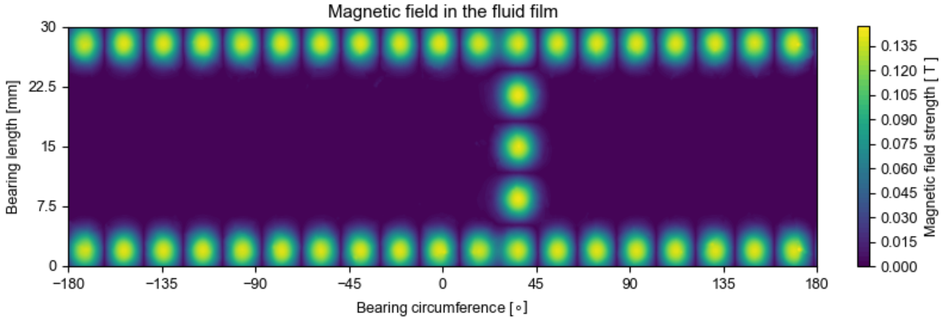

Figure 4.4: Sliding surface measurements, a) bearing sleeve; b) shaft; c) an example of measured geometry profiles of sliding surface and linear wear assessment.

process was investigated, bearings produced from different materials were tested. Bronze (CuSn7Zn4Pb7-C) was used as a base material in most tests. In addition, bearings made of a harder material (steel) and softer polymer (compressive modulus of elasticity 2.2GPa, hardness 83 shore D, melting point 260°C) and rubber (oil and chemical resistant nitrile rubber, hardness 70±3 shore) were also tested. Commercially available bearing sleeves made of polymer and rubber were selected, which are designated for applications that require operation under increased wear conditions. FTIR and TG (in a nitrogen atmosphere) methods were used to determine the composition of the soft bearing sleeves. The results of these measurements (figure 4.3) allowed to identify that the polymer sleeve material was a PPS-based polymer composite, and the rubber sleeve material was a Low-cis Butadiene-based rubber composite. For simplicity, they will be referred to further in the paper as polymer and rubber bearing sleeves.

In the case of polymer bearing, intermediate sleeves were used to assemble polymer inserts for tests. The tested rubber bearing had a different design (typical for water-lubricated bearings), with 8 axial grooves evenly distributed on the bearing perimeter. For shaft material, carbon steel (typical for ship shafts) was assumed to be used for all tests. Dimensions of tested bearings, materials and operation conditions were collected in table 4.1.

One series of tests focused on the effect of a magnetic field on the wear process. Therefore, 4mm diameter x 1mm thick magnets (magnet flux density = 1.03T) were installed in the tested sleeve 2mm below the sliding surface. They were arranged in two circumferential rows (each composed of 20 magnets) placed close to bearing ends (figure 4.5a), and one axial row (composed of 3 magnets) shifted 36° from the vertical direction in the vicinity of the expected minimum film thickness zone. The axial row is meant to effectively increases film pressure near the minimum film zone, while the circumferential rows should decrease MR-fluid leakages from the film at the bearing ends, thereby also increasing film pressure. Adjacent magnets were arranged in an alternating order (N – S – N – S – etc.), which, according to numerical analysis [105], results in a magnetic field that is smaller far away from the magnets (relative to the field close to the magnets) compared to a uniform orientation (e.g. N – N – N – N – etc.). This should focus the viscosity increase on the areas of the film directly below the magnets, while limiting the viscosity increase far away from the magnets and thereby reducing the friction losses.

The magnetic field resulting from this arrangement of magnets has been calculated numerically, and is shown in figure 4.4 This calculation was performed using a commercial software package for numerical simulation [51], and other than the bearing geometry (see table 4.1) the details of the implementation of the numerical model have been described in detail in a previous paper by the same authors [105].

4.3.3 Wear amount assessment methodology

The wear assessment of the tested components utilised a comparison of the surface geometry measurements before and after the tests. Measurements were conducted using a contact profilometer (Jenoptik Hommel Etamic T8000, measuring vertical range 400μm). To compare the profiles before and after tests, both shafts and bearings were manufactured with special reference surfaces in the shape of grooves, with the bottom surface below the sliding surface, to avoid their wear during operation (figure 4.5). The axial profiles of the mating surfaces started and finished each time at reference grooves. For each sleeve, several axial profiles were measured on the loaded bearing half (evenly distributed to the direction of the load, initially 5 paths in a range ± 30°, later 9 paths in a range ± 65°, figure 4.5a. Positioning holes made at the outer surface of the bearing, together with a pin mounted in the v-block groove, provided accurate (and repeatable) angular positions of the bearing for measurements. One axial profile was collected for each shaft journal in marked angular position since differences in measured geometries for other circumferential positions were negligible. Figure 4.5c shows an example of a measured sliding surface profile comparison. Since the geometry of the reference surfaces did not change during the wear test, it was possible to compare profiles. The difference in the average level of the sliding surface before and after the wear test was a measure of the linear wear. The same comparison was carried out for each angular position of the sleeve. As a result, a circumferential distribution of wear for the loaded half of the bearing was obtained. This

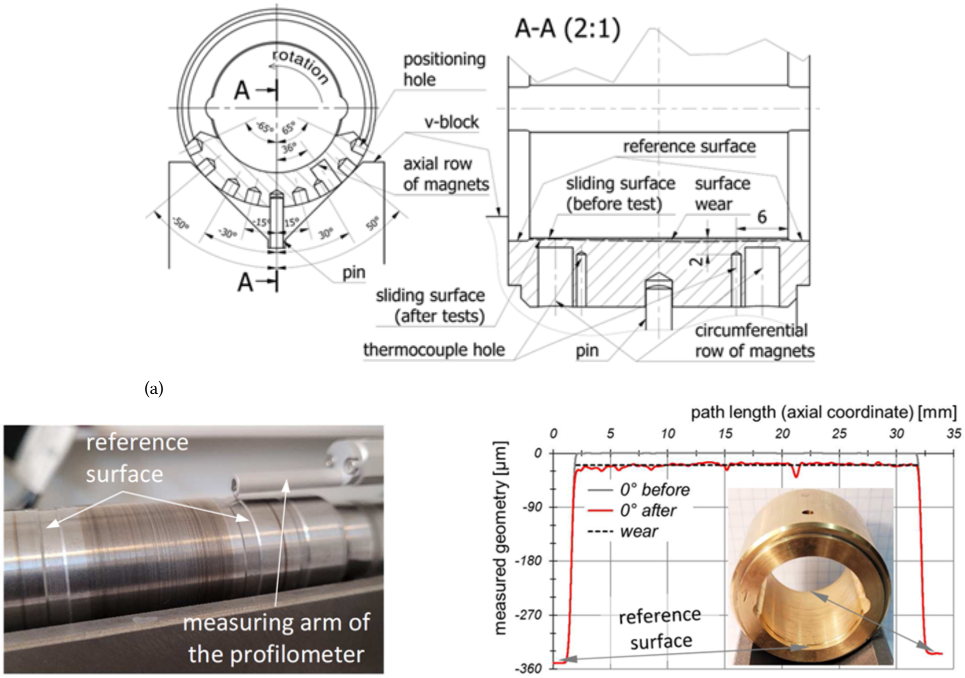

(a)

(b)

(c)

Figure 4.5: Sliding surface measurements: a) bearing sleeve, b) shaft, c) an example of measured geometry profiles of sliding surface and linear wear assessment.

distribution was also used to calculate the volumetric wear of the sleeves, assuming that the sliding surface was unfolded and changes in the wear between measurement points (namely path positions) were linear. In the case of shaft journals, volumetric wear was calculated as a difference in volume between a journal with nominal size (before the test) and one with a radius reduced by linear wear (after the test).

4.3.4 SEM analysis

A JEOL 6010LA scanning electron microscope (SEM) with integrated energy dispersive X-ray spectroscopy (EDS) functionality was used for two different investigations after the wear tests had been performed. First of all, micrographs of the shaft and bearing surfaces were created to investigate the wear mechanisms, and elemental analysis of the surfaces was performed using EDS to check for possible material transfer between the shafts, bearings, and particles. For this purpose, the shafts and bearings were cleaned by hand with isopropyl alcohol and were cut into smaller pieces, and before being placed in the SEM the non-conductive rubber and polymer bearing surfaces were coated with a thin layer of gold to improve the imaging results.

Secondly, the SEM was used to perform an analysis of the particle sizes before and after the wear tests. In order to extract the particles from the MR fluid, the fluid had to be destabilised using acetone. This was done by adding MR fluid and acetone in a 1:1 ratio to a container, which was placed in a shaker for 1 minute. After this minute, the container with the mixture was placed on a large NdFeB magnet, rapidly causing the particles to be pulled towards the magnet and leaving a mixture of acetone, oil, and additives floating on top. With the container still on the magnet the supernatant liquid was decanted, and this process was repeated until the decanted liquid started running clear. After drying, the particles were sprinkled on carbon tape to enable imaging with the SEM, resulting in micrographs containing thousands of particles. Image analysis software with particle analysis functionality [120] was used to find the particle size distribution based on these micrographs. This was done by first applying a median blur filter (blur radius 0.25μm) to denoise the micrograph, followed by an application of the Li threshold algorithm [121] to separate the particles from the background. Finally, the watershed algorithm was used to separate partially overlapping particles. This sequence of operations was qualitatively found to result in reasonable recognition of the particles by the particle analysis function.

4.4 Wear test results

During each wear test, two bearing sleeves and one shaft with two bearing journals were tested simultaneously. This allowed us to assess the repeatability of the process by comparing the wear results for components tested separately under the same operating conditions. The results showed that linear wear did not differ significantly between sleeves and journal shafts from one test. Consequently, the linear wear results presented in this section are averaged values obtained for the same component type (sleeve and shaft) in one test.

Wear tests were started for a system with bronze bearings under 2MPa of specific pressure loading and lubricated with the mineral oil Castrol MHP 153 (SAE 30) using the same methodology as planned for MR-lubricated bearings. The results obtained from this

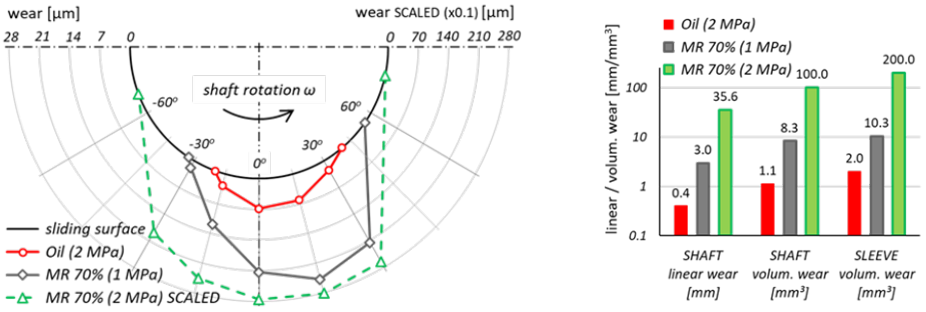

(a) (b)

Figure 4.6: Effect of the load on the wear of bearing components lubricated with MR fluid: a) distribution of the linear wear at the circumference of the sleeves, b) linear wear of the shaft journals and volumetric wear of the sleeves and shafts.

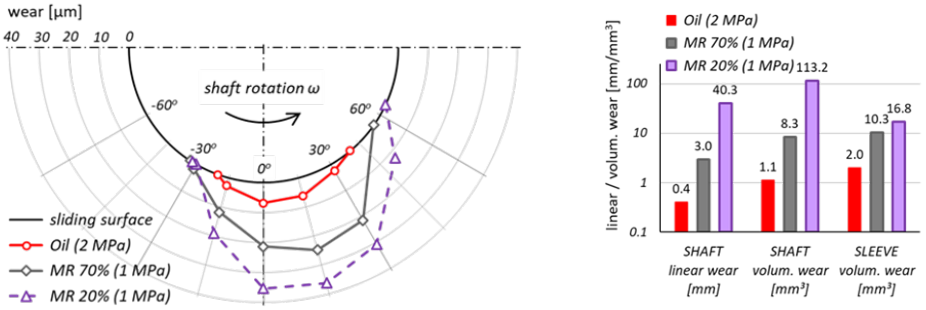

(a) (b)

Figure 4.7: Effect of the MR fluid type on the wear of bearing components: a) distribution of the linear wear at the circumference of the sleeves, b) linear wear of the shaft journals and volumetric wear of the sleeves and shafts.

test were used as reference values to assess the wear resistance of tested components with MR-fluid lubrication. The tests were planned and carried out so that it was possible to analyse the impact of a single parameter of the system on the process of component wear. The research plan covered the test focused on effects of bearing load, MR-fluid type, presence of magnetic field, and bearing material. Obtained results were shown and described in the following parts of this section (4.4.1 - 4.4.4).

4.4.1 Effect of the load

In the first series of experiments, bronze bearings lubricated with MR 70% were tested under the same conditions as in the reference case (under load of 2MPa). At this stage, magnets were not installed in the bearings, so no magnetic field acted on the fluid. The results showed a huge wear of components. Consequently, the next test was planned and carried out with the reduced bearing load (to 1MPa) to investigate the impact of this parameter on wear under MR-fluid lubrication.

In figure 4.6, a summary of the wear results for load effect under MR-fluid lubrication was presented and compared to results obtained for the reference case (oil-lubricated bearing). figure 4.6a presents measured circumferential distribution of linear wear for sleeves (note that results for MR 70% and 2MPa load were scaled – reduced by factor 10 - to fit them in the plot). In figure 4.6b measured wear for shaft journals and sleeves were compared. The circumferential distribution of the bearing sleeve wear was not symmetrical to the load direction (angular position of 0 degrees in figure 4.6a). This shape is typical (visible in all further results), as higher linear wear occurs near the minimum lubricant film thickness zone. Under the load of 2MPa, the volumetric wear of the bearing and journals lubricated with MR 70% was two orders of magnitude (!) higher than that of the reference case (figure 4.6b). After reducing the load to 1MPa, the wear of the components lubricated with MR 70% was also reduced; however, it was higher from 5 (for sleeves) to 7 times (for journals) than in the reference case.

4.4.2 Effect of the MR lubricant

The measured level of component wear lubricated with MR 70% fluid was unacceptable in the case of real bearing system operation. One reason for this can be the relatively high concentration of particles in the MR fluid that was applied as a lubricant in previous tests. To investigate the effect of MR lubricant with lower particle content on system wear, a new fluid, MR 20%, was developed and provided for testing. Wear tests, as previously, were carried out for bronze bearings under the load of 1MPa.

Figure 4.6 shows the measured wear distribution for sleeves (a) and journals (b) lubricated with MR 70% and MR 20% fluids compared to the reference case. Surprisingly, the volumetric wear of the sleeves lubricated with the MR 20% fluid with a lower concentration of the particles was significantly higher (about 60%) than for MR 70% lubrication. It was much worse in the case of journals since their wear was an order of magnitude higher than the wear of parts operated with MR fluid with a higher concentration of particles. In addition, it was even slightly higher than shaft journal wear, measured for MR at 70% under 2MPa load (see figure 4.6b).

4.4.3 Effect of the magnetic field

Activating the magnetic field (MF) is required to gain the unique benefits of MR lubrication (change of the lubricant viscosity and thus adjustment of bearing properties—active bearing principle). One of the tests evaluated the effect of MF presence on the bearing system components' wear. The test was carried out using bronze bearings with magnets assembled in the bearing body (as described in paragraph 4.3.2) and for a load of 1MPa.

Figure 4.8 shows the measured wear results for the bearing system components lubricated with MR 70% fluid with activated MF compared to the case without activated MF. The volumetric wear of the shaft journals was found to be higher while the MF was activated (less than 2 times higher). Simultaneously, the level of volumetric wear for the bearing sleeves operated with and without the magnetic field was the same. However, the angular wear range was slightly narrower (shorter) when the system was tested without an activated magnetic field.

4.4.4 Effect of the material

Parameter changes studied and described in previous parts of this chapter did not cause a reduction of the system component's wear lubricated with MR-fluid to a level similar to that observed for the reference case. The last of the studied parameters was the material of the bearing. Different types of materials were tried, with varied properties. One of them was steel, whose hardness is much higher than bronze, which was expected to be beneficial for wear reduction. However, tests with steel bearings lubricated with MR 70% fluid under the load of 1MPa failed catastrophically after several start/stop cycles, probably due to scuffing and the effect of having the same material for both mating surfaces. Thus, no results were available for this test.

In further tests, softer materials, such as polymer and rubber, were used. Polymer bearings tested were cylindrical plain bearings of the same design as tested bronze bearings. In the case of rubber bearings, due to the lack of availability of a design and size similar to the tested one, a typical design for water lubrication with 8 axial grooves distributed evenly around the bearing perimeter was tested. Tests were carried out under the load of 2MPa and with MR 70% as lubricant.

Figure 4.9 shows the wear results for different tested materials of the bearing sleeve. Since a reference surface could not be manufactured on the rubber bearings (the rubber was too soft, later on this also prevented accurate profile measurements with the profilometer), the proposed wear measurement method could not be used. Other wear assessment methods were considered for rubber bearings, such as the weight method or employing a Coordinate Measuring Machine (CMM); however, their accuracy was not satisfactory considering the level of wear on the components. Thus, the wear amount of the rubber bearings could not be determined.

The polymer volumetric wear was higher than the reference value for oil-lubricated bearings. However, the wear on polymer bearings was the smallest among all wear tests with MR fluid lubrication. In the case of the shaft, the wear of the journals operated against the polymer was higher than the reference (around seven times). Simultaneously, the volumetric wear of the journals after tests with rubber bearings was hardly measurable and even smaller than for oil-lubricated bearings.

4.4.5 Coefficient of friction (COF) and temperature

In figure 4.10, the measured coefficient of friction (COF) obtained during all wear tests reported in this paper is compared (for both bearing sleeves tested simultaneously during a given test). The standard deviation of the COF (as error bars calculated using all 8600 data points) is shown as well, which enables an assessment of friction variability in the bearing during tests. The values shown in the figure are the average values of the bearing friction coefficient (considering the seal friction correction) for all start/stop cycles at the end of steady-state operation of the bearing with a speed of 1000rpm (fluid friction mode, approximately 12s for each cycle assuming that typical cycle consists of 2 seconds acceleration from standstill to the nominal steady state velocity that is maintained for 10 seconds, followed by a deceleration again to zero velocity in 3 seconds, Table 1). This choice was motivated by the relatively low frequency of the signal recording applied in this research, which did not allow for monitoring the evolution of the COF during transient states of bearing operation (start-up and shut-down). In addition, while both bearings operated

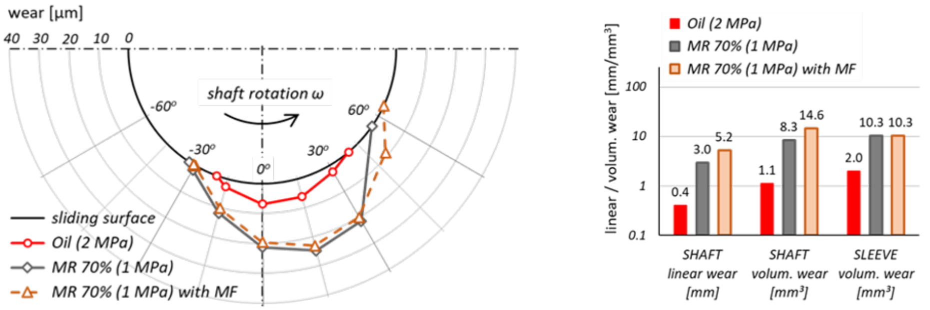

(a) (b)

Figure 4.8: Effect of the magnetic field (MF) on the wear of bearing components lubricated with MR fluid: a) distribution of the linear wear at the circumference of the sleeves, b) linear wear of the shaft journals and volumetric wear of the sleeves and shafts.

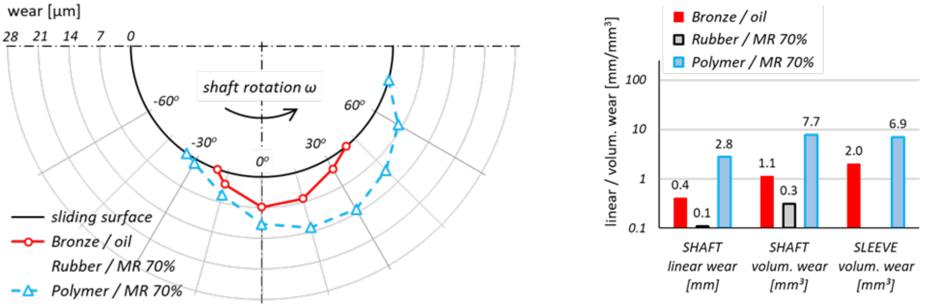

(a) (b)

Figure 4.9: Effect of the sleeve material on the wear of bearing components lubricated with MR fluid under the load of 2MPa: a) distribution of the linear wear at the circumference of the sleeves, b) linear wear of the shaft journals and volumetric wear of the sleeves and shafts.

with the same shaft, they had some impact on each other during the start and stop of the bearing system which was not the case during steady-state operation.

The results in figure 4.10 show that the smallest values of COF and their standard deviations were measured during the test with the oil as a lubricant at the load of 2MPa (reference case), while the highest friction was noticed for MR 70% and 2MPa. This last case also showed the largest difference in the average friction coefficients between the two tested bearings, as well as the largest standard deviations, meaning significant variability of the COF during tests. A much lower COF was measured under MR 70% lubrication when the load was reduced from 2 to 1MPa. However, it was still higher than for the reference case (over 2 times). It can be noticed that the COF measured for MR 70% was lower than for MR 20% (at the load of 1MPa) and that the activated magnetic field also increased the measured COF compared to the case without MF (for MR 70% and 1MPa). When compliant and soft materials (rubber and polymer) were applied for bearing sleeves, the measured friction coefficient was similar and equal to ~ 0.025. It was, however, still

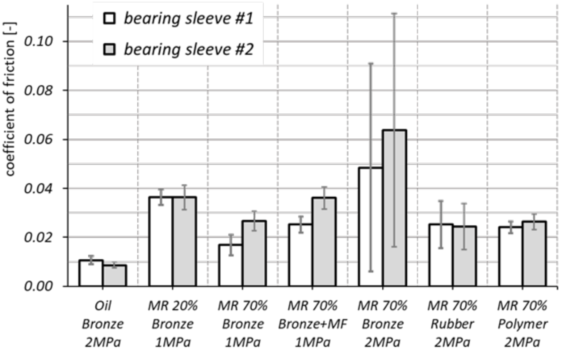

Figure 4.10: Comparison of the coefficient of friction for both bearing sleeves tested during a given wear test with standard deviation bars (calculated using 8600 data points).

higher than in the reference case (around 2.6 times).

Results of the bearing temperature during tests showed no significant changes for most of the cases. The measured temperature varied only slightly during the entire test, keeping a constant level around 35-45°C. The lowest temperature was measured in the polymer bearing; however, due to the low thermal conductivity of this material, it cannot be compared directly to the measurements for metallic bearings (bronze). On the other hand, high temperature variations were noticed for MR 70% bronze bearing tested under the load of 2MPa. In this case, the measured temperature course was "chaotic". It showed variations in a relatively large range (45-95°C), which was caused by periodic bearing operation with high friction (periods with the higher friction torque in the bearing correspond to higher bearing temperature).

4.4.6 Particle size analysis before and after start/stop tests

A particle size analysis was performed for samples of the MR fluids collected after the wear tests described in sections 4.4.1 - 4.4.4, and for samples of the unused MR 20% and MR 70% fluids. Micrographs of the particles from these samples were analysed with image processing software to determine the particle size distributions, but before these distributions are discussed, a qualitative comparison of the particle shapes and sizes will be performed using several representative micrographs. The effectiveness of the image analysis procedure for each of these groups will also be discussed.

Qualitative analysis

Figure 4.11 shows five of these micrographs, with each micrograph representing a group of particle samples with distinct properties. The first group contains the MR 20% samples, both before and after the wear test, and is represented by figure 4.11b which shows the particles from the used MR 20% fluid. As can be seen in the figure, the particles in this group are round and there are hardly any particle agglomerates. The image analysis procedure described in section 4.3.4 was found to work very well for this group.

The second group consists only of the samples collected after the wear tests with a bronze bearing loaded to 2MPa and lubricated with MR 70%, and is represented by figure

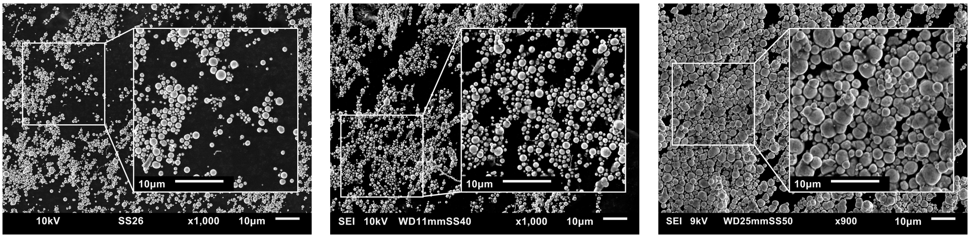

(a) MR 20% (unused)

(b) MR 20%, bronze, 1MPa

(c) MR 70% (unused)

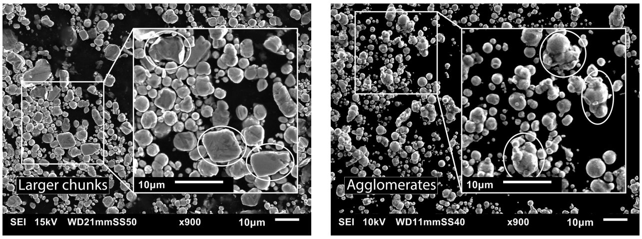

(d) MR 70%, bronze, 2MPa

(e) MR 70%, polymer, 2MPa

Figure 4.11: SEM micrographs of particles taken from several MR fluid samples. In subfigure (b) several larger chunks of iron are encircled, and in subfigure (c) the same is done for several particle agglomerates. Note that the micrographs in subfigures c), d), and e) were taken with an SEM magnification of 900x as indicated in the figures, but that these were zoomed in digitally to 1000x to match subfigures a) and b).

4.11d. As can be seen in figure 4.6, the wear of both the shaft and the bearing was very high during this wear test, and it is clear that the particles were also damaged. Compared to the first group, and to the particles from the unused MR 70% fluid shown in figure 4.11c, the particles from this group are generally less round and their surfaces are less smooth. Furthermore, several large non-round chunks of iron can be found between the particles (some have been encircled in figure 4.11d), these were probably created when individual particles were flattened or crushed together in the contact zone of the bearing. For this group the image analysis procedure works well too.

The final group includes all remaining MR 70% samples, and is represented by figure 4.11e, where the particles collected after one of the polymer bearing tests are shown. The micrograph shows that the individual particles are still mostly round, but that there are also a quite a few agglomerates consisting of multiple particles sticking together which were not present in the unused fluid from figure 4.11c (some of these have been encircled in the figure). In contrast to the heavily worn particles from figure 4.11d, these agglomerates still recognisably consist of individual particles. As a result, the particle analysis procedure was observed to frequently find the individual particles making up these agglomerates, instead of considering an agglomerate itself as one single particle. Whether or not the image analysis is successful seems to depend on the brightness and contrast of the agglomerate surface on the micrographs, specifically in those regions where the individual particles making up the agglomerates touch. It is therefore expected that the particle size distributions created for the fluid samples containing these types of agglomerates will underestimate the amount of relatively large particles, and will overestimate the number of small to medium particles.

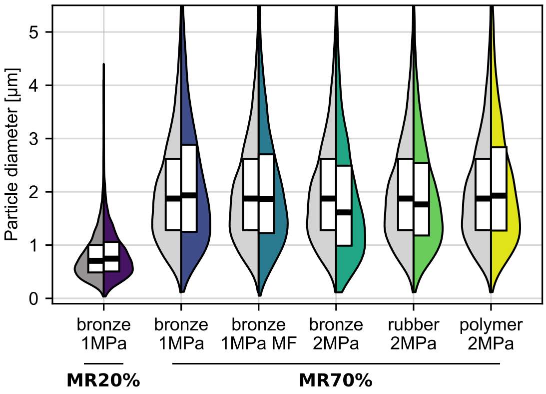

Figure 4.12: A violin plot of the particle size distributions both before and after the various wear tests. All violins have been calculated by combining the particle size data obtained from three different micrographs, all containing at least 1000 particles from the same MR fluid sample. The left (greyscale) side of every violin represents the unused MR fluid, the right (colored) side represents the MR fluid after the wear tests. The box plots inside the violins show the first and third quartiles, as well as the medians.

Particle size distributions

Figure 4.12 contains the particle size distributions for all MR fluid samples. As was mentioned in section 4.3.1, a different batch of (smaller) particles was used for the MR 20% fluid, explaining the stark difference in the distributions of the MR 20% and MR 70% fluids. There is also very little difference between the distributions before and after the MR 20% wear tests, which matches the qualitative analysis. Continuing to the MR 70% tests, it can be seen that the difference in the distributions before and after the wear tests is small for most of these samples as well. The largest difference can be observed for the bronze bearing lubricated with MR 70% and loaded to 2MPa, where the first quartile and median have both decreased by about 0.26µm after the wear test, and the third quartile has decreased by about 0.11µm. This corresponds with the qualitative analysis, where it was observed that this was the only wear test where the particles themselves seemed to have been damaged (see figure 4.11d).

Lowering the load to 1MPa prevents the particles from being worn down as much, with the first quartile and median changing no more than 0.1µm. The third quartile does increase by about 0.26µm, which could indicate an increase in the number of particle agglomerates that have been formed. Interestingly, this increase is not visible when the magnetic field is activated during the wear test. Finally, for the rubber bearing there is little difference in the size distributions before and after, with only a small decrease of all quartiles by less than 0.1µm after the test. In contrast, the polymer bearing shows a similar increase of the third quartile as was observed with the bronze bearing loaded to 1MPa (though the polymer bearing was loaded to 2MPa).

4.4.7 Surface analysis

SEM micrographs were made of the surfaces of the bearings and shafts used during the wear tests, to help explain the wear mechanisms occurring with MR lubrication. Figure 4.13 shows these micrographs for all bronze bearings, the micrographs of the corresponding shafts are only shown for the reference case (oil lubrication) and for the MR-lubricated cases with high shaft wear (MR 70% with 2MPa and MR 20% with 1MPa). All other shaft micrographs were qualitatively found to be indistinguishable from the reference case. Figure 4.14 shows micrographs of the surfaces of the softer rubber and polymer bearings that were tested. Of the shafts, only the micrograph of the shaft used with the rubber bearing is shown, the shaft used with the polymer bearing was lost in transit between two labs. Finally, the sliding direction was upwards in all micrographs, and the micrographs of the bearing surfaces were taken at the bottom of the bearing, in the contact zone, unless mentioned otherwise.

Bronze bearings

The unused and used bearing surfaces of the bronze bearing lubricated with oil are shown in figures 4.13a and 4.13b respectively. The unused surface contains many ridges in the vertical direction left by the original machining process, and while several ridges have worn down after the wear test, some of these marks are still visible on the right side of the micrograph of the worn surface. The condition of the worn shaft surface looks similar to that of the bearing surface, though some plastic deformation of the ridges can also be seen (figure 4.13c).

With MR lubrication, the appearance of the surfaces changed dramatically after the wear tests. Figures 4.13h and 4.13d show the bearing micrographs for loads of 1 and 2MPa respectively, and at first glance their overall appearance is similar. For both loads the original machining marks have disappeared completely, almost certainly due to large amounts of third body abrasive wear caused by the particles. Furthermore, several features are visible that indicate that some adhesive wear may have occurred. Next to that, figures 4.13e and 4.13f, which represent EDS maps of the iron and copper content, show large patches of (pure) iron on the surface of the bearing loaded to 2MPa, while no iron could be found on the surface of the bearing loaded to 1MPa. Finally, the shaft used with the bearing loaded to 2MPa is shown in figure 4.13g. Its surface looks very similar to that of the oil-lubricated shaft (figure 4.13c), but there seems to be some cracks running in the sliding direction.

In the next wear test, magnets were added to the MR lubricated system loaded to 1MPa, resulting in the micrograph in figure 4.13i which was taken at a location on the surface directly above one of the magnets. The overall appearance of the surface is the same as it was without the magnets present, apart from a large number of small scratches.

Finally, figures 4.13j and 4.13l show the effect of a reduced particle concentration (20% by volume) on the surfaces of the bearing and shaft respectively. The contrast with the other micrographs for the bearings lubricated with MR 70% is large, with both the bearing and shaft surfaces containing some cracks, and the shaft surface showing many ridges in the sliding direction. When zooming in on the bearing surface (figure 4.13k) it can be seen that this surface is heavily scratched and contains many embedded particles. Furthermore, many pits can be found in the surface, some of which are almost perfectly round, indicating that a number of embedded particles may have been dislodged during the wear test.

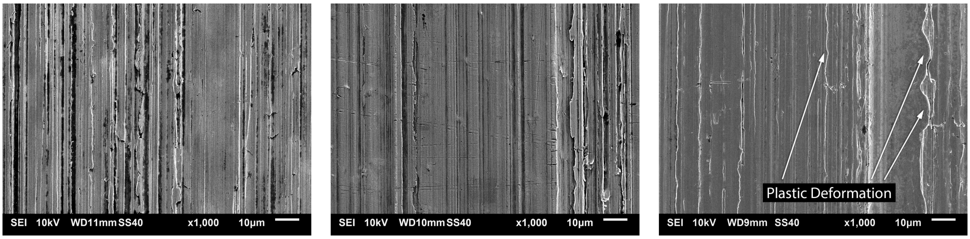

(a) Bronze (unused) (b) Oil, 2MPa (c) Oil, 2MPa (shaft)

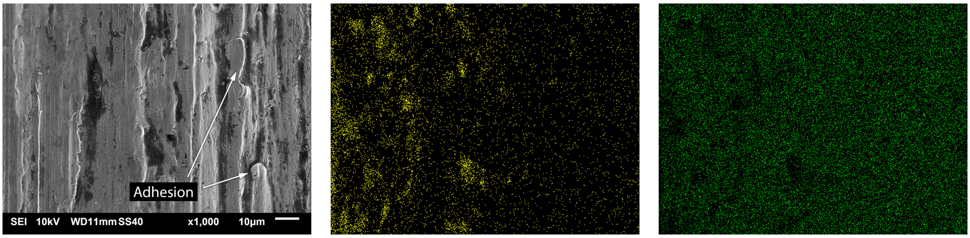

(d) MR 70%, 2MPa (e) MR 70%, 2MPa, Fe-content (f) MR 70%, 2MPa, Cu-content

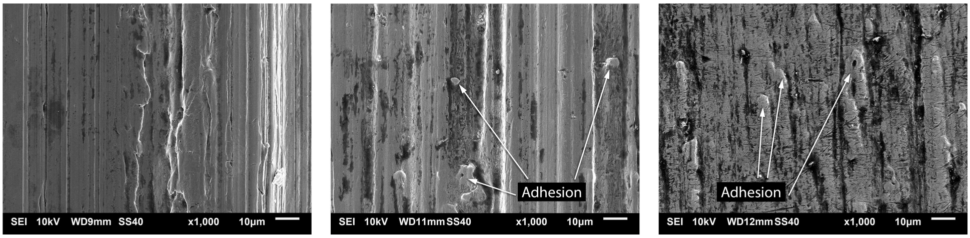

(g) MR 70%, 2MPa (shaft) (h) MR 70%, 1MPa (i) MR 70%, 1MPa, with MF

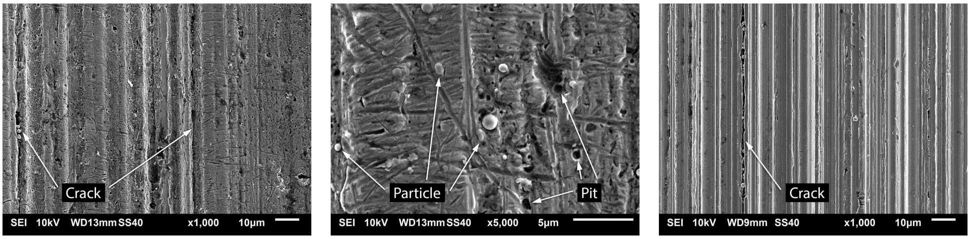

(j) MR 20%, 1MPa (k) MR 20%, 1MPa, zoomed in (l) MR 20%, 1MPa (shaft)

Figure 4.13: SEM micrographs and EDS maps of several bronze bearing surfaces for various operating conditions, as well as some representative steel shaft surfaces. The sliding direction was upwards in all cases.

Similar to the MR 70% test with a load of 1MPa, no iron could be found in the bearing surface itself (apart from the embedded particles).

Rubber and polymer bearings

Starting with the rubber bearing, figures 4.14a and 4.14b show the surface before and after the wear test respectively. While it was not possible to determine the volumetric wear of the rubber bearing, the micrographs do indicate that the appearance of the surface has at least changed drastically. The original machining marks (horizontal ridges that were left by the molds) have worn away completely, and the surface instead contains vertical grooves, as well as some pits. Particles are visible in some of these pits, and individual particles have been embedded in the rubber as well in some other locations.

In contrast, the surface of the corresponding shaft shown in figure 4.14c does not show major signs of wear, and looks similar to the lightly worn shaft used in the oil-lubricated bronze bearing (see figure 4.13c). Only some fine scratches are visible, which are probably caused by particles embedded in the rubber. These results agrees with the linear wear tests, which showed minimal wear of the shaft (see figure 4.9).

The remaining figures all show micrographs and EDS maps for the polymer bearing surface (unfortunately the shaft used for the polymer bearing test was lost during shipping between the participating research groups). This was the only bearing where a clear difference could be observed in the appearance of the surface in the converging region of the film, compared to the surface close to minimum film, which is why micrographs were made of both regions of the bearing.

Starting with figure 4.14d, the unused polymer surface shows very obvious machining marks, with clear vertical ridges about 100μm apart, and smaller, regularly spaced horizontal grooves in between. This texture is still visible on some parts of the worn surface in the converging region of the film, as can be seen in figure 4.14e, but large clumps of iron have also been smeared onto the surface, forming an almost continuous layer of iron on top of the polymer. This becomes even more obvious when zooming in (see figure 4.14g) and comparing the micrograph with the EDS maps for iron and carbon (figures 4.14h and 4.14i respectively) respectively, with carbon being the main element of the polymer). The diverging half of the bearing has a very different surface, as can be seen in figure 4.14f. The mostly continuous layer of iron from the converging region tapers off into smaller branches in this region. Furthermore, the original machining marks have been worn away completely and there are obvious grooves and ridges in the sliding direction. When zooming in on one of the areas without a layer of iron (see figure 4.14j) and comparing the micrograph with the EDS maps for iron and carbon (figures 4.14k and 4.14l respectively), it becomes clear that there is still a large amount of iron on the polymer bearing surface, mostly in the form of smaller clumps and individual particles embedded in the surface.

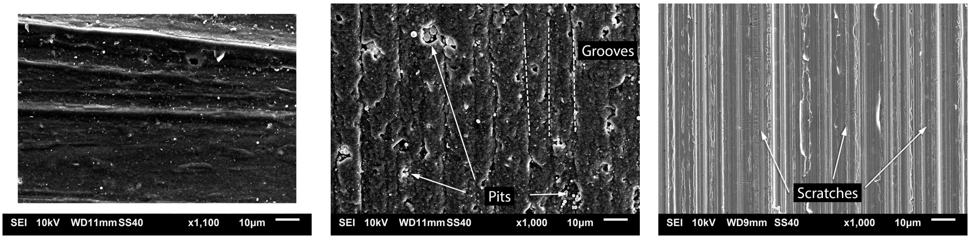

(a) Rubber (unused) (b) MR 70%, 2MPa, rubber (c) MR 70%, 2MPa, rubber (shaft)

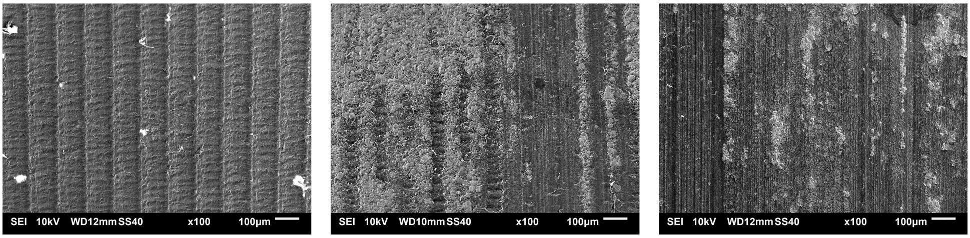

(d) Polymer (unused) (e) MR 70%, 2MPa, polymer, converging region (f) MR 70%, 2MPa, polymer, diverging region

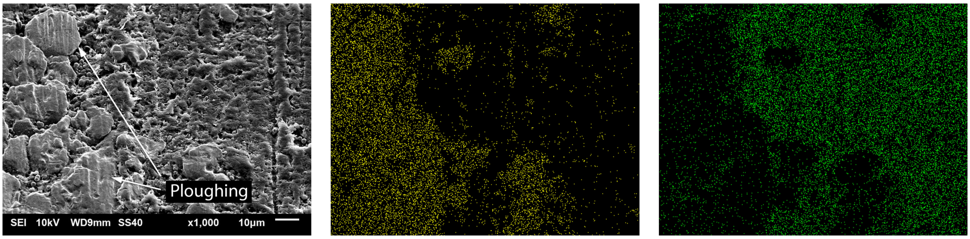

(g) MR 70%, 2MPa, polymer, converging region, zoomed in (h) MR 70%, 2MPa, polymer, converging region, Fe-content (i) MR 70%, 2MPa, polymer, converging region, C-content

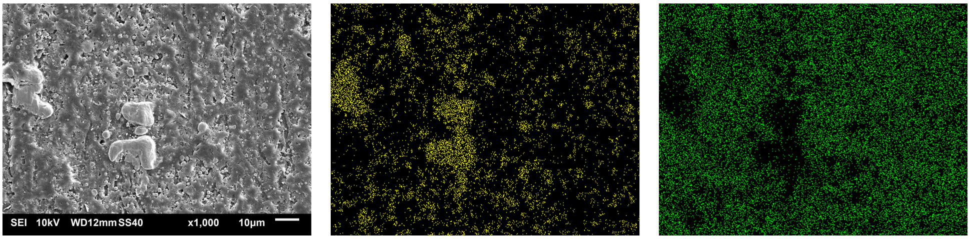

(j) MR 70%, 2MPa, polymer, diverging region, zoomed in (k) MR 70%, 2MPa, polymer, diverging region, Fe-content (l) MR 70%, 2MPa, polymer, diverging region, C-content

Figure 4.14: SEM micrographs and EDS maps of the rubber bearing surfaces (subfigures a) through c)) and polymer bearing surfaces (subfigures d) through l)). The sliding direction was upwards in all cases. Note that the micrograph in subfigure a) was taken with an SEM magnification of 1100x as indicated in the subfigure, this micrograph was zoomed out digitally to 1000x to match the other subfigures.

4.5 Discussion

The comprehensive research program allowed us to investigate different aspects of the tribological properties of the system lubricated with the MR fluid and compare the obtained results to those of an oil-lubricated bearing tested under the same conditions. This section discusses the results presented in the previous sections of the paper.

The oil-lubricated bearing sleeves and shaft journals (reference case) showed low friction coefficients and relatively small amounts of wear under the load of 2MPa (figure 4.6), which agrees with the very minor differences in the surface micrographs before and after the wear tests (figures 4.13a through 4.13c). In contrast, the wear of the mating components was found to be higher (sometimes much higher) in most of the tested bearing configurations lubricated with MR fluid. The bronze bearing lubricated with MR 70% under a load of 2MPa showed the highest wear, which was found to be two orders of magnitude higher (!) than in the reference case. The friction coefficient was also found to be 5.5 to 6 times larger for steady-state operation (figure 4.10), which could indicate permanent mixed or boundary lubrication, especially since the standard deviation on the friction measurements was high as well for these tests. As was to be expected, these extreme levels of wear and friction could be reduced by lowering the load to 1MPa, but even then, they were still several times higher than for oil-lubricated bearings. For both loads the large amounts of wear are probably the result of third body abrasion, however, looking at the micrographs of the mating surfaces (figures 4.13d through 4.13h) also reveals some differences in the wear mechanisms for these two load cases. As was observed in the results section, the bronze sleeve surface of the bearing loaded to 2MPa contained patches of pure iron, while this was not the case for the lower load. The only two components in the bearing system containing any iron were the particles (pure iron) and the shaft journal (AISI 1045 carbon steel). Since the EDS did not detect any elements in these patches other than iron (such as manganese, which appears in AISI 1045), these patches can only consist of (the remains of) particles. It seems likely that with the higher load of 2MPa, particles were flattened or crushed into the bearing surface and were then worn down together with the bronze, since the areas on the EDS map that contain iron do not match up with the ridges visible on the micrograph (figures 4.13e and 4.13d respectively). Since no patches of iron were found with a load of 1MPa, it seems likely that this load was too low to cause such a deformation of the particles. This difference was also revealed by the particle size analysis in section 4.4.6, where it was found that only the particles from the bearing loaded to 2MPa were visibly worn (figure 4.11) and had decreased in size after the wear test, while the particles from the bearing loaded to 1MPa had roughly the same size before and after (figure 4.12).

The effect of the magnetic field was much smaller than that of bearing load. The friction increase compared to the reference went up from 2.3 times without magnetic field to 3.2 times with magnetic field (figure 4.10), which was caused by the magnetically induced viscosity increase. With the activation of the magnetic field the wear of the shaft journals was also slightly higher than without a magnetic field, but the wear of the bearing sleeves did not change (figure 4.8). This could be caused by the formation of particles chains at the locations of the magnets that are embedded below the stationary bearing sleeve surface. These chains will mostly stay in position over the magnets [5], likely causing their ends to be dragged along the surface of the rotating shaft journal. The existence of such a wear mechanism is supported by the fact that only the shaft wear changed with the activation of the magnetic field, the level of wear of the bearing sleeves remained the same. The sleeve surface micrographs did show a large number of scratches though (figure 4.13i), these may have appeared during the transitions to boundary lubrication, with the magnetic field pinning the particles near the magnets in the contact zone in place, preventing them from moving along with the rotating shaft. Such an effect could also be the cause of the reduction of the number of agglomerates consisting of multiple particles compared to the unactivated bearing (figure 4.12).

In contrast to initial expectations based on literature about lubrication experiments with contaminated water [122, 123], a reduction in the particle concentration from 70% to 20% did not lead to lower wear, but actually increased wear. The amount of wear noticed for the bearing sleeves was only slightly higher (around 60%, see figure 4.7), but the shaft journal wear increased by a significant amount (an order of magnitude) with MR 20% lubrication compared to wear results for the standard MR fluid (MR 70%, 1MPa). Compared to that bearing the friction coefficient also increased slightly. An explanation for these wear results might be found by examining the surface micrographs (figures 4.13j and 4.13l). As was mentioned in the results section, the shaft journal surface was heavily grooved in the sliding direction, while the bearing sleeve surface contained many embedded particles. However, unlike the 2MPa MR 70% test there were no patches of iron in the sleeve surface meaning that the particles were not crushed or flattened into the surface like they were at that higher load. Similarly, the particle size analysis indicated barely any change in both the size and shape of the particles in the MR 20% fluid before and after the wear tests (figure 4.12). Taken all together, it seems likely that the qualitative information from the manufacturer (section 4.3.1) was correct, and the hardness of the particles in the MR 20% fluid was indeed higher than of those in the MR 70% fluid. The exact difference in hardness between the MR 20% and MR 70% particles is not known, and it was found to be difficult to measure the hardness due to the extremely small size of the particles. Do note that there could also be an alternative explanation for the difference in particle hardness between the two MR fluids. Work hardening of particles has been observed in literature [54, 55], and it is possible that the lower concentration of 20% led to higher stresses on the individual particles. However, since the deformation of the particles seems to have been minimal, it is deemed more likely that the particles in MR 20% did indeed have a higher hardness to begin with, but this could be investigated further.

The results for the tests with the bearings made of compliant materials show very different results compared to the bronze bearing. Both polymer and rubber bearings show a comparatively modest increase in friction coefficient by about 2.6 times (figure 4.10). At the same time, the polymer bearing has the lowest bearing sleeve wear level out of all bearings lubricated with MR fluid, and was relatively close to the reference case for both bearing and journal wear (figure 4.9). The wear level on the shaft journal used with the rubber bearing was the lowest of all bearings that were tested, lower even than in the reference case. However, since the sleeve wear could not be measured for the rubber bearing, it is difficult to say anything about its overall wear performance. Looking at the rubber surface micrographs also shows large changes in the surface geometry before and after the wear tests (figures 4.14a and 4.14b respectively). The wear to the rubber sleeve surface was at least large enough to completely remove the original machining marks, and to create several grooves and pits that contain particles. These findings match with literature for rubber bearings lubricated with oil or water containing hard particles [122, 124, 125]. It has been stated that once the oil film becomes thin enough (due to lowered speed or increased load), individual particles with diameters larger than the film thickness will bridge the gap between the mating surfaces. Due to the elasticity of the rubber, the particles will locally deform this surface and will start to roll on the harder shaft surface, minimizing the wear to both components. However, once the system reaches boundary lubrication, the particles will be pressed almost fully into the rubber, which can lead to ploughing of the rubber surface and the formation of furrows or grooves in the sliding direction, similar to those observed in the micrograph. At the same time, local stress concentrations due to the particles deforming the rubber can cause the stress to exceed the strength limit, causing particles to be embedded in the rubber, and leading to the formation of pits [125]. These pits can be identified by the particles that have been collected in them and can be found on the micrographs of the rubber bearing sleeve.

The micrographs for the polymer bearing show that the wear mechanisms for that system differed significantly from those with the rubber bearing (figures 4.14d through 4.14f). The polymer bearing sleeve was the only sleeve with a difference in the appearance of the converging and diverging areas of the bearing, with the converging area showing a layer of iron clumps on top of the polymer surface, while the diverging area showed more wear and showed embedded individual particles and smaller clumps. During operation of the bearing, the particles were probably crushed in the converging region of the film, leading to iron clumps that are tens of micrometers wide, much larger than the particles from the fluid which had a median size of 1.9µm after the wear test (see figure 4.12). Similar to the bronze bearing tested at 2MPa with MR 70%, the iron on the bearing surface has been worn during the test, as evidenced by the clear ploughing marks in the sliding direction that are visible on most of the clumps in figure 4.14g. An obvious difference with the bronze bearing sleeve is that the iron on the polymer surface has formed clearly distinguishable clumps lying on top of the polymer, and has not been smeared out over the sleeve surface (figure 4.13d). This may be the result of the lower stiffness and hardness of the polymer bearing, which can deform elastically under load, possibly preventing the particles from being flattened entirely. It could also explain why the average size of the particles in the fluid increased slightly, instead of decreasing like with the bronze bearing sleeve. Furthermore, the resulting layer of iron seems to have partially protected the underlying polymer surface, since the machining marks are still visible through gaps in the iron layer while they have been worn away in the areas without any iron clumps at all. This seems to be a similar effect to what was observed by Leung et al [54], who found a protective layer of flattened particles on the block of a block-on-ring tribotester lubricated with an MR fluid. They also found that the protective layer did not extend into the diverging region, which is the case for the bearing in this paper as well and would explain the larger degree of visible wear in the micrographs of that region. The individual clumps or iron found in the diverging region are likely debris from the iron layer in the converging region.

4.6 Conclusion

In this research, the wear properties of an MR-lubricated hydrodynamic journal bearing system have been investigated experimentally with start / stop wear tests under varying operating conditions. These results have been compared with a reference, an oil-lubricated bearing with a bronze sleeve, with the aim of finding a bearing sleeve material with a similar level of wear for MR lubrication as that of the reference for oil lubrication. The key conclusions of this investigation are:

1. The wear performance of a standard combination of a bronze bearing sleeve and steel shaft journal is extremely poor for all operating conditions, with an increase in wear of two orders of magnitude compared to the reference, as well as 5 to 6 times increase in friction. The wear increase is likely the result of third body abrasion due to the presence of iron microparticles in the MR fluid (which were also damaged), and could only be reduced by lowering the load applied to the system.

2. Lowering the particle concentration of the MR fluid from 70% to 20% did not yield the expected wear reduction but actually increased the wear. The exact reason for this is not known but may be related to an unintended difference in particle size and hardness between the particles in the two MR fluids.

3. Using a rubber bearing sleeve resulted in minimal wear to the shaft journal, reducing it below even the level of wear of the reference, as well as a doubling of the friction coefficient. However, due to the softness of the rubber compound it was not possible to measure the sleeve wear with the profilometer, and the SEM micrographs did reveal some visible damage to the rubber surface. Due to the low level of shaft journal wear it is recommended to further investigate the wear performance of rubber bearing sleeves for MR lubrication.

4. The lowest level of bearing sleeve wear for MR lubrication was obtained with a polymer sleeve, the wear of this sleeve was only about 4 times larger than with the reference, while the friction was doubled. It was found that a layer of crushed iron particles had formed in the converging region of the bearing, possibly protecting the underlying polymer. For these reasons, polymer seems like a promising sleeve material for an MR-lubricated bearing operating in low-speed conditions. This has since been reconfirmed by another investigation, where the authors experimentally tested the hydrodynamic performance of an MR-lubricated polymer bearing for a wide range of speeds [126].

5

The MR-lubricated bearing

In chapter 2, an initial exploration showed that MR-lubrication of a hydrodynamic journal bearing does not necessarily have to result in high friction, which was previously the only result reported in literature. Simultaneously it was found that the shear-thinning MR fluid was not easily modelled using a Newtonian approximation, leading to the development of a computationally efficient shear-thinning model in chapter 3. Furthermore, wear was found to be unacceptable at higher loads, leading to the discovery of an alternative polymer bearing sleeve with more acceptable wear characteristics in chapter 4. This chapter combines the lessons of these previous investigations, leading to a comprehensive research project focused on testing the performance of an MR-lubricated journal bearing for a range of loads and magnetic fields. The aim was to find out to which degree the performance of the bearing could be modified by changing the magnetic field when lubricating with MR fluid.

This chapter previously appeared as *G. van der Meer and R. van Ostayen, 'Investigating Film Thickness and Friction of an MR-Lubricated Journal Bearing', Lubricants, vol. 13, no. 4, Art. no. 4, Apr. 2025..*

Please note that the addendum at the end of this chapter was not part of the original publication, it discusses possible ways in which the standard Hersey number could be modified to be used for variable viscosity fluids. This is done with examples based on the experimental results presented in this chapter.

Abstract

Magnetorheological (MR) fluids are frequently reported to have potential as lubricants for hydrodynamic bearings operating at high loads, but no comprehensive effort has been made to investigate their performance under a variety of operating conditions. This paper therefore presents an extensive experimental and numerical investigation of a MR-lubricated hydrodynamic journal bearing subjected to different loads and magnetic fields, and compares these results to those of an oil-lubricated bearing. It is shown that by increasing the magnetic field strength, the performance characteristics of the bearing can be changed from low hydrodynamic friction and a high transition speed, to high hydrodynamic friction and a low transition speed. Furthermore, it has been found that the way in which these characteristics scale with increasing load differs for the MR- and oil-lubricated bearings. With MR lubrication, the relative change in characteristics with the application of a magnetic field is smaller at higher loads, due to the strong shear-thinning rheology of MR fluids. To include these effects in the model, a basic relation for the apparent MR viscosity as a function of shear rate, temperature and magnetic field strength is introduced. Finally, the bearing was made from a polymer to improve wear resistance under MR lubrication, but a comparison with a Reynolds equation–based numerical model indicates possible performance degradation due to shape errors, which is a known issue with this bearing material.

5.1 Introduction

A hydrodynamic journal bearing is defined by its lubricating film, which separates the two surfaces and thereby minimises friction and prevents wear. The thickness of this film depends on various factors like the geometry, the speed of the shaft, and the properties of the lubricant that is being used. A very important lubricant property is the viscosity, with higher viscosity leading to thicker films but also to higher friction, and vice versa. Viscosity is an inherent property of a standard lubricating oil, but with 'smart' lubricants like magnetorheological (MR) fluids, it is possible to actively control the apparent viscosity with the application of an external magnetic field.

An MR fluid consists of a base oil with a large number of iron microparticles in suspension (generally around 20 vol%). In general, the MR fluid responds like a standard (albeit strongly shear-thinning) lubricant, but with the application of a magnetic field the particles in the fluid will magnetise, and will form chain-like structures along the magnetic field lines. These structures impede the flow of the base oil, manifesting as an increase in the effective viscosity on the macro scale. The magnetic field also enhances the shear-thinning characteristics, with higher stresses leading to breakage of the structures and therefore to progressively smaller viscosity increases. In contrast, lower stresses will strengthen the particle structures, eventually preventing the flow of base oil completely and turning the fluid into something resembling a viscoplastic solid. Finally, all of these magnetically induced effects are fully reversible, removing the magnetic field will result in the original suspension in only a few milliseconds [5, 6].

In the past, the controllable viscosity of MR fluids has been used mainly to construct active dampers and brakes, but other applications have also been investigated, such as actuators, haptic devices, and magnetic metamaterials [19, 127–129]. In addition, some research has been done on the use of MR fluids as lubricant in hydrodynamic (journal) bearings. Due to the complicated non-Newtonian characteristics of MR fluids, a relatively large number of researchers have focused on modelling these bearings numerically. A number of viscosity models have been identified that can describe these non-Newtonian characteristics with reasonable accuracy, most notably the Bingham plastic and Herschel-Bulkley models [11]. These viscosity models can then be combined with either the Navier-Stokes equations for a full 3D CFD model [39], or with a variant of the Reynolds equation for a simpler 2D or even 1D model [40, 66]. Several general journal bearing case studies have been created where these types of models were used to investigate the effects of MR lubrication [21, 22, 130]. More focused studies can be found as well, for example ones investigating dynamic behaviour [29, 131] or the influence of surface textures [23], surface roughness [132], or temperature [133]. In general it was observed that an increase in lubricant viscosity due a stronger magnetic field would lead to thicker films (or equivalently, a reduction in the transition speed) but also to higher friction.

Several experimental investigations into MR lubrication in bearings have also been carried out, but these are more rare. In one of the earliest experimental papers, an MR-lubricated hydrostatic bearing was successfully designed to achieve a constant film thickness independent of load by varying the magnetic field strength [26, 45]. Several experiments with journal bearing setups were then performed, confirming the general findings of numerical research that stronger fields lead to both thicker films and higher friction [20, 27–29]. Some of these researchers suggested that active control of the magnetic fields using electromagnets could be a way of achieving both thick films at low speeds, and low friction at high speeds, by reducing the strength of the magnetic field at higher speeds [27]. Similarly, the use of local magnetic fields has been proposed as a way of minimising the friction increase by only magnetising the film where an increase in viscosity has the largest effect on film thickness (near minimum film), instead of magnetising the entire film [46, 134]. Two investigations have looked into this concept and have compared the performance of MR fluid with that of standard (Newtonian) lubricating oils. The first used a very strong local magnetic field with a standard MR fluid, and found that the resulting film thickness and friction were both still higher than with the standard lubricating oil [30]. On the other hand, the second used a weaker magnetic field and a fluid with fewer particles (reducing the magnitude of the viscosity increase), and found the MR lubricated bearing to have lower friction than the oil lubricated bearing, but also a higher transition speed (equivalent to a lower film thickness) [105]. Both suggested that the fluid and magnetic field should be optimised further.

In summary, the use of MR fluid as a lubricant for hydrodynamic (journal) bearings has gotten some (mostly numerical) attention in literature. Generally it is found that the increase in viscosity due to the magnetic field will not only increase the film thickness, and thus reduce the transition speed, but will also result in higher friction compared to standard lubricants. However, while some suggestions have been made for possible ways to improve these bearings and obtain performance superior to that of an oil lubricated bearing, there has not yet been a comprehensive effort to find out under which operating conditions this would actually be possible, if at all. This work therefore presents an extensive experimental and numerical investigation into the performance of an MR-lubricated journal bearing under different loads and with different magnetic fields, and compares this to the same bearing lubricated with a standard oil.

5.2 Method

In this paper, experiments have been performed with a custom hydrodynamic journal bearing setup, lubricated either with a reference oil or a magnetorheological (MR) fluid. These results have been compared with those of a numerical model. This section will first introduce the experimental setup and experimental procedures, and will then discuss the model.

5.2.1 Experimental setup

The custom-built experimental journal bearing setup that was used for this research is shown in figure 5.1. This setup was previously used for the research presented in [105], the main changes compared to that work are the difference in bearing material and MR fluid, and the larger variety of tests that have been performed. The operating conditions for those tests can be found in table 5.1, which also shows the properties of the main bearing. The setup consists of a main shaft supported by two self-aligning ball bearings, with the bearing housing placed in between. Since this housing is hollow, the actual bearing bush is only supported at the edges, leaving open space inside the housing all around the circumference of the bush, as is shown schematically in figure 5.2. This open space is used to place neodymium permanent magnets to activate the MR fluid in the thin film. To pre-

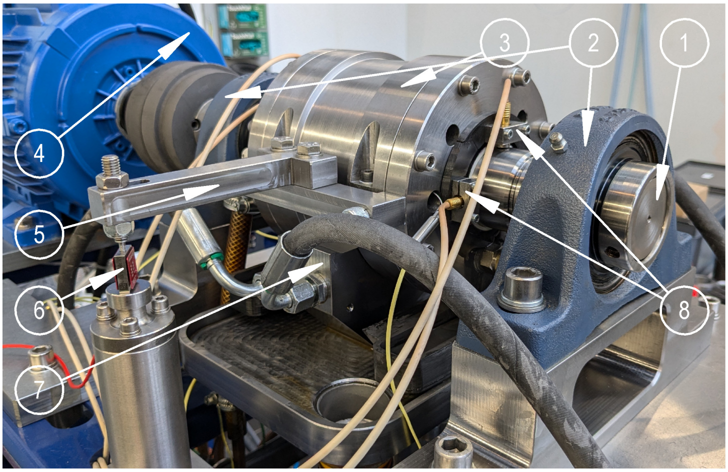

Figure 5.1: A picture of the experimental setup. 1 – main shaft, 2 – support bearings, 3 – bearing housing, 4 – motor, 5 – moment arm, 6 – load cell for friction torque measurement, 7 – hydrostatic bearing, 8 – capacitive sensors (the two capacitive sensors on the other side of the housing are not visible).

Table 5.1: Overview of the bearing properties and operating conditions. This data previously appeared in another article by the authors where this setup was used as well [105], the reader is referred to that paper for a more extensive description of the setup, as well as a derivation of the sensor accuracies. The properties of the polymer used for the bearing were obtained from the manufacturer.

Property	Symbol	Value
Bearing length / shaft diameter /	L/D	100mm/50mm
Nominal radial clearance	h_0	155µm
Shaft / bearing material		C45 steel/Polymer
Shaft / bearing surface roughness	Ra	0.4µm/0.4µm
Max. load / specific pressure	W_a/p_m	7.5kN/1.5MPa
Speed range	n	0 - 1000/1500rpm
Lubrication groove radius / length		1mm/100mm
Lubricant flow rate	Q_{in}	$0.3\,\mathrm{L\,min^{-1}}$
Average inlet temperature		32°C
Average film temperature	T	36°C
Polymer Youngs modulus		2.2GPa
Polymer hardness (shore-D)		83
Polymer thermal expansion coefficient		6×10^{-5}mm/(mm°C)
Applied load accuracy		±30N
Distance sensor accuracy		±0.15µm
Friction coefficient accuracy		±3.12N/W_a
Thermocouple accuracy		±1.5K
Centre-to-centre distance magnets	L1	20.8mm
Distance magnet-film	L2	9mm
Magnet diameter / length	d_m/L3	20mm/5,10,20mm
Magnet remanence	B_r	1.29-1.32T

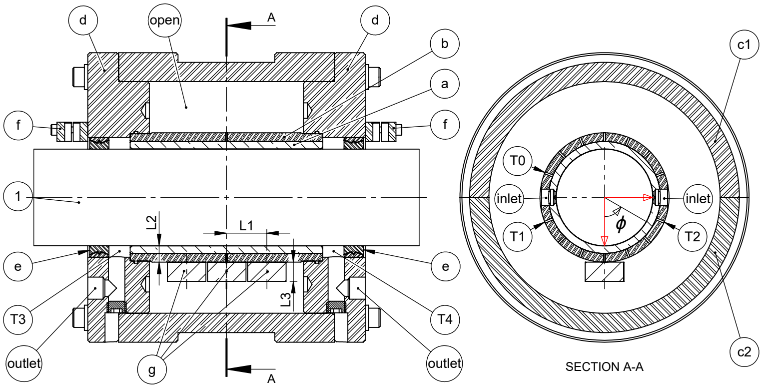

Figure 5.2: A section view of the bearing housing (component 3 in figure 5.1). 1 – shaft (component 1 in figure 5.1), a – polymer inner bush, b – non-magnetic steel outer bush, c1/c2/d – housing components, e – non-magnetic contactless labyrinth seals, f – capacitive sensor clamps (component 8 in figure 5.1), g – magnets, T0-T4 – thermocouples (T3 and T4 were not present for all measurements). The lubricant inlets and outlets are marked as well. In the figure on the right, ϕ is defined as the angular coordinate inside the bearing. The shaft rotates in the positive ϕ direction, and as an example of a possible position of the magnets, the magnets are shown at $\phi = 0°$.

vent deformation of the bush due to the film pressures, the 4mm thick polymer inner bush (chosen for its wear resistance when lubricated with MR fluid [135]) is press-fitted inside a 5mm thick steel bush.

A constant load is applied to the bearing housing with a pneumatic actuator. The friction torque in the bearing is measured with a load cell that is loaded via a moment arm connected to the bearing housing. Accurate torque measurements are obtained since the rotation of the housing around the shaft is only constrained by the load cell: a hydrostatic bearing is used to transfer the load from the actuator to the housing, and the bearing is sealed with contactless labyrinth-type seals (components marked 'e' in figure 5.2). Lubricant is provided to the bearing at a constant flow rate of $0.3\,\mathrm{L\,min^{-1}}$ using a positive displacement cavity pump that draws from a 1L reservoir. Thermocouples measure the temperature of the outer steel bush and the lubricant temperature in the inlets, later on some tests were repeated with thermocouples T3 and T4 present in the outlets to verify the bush temperatures. Finally, two capacitive distance sensors are mounted 90° apart on both sides of the housing. These sensors point at the shaft surface and are used to calculate the locus on both sides of the bearing, an overall locus is obtained by averaging the results from the two sides.

5.2.2 Experimental procedure

The experimental setup has been used to measure Stribeck curves of the tested lubricants by changing the speed of the shaft, while keeping the load and magnetic field constant. Every Stribeck measurement was started with a warm-up phase, consisting of the system running at maximum shaft speed (either 1000 or 1500rpm depending on the test) while subjected to the target load and magnetic field. This process was continued until the lubricant temperature at the outlets reached 32°C, which could take up to an hour depending on the ambient conditions in the room.

After the warm-up phase, the Stribeck measurement was started. These measurements were conducted by reducing the speed in discreet steps, and by letting the system stabilise for 3 minutes after every change in speed. Steps of 100, 50, and 25rpm were taken between respectively 1500/1000rpm-500rpm, 500rpm-300rpm, and 300rpm-0rpm. A Stribeck measurement was considered to be finished once the friction coefficient started increasing sharply after a reduction in speed, or once the friction coefficient became larger than 0.02. Either one of these events was considered to be an indication of a transition to mixed or boundary lubrication. At that point the shaft would be stopped (to prevent damage to the bearing by running under boundary lubrication unnecessarily), and as a final step the clearance circles, used to calibrate the locus measurements, would be measured with a method that was established previously [50, 105]. For any follow-up tests on the same day, the system would first be allowed to cool down sufficiently before starting the warm-up process of the next measurement. All tests presented in this paper were repeated three times, the reported values are the averaged values.

5.2.3 Lubricant properties

Two different lubricants were tested for this paper. A standard SAE 30 mineral oil, Castrol MHP 153, was used to obtain a reference measurement, while the MR measurements were performed with the MR fluid MRHCCS4-A containing 70% particles by weight [119]. From this point on these lubricants will be referred to as 'Oil' and 'MR 70%' (or simply 'MR') respectively. An Anton Paar MRC 302 rheometer [136] with a cone-on-plate geometry was used to measure the viscosity of the two lubricants as a function of temperature, shear rate, and magnetic field strength (only for the MR fluid), the results are shown in figure 5.3. The shear-thinning properties of the MR fluid are visible in figure 5.3b, and all figures (figure 5.3c in particular) show the increase in viscosity with increasing magnetic field strength. It can also be seen that the effect of very strong magnetic fields is relatively minor due to the effects of magnetic saturation of the particles. Finally, figure 5.3a shows that similar to oil, the MR fluid viscosity decreases with temperature, but interestingly this decrease is stronger when no magnetic field is applied. The reduced influence of temperature on the viscosity when a magnetic field is present is the result of the influence of the particle structures, which are not influenced by temperature (below the Curie temperature) [48, 127, 137]. This means that the relative increase in viscosity due to the application of a magnetic field actually goes up when the temperature increases.

To be able to use this viscosity data in the numerical model (described in section 5.2.4), a viscosity model can be fitted to the data. The Bingham plastic and Herschel-Bulkley models are frequently used for this purpose, both of these models use a yield stress to represent the very large increase in viscosity (almost a solidification) at shear stresses near zero. More important is that the Herschel-Bulkley model also incorporates shear-thinning, which is generally considered to make it more accurate for use in high shear rate applications (such as journal bearings) [6, 11]. The Herschel-Bulkley model is represented by equation 5.1, where $|\vec{\tau}|$ and $|\vec{\dot{\gamma}}|$ are the shear stress and shear rate magnitudes respectively, K is a proportionality constant called the consistency index, τ_y is the yield stress, and m is the flow index that determines whether the fluid is shear-thinning ($m < 1$)

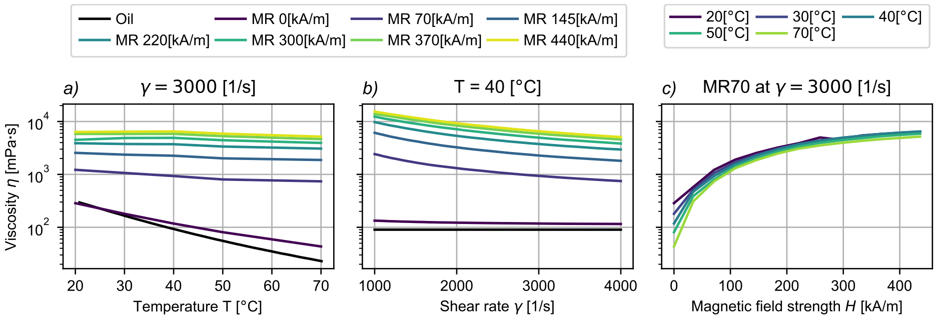

Figure 5.3: Viscosity measurements for the reference oil and MR fluid used to perform the experimental investigation. a) Viscosity as a function of temperature for a constant shear rate. b) Viscosity as a function of shear rate for a constant temperature. c) Viscosity as a function of magnetic field strength for a constant temperature and shear rate.

or shear-thickening ($m > 1$).

$$|\vec{\tau}| = \tau_y + K|\vec{\dot{\gamma}}|^m \tag{5.1}$$

This equation can be rewritten to the form $|\vec{\tau}| = \eta|\vec{\dot{\gamma}}|$, and isolating the apparent viscosity η then results in equation 5.2 that can be fitted to the rheometer data. For this equation it is assumed that the shear stress in the fluid is larger than the yield stress.

$$\eta = \frac{\tau_y + K|\vec{\dot{\gamma}}|^m}{|\vec{\dot{\gamma}}|} \tag{5.2}$$

However, in its current form, the Herschel-Bulkley model does not yet include the effects of variations in magnetic field strength H or temperature T. Starting with the former, only limited literature could be found about magnetic field strength–dependent MR Herschel-Bulkley fits (or Bingham fits). One paper describes the use of an asymmetrical sigmoidal ('S'-shaped) function to model the relation between yield stress and magnetic field strength, while keeping the other Herschel-Bulkley parameters constant [132]. Similar symmetric sigmoidal functions have also been used to describe the 'S' shape of a standard magnetisation (hysteresis) curve of a solid, where the initial linear relation between magnetisation and field strength tapers off once the material saturates [138, 139]. Based on this information, it was found to be possible to fit the MR fluid viscosity data at a constant temperature by allowing all three Herschel-Bulkley parameters to depend on magnetic field strength with a symmetrical sigmoidal function. Specifically, the error function was used, resulting in equation 5.3 where C is one of the three Herschel-Bulkley parameters (τ_y, m or K), c_1 to c_4 are the fit constants, and H is the magnetic field strength in $\mathrm{A\,m^{-1}}$.

$$C = c_1\,\mathrm{erf}(c_2\,(H - c_3)) + c_4 \tag{5.3}$$

With equation 5.3, the Herschel-Bulkley model was fitted to the viscosity data from figure 5.3 for a constant temperature of 36°C (the assumed fluid film temperature in the bearing). Finally, including the effect of variations in temperature was achieved by simply multiplying the Herschel-Bulkley fit at 36°C with a normalised exponential expression, resulting

Table 5.2: Coefficient values for the magnetic field strength–dependent Herschel-Bulkley viscosity fit of MRHCCS4-A.

C	Unit	c_1	c_2	c_3	c_4
τ_y	Pa	6605	5.151×10^{-6}	1.601×10^{5}	5013
K	$\mathrm{Pa \cdot s}^{m}$	210.3	1.007×10^{-5}	2.553×10^{5}	210.7
m	-	0.9614	1.039×10^{-5}	1.570×10^{5}	1.992
β	$°\mathrm{C}^{-1}$	3.638×10^{-2}	3.785×10^{-5}	0	-4.260×10^{-2}

in equation 5.4 where β is the temperature-viscosity coefficient and $T_0 = 36°\mathrm{C}$. A similar viscosity-temperature dependence for MR fluids has been found previously in literature [137], although the slightly more complex Arrhenius equation was used in that case.

$$\eta = \frac{\tau_y + K|\vec{\dot{\gamma}}|^m}{|\vec{\dot{\gamma}}|} e^{\beta\,(T - T_0)} \tag{5.4}$$

The magnetic field strength–dependence of β could be modelled with equation 5.3 as well, the final values for all of the fit constants for τ_y, m, K, and β are shown in table 5.2. The viscosity model obtained with these values combines three basic relations for the rheology of an MR fluid, relating apparent viscosity to shear stress (Herschel-Bulkley), temperature (exponential fit), and magnetic field strength (symmetric sigmoidal). For engineering purposes this basic combination was found to be sufficiently accurate: at a constant temperature of 36°C, with varying shear rate and magnetic field strength, this fit has a normalised RMSE of 0.044, for temperatures of 20°C and 70°C this changes to 0.0858 and 0.102 respectively. Keeping the magnetic field constant instead and fitting for varying shear rate and temperature results in a normalised RMSE of 0.0866 at $0\,\mathrm{kA\,m^{-1}}$ and 0.0580 at $440\,\mathrm{kA\,m^{-1}}$.

5.2.4 Numerical model

The experimental measurements obtained with the setup have been compared to a numerical model that was developed previously. This paper will only show the equations required to solve the numerical model, for the full derivation the reader is referred to our previous paper [140]. The aim of the comparison in this paper was to verify the accuracy of the model when applied to MR fluids, and to check its usefulness for optimisation of the magnetic field. This isothermal model is based on the laminar 2D Reynolds equation and incorporates cavitation, as well as the non-Newtonian characteristics of an MR fluid.

Starting with the Herschel-Bulkley model, the apparent viscosity is once again determined by rewriting equation 5.1 using the form $|\vec{\tau}| = \eta|\vec{\dot{\gamma}}|$, but unlike equation 5.2 where the viscosity was expressed as a function of the shear rate, equation 5.5 shows the viscosity as a function of the shear stress.

$$\begin{gathered} \eta = \frac{K^{\frac{1}{m}}|\vec{\tau}|}{f\left(|\vec{\tau}| - \tau_y\right)^{\frac{1}{m}}} \\ f = \begin{cases} 1 & \text{if} \quad |\vec{\tau}| \geq \tau_y \\ 0 & \text{if} \quad |\vec{\tau}| < \tau_y \end{cases} \end{gathered} \tag{5.5}$$

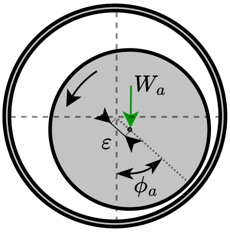

Figure 5.4: The position of the shaft inside the bearing is defined with the eccentricity ε and the attitude angle ϕ_a, with the applied load W_a acting on the shaft. The curved arrow on the left indicates the rotation direction of the shaft.

In order to use the Herschel-Bulkley model with the Reynolds equation, a modification is required to allow viscosity variations over the film thickness. To account for this, a generalised Reynolds equation has been derived following the method pioneered by Dowson [70], resulting in equation 5.6. Here F_0, F_1, and F_2 are flow factor integrals that depend on the apparent viscosity, $\vec{u}_b$ is the velocity of the shaft, and h is the film thickness given by equation 5.7, with nominal film thickness h_0, eccentricity ε, and attitude angle ϕ_a (see figure 5.4).

$$\vec{\nabla}\left(-h^3\left(F_2 - \frac{F_1^2}{F_0}\right)\vec{\nabla}\xi + \psi h\left(1 - \frac{F_1}{F_0}\right)\vec{u}_b\right) = 0 \tag{5.6}$$

$$h = h_0(1 + \varepsilon\cos(\phi - \phi_a)) \tag{5.7}$$

In this Reynolds equation, cavitation is included using mass-conserving JFO boundary conditions, which are implemented by replacing both the pressure p and lubricant fraction ψ with functions of a new variable ξ (see equations 5.8 and 5.9) [52]. By assuming that every point in the bearing is either part of a full film region ($p > 0$, $\psi = 1$) or a cavitated region ($p = 0$, $0 \leq \psi < 1$), the generalised Reynolds equation can be solved for ξ, with the positive part representing the pressure, and the negative part representing the mass fraction.

$$p = (\xi \geq 0)\xi \tag{5.8}$$

$$\psi = 1 + (\xi < 0)c_f\xi \tag{5.9}$$

Numerical stabilisation is required to prevent oscillations in the convection-dominated cavitation region, in this case artificial diffusion has been implemented which is controlled by the variable c_f in equation 5.9. It is possible to calculate the minimum value of c_f that will still prevent oscillations [52, 140], which results in equation 5.10, where h_e is the local mesh size.

$$c_f = \left(F_2 - \frac{F_1^2}{F_0}\right)\frac{h^2}{h_e\left(1 - \frac{F_1}{F_0}\right)\vec{u}_b} \tag{5.10}$$

The flow factors that appear in the Reynolds equation are calculated with equation 5.11, where the inverse of the viscosity is integrated over the film thickness coordinate z. As

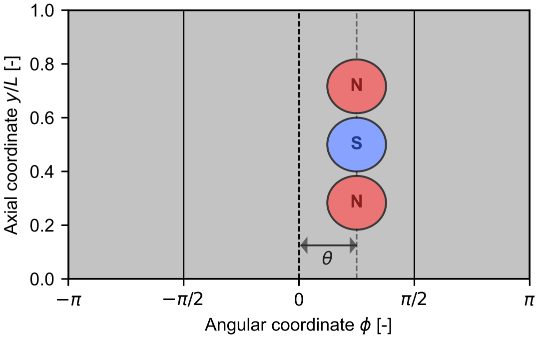

Figure 5.5: The 2D computational domain of the journal bearing. Two inlets spanning the entire axial length of the bearing are indicated at $\phi = -\pi/2$ and $\phi = \pi/2$. A row of three magnets is placed at $\phi = \theta$, their dimensions can be found in table 5.1 and the pole of the magnets that is closest to the fluid film is indicated with N(orth) or S(outh).

can be seen in equation 5.5 for the viscosity, this requires a formula for the shear stress $\vec{\tau}$ as a function of z, which is provided by equation 5.12.

$$F_n = \int_0^h \frac{z^n}{\eta} \mathrm{d}z \tag{5.11}$$

$$\vec{\tau} = \left(z - \frac{F_1}{F_0}\right)\vec{\nabla}p + \frac{\vec{u}_b}{F_0} \tag{5.12}$$

Finally, a solution to the numerical model is obtained by solving the Reynolds equation (equation 5.6) for ξ, equation 5.11 for the flow factors F_0, F_1, and F_2, and the horizontal and vertical load balances F_x and F_y for the shaft attitude angle ϕ_a and eccentricity ε respectively (equations 5.13 and 5.14)[1].

$$F_x = \iint_S p \sin\phi \,\mathrm{d}A = 0 \tag{5.13}$$

$$F_y = \iint_S p \cos\phi \,\mathrm{d}A - W_a = 0 \tag{5.14}$$

Magnetic field calculation

The final requirement for solving the numerical model is the magnetic field in the film, which will be determined numerically. For this paper, the magnetic field that was used in the experiments was generated by three neodymium permanent magnets placed side-by-side in the axial direction, as shown in figure 5.2. During these experiments, the strength of the magnets was varied (by changing their length, denoted by dimension L3) as well as their angular position (in the ϕ-direction). Figure 5.5 shows the 2D computational domain

---

[1] *Footnote not present in original publication* - A small mistake was made in writing down these equations, the surface integral is written as $\iint_S$ which means the differentials should be written as dS instead of dA.

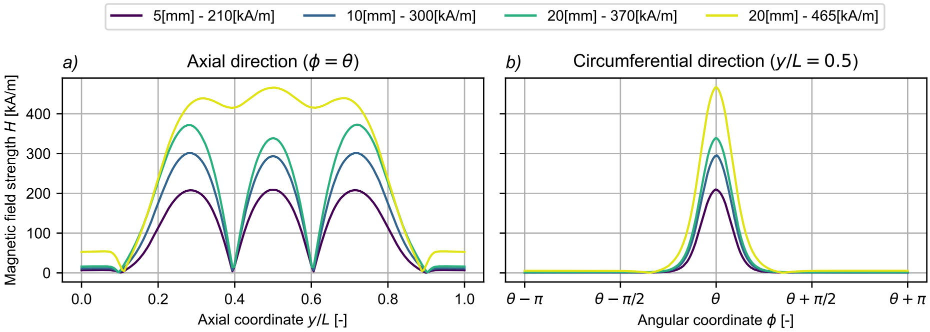

Figure 5.6: The fluid film magnetic field strength H in a) the axial and b) the circumferential directions for different magnet lengths L3. The legend indicates the length of the magnets, and the peak field strength value. By increasing the size of the magnets, the magnetic field in the fluid film is increased. Note that the polarity of the central magnet in figure 5.5 was switched from S to N to reach the strongest field with a peak strength of 465kA m^{-1}.

of the Reynolds simulation, where the angular position of the magnets is indicated with the angle θ. Note that the polarity of the magnets was alternated in an attempt to reduce the magnetic field strength in the film outside the area covered by the magnets. This was done in an attempt to reduce the friction increase, since the magnetic field simulations indicated that with opposing polarities, the strength of the field far away from the magnets would be much lower (relative to the strength close to the magnets) compared to having the same polarities. The aim was to use this to focus the viscosity increase on the area of the film directly below the magnets, while limiting the viscosity increase far away, thereby limiting the increase in friction. One experiment has also been performed where the polarisation of the magnets was not alternated, to maximise the magnetic field in the film.

For the purposes of the magnetic field simulation, only the magnets themselves, the housing, and the shaft are considered. Both the inner and outer bearing bush are non-magnetic, and the influence of magnetisable components outside the bearing housing was found to be negligible. Furthermore, small features in the geometry of the housing (internal channels, bolt holes, bolts, etc...) are removed to reduce complexity, meaning that the final bearing housing geometry is axisymmetric in the simulation. As a result, the magnetic field in the film is only calculated for different magnet sizes at $\theta = 0$, for other angles θ that magnetic field solution is simply shifted in the ϕ-direction by θ radians. The resulting 3D magnetic field simulation is implemented in the FEM software package COMSOL Multiphysics® 6.1 [51] with the standard ’Magnetic Fields, No Currents (mfnc)’ interface. This simulation is almost identical to the one performed in our previous work, for details about the implementation in COMSOL or the computational geometry, the reader is referred to that work [105]. The only difference with that paper is the variation of the length of the magnets. The resulting magnetic fields in the fluid film are shown in figure 5.6 as a function of this length and for a constant magnet angle of θ radians. The strongest magnetic field in this figure, with a peak strength of 465kA m^{-1}, is the field that was created by placing all three magnets in the same polarity direction (switching the polarity of the central magnet from S to N, see figure 5.5). This is the reason why the magnetic field strength does not go to zero in between the magnets, in contrast to the other magnetic fields. For simplicity, the magnetic fields will be referred to by their peak field strength values from now on.

Software implementation

The full numerical model is solved with the FEM software package COMSOL Multiphysics® 6.1 [51]. The Reynolds equation and flow factors (equations 5.6 and 5.11) are implemented as General From PDE's with quadratic Lagrangian shape functions, while the load balances (equations 5.13 and 5.14) are implemented as global equations. Note that the flow factor integrals are evaluated with COMSOL's numerical integration routine `integrate`. The 2D computational domain on which the equations are solved is meshed with a structured quadrilateral mesh with 10000 (100 × 100) elements. The domain is shown in figure 5.5, a periodic boundary condition is used to connect the solution at $\phi = -\pi$ and $\phi = \pi$ (equation 5.15), while Dirichlet boundary conditions setting $\xi = 0$ are placed on both the inlets at $\phi = -\pi/2$ and $\phi = \pi/2$ and outlets at $y = 0$ and $y = 1$ (equation 5.16). A constant pressure boundary condition has been chosen for the inlets, because while the lubricant is being pumped by a constant volume pump, the inlet grooves extend along the entire length of the bearing and connect directly to both outlets. For this reason it is expected that the bearing will only take as much lubricant from the inlet flow as it needs, while the rest of the inflowing lubricant flows directly to the outlets through the inlet grooves.

$$\xi_{\phi=-\frac{\pi}{2}} = \xi_{\phi=\frac{\pi}{2}} \tag{5.15}$$

$$\xi = 0 \quad \text{at} \quad y = 0,\ y = 1,\ \phi = -\frac{\pi}{2}, \phi = \frac{\pi}{2} \tag{5.16}$$

The problem is solved with the standard COMSOL Newton-Raphson solver with under-relaxation for a total of 311 010 degrees of freedom, convergence is assumed when the relative tolerance on the solution is lower than 1×10^{-3}. The model has been validated for a relative tolerance of 1×10^{-6} (see also [140]), as an indication, the difference with a tolerance of 1×10^{-3} is on average about 0.1% for the film thickness. The solver uses three steps, the first step solves only the Reynolds equation, the second steps solves the Reynolds equation and flow factors, and the final step solves the Reynolds equation, flow factors, and load balances. The solver is modified slightly for the final step, where the relaxation factor is set to a constant value of 0.2, for the other steps this factor is chosen automatically.

5.3 Results and discussion

This section presents the results of the experimental and numerical work that was performed, and is divided into three subsections. The first subsection describes an initial optimisation of the angle of the magnets with the numerical model, and shows the experimental verification. In the second subsection, this optimised angle is used while varying the magnetic field strength and the applied load. This is done both experimentally and numerically, and the results are compared with that of the reference lubricating oil. The final subsection discusses the deviations between the numerical model and the experiments.

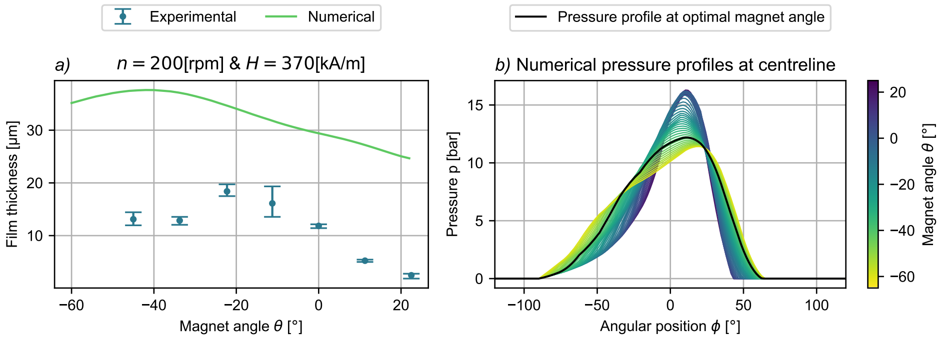

Figure 5.7: *a)* Minimum film thickness at 200rpm and with a peak field strength of 370kA m^{-1}, as a function of the angle of the magnets θ. The experimental results all have error bars that indicate the maximum and minimum film thickness that was measured during the three repetitions of every magnet angle measurement. *b)* The corresponding numerical pressure profiles at the centreline of the bearing as a function of the angle of the magnets θ. The pressure profile for the optimal angle is marked.

5.3.1 Magnet angle optimisation

It was decided to start the investigation by using the model to optimise the angle θ of the permanent magnets (see figure 5.5), and to use the experimental setup to verify these results. The goal of this optimisation was to find the angle where the localised increase in film viscosity due to the magnetic field would result in the largest increase in film thickness (or equivalently, the largest decrease in eccentricity). Since the optimal angle was found to vary with speed, the optimisation was performed for a constant (low) speed of 200rpm, at this speed the bearing was experimentally found to be in mixed or boundary lubrication without the presence of a magnetic field. The reason for optimising at low speed, instead of at high speed, is that in most situations the film of a bearing would already be sufficiently thick at high speeds. Increasing the viscosity would make it even thicker, but would mostly just reduce efficiency since it also increases friction. Optimising the magnetic field to increase film thickness at low speeds is expected to be more useful, since this reduces the transition speed, meaning the minimum speed where the bearing is still in the hydrodynamic regime. It would have been more effective to optimise the transition speed directly, and for an oil-lubricated bearing this could be done by checking when the minimum film thickness becomes smaller than the combined roughness of the shaft and bearing [141]. With an MR-lubricated bearing this is not possible due to the presence of the microparticles in minimum film, which are expected to have a large influence on the low speed hydrodynamic performance of the bearing (as will be discussed at the end of section 5.3.2). For that reason the model is only valid in the hydrodynamic regime.

Figure 5.7a shows the results of the numerical optimisation, with film thickness plotted as a function of the angle of the magnets, as well as the experimental verification that was performed afterwards for a select number of magnet angles. Note that the verification could not be performed for magnet angles lower than −45°, since that would cause the support bracket holding the magnets to collide with one of the inlets. Figure 5.7b shows the corresponding numerically calculated pressure profiles at the centreline of the bearing.

When examining the results, it can be seen that both the experimental and numerical results indicate the existence of an optimal angle that maximises the film thickness at minimum film. Specifically, the optimisation predicts an optimum around −42° with a film thickness of 37.6μm, whereas the experiments show the optimum to lie around −22.5° with a film thickness of 18.4μm.

Counter to the initial expectations of the authors, both the model and experiments show that the optimum lies quite far upstream from minimum film (which the experiments indicate lies between $20 < \phi < 40$ for 200rpm, depending on the exact value of θ), and that placing magnets near or just after minimum film does not result in a higher pressure peak. Instead, placing the magnets farther upstream from minimum film results in a lower but also wider pressure peak, with an overall higher load capacity. Placing the magnets too far upstream will reduce the load capacity again, since the pressure profile will be so wide that a substantial part will act mostly in the horizontal direction.

It seems intuitive to think that this might in some way be related to the strong shear-thinning characteristics of the MR fluid. The shear rate will be relatively high near minimum film, and the effect of the magnetic field on the viscosity will therefore be smaller than in regions of the film with lower shear rates. However, rerunning the simulation while assuming a constant shear rate for the purposes of calculating the viscosity (meaning that the fluid is no longer shear-thinning and that its viscosity depends only on the magnetic field strength) gives qualitatively similar results. It therefore seems that the optimum may actually be caused by the geometry of a journal bearing, not by the shear-thinning rheology of the MR fluid.

5.3.2 Varying magnetic field strength and load

In this section, experimental and numerical Stribeck curves are shown for the MR-lubricated bearing, first with a varying magnetic field strength and then with a varying applied load. These results will be shown alongside the results for oil lubrication, to see how MR lubrication compares with a more traditional lubricant. During the MR measurements, the angle of the magnets is set to the optimal value (for the specific magnetic field used in this research) of $\theta = -22.5°$ identified experimentally in the previous section. It is worth mentioning that the model predicts that the optimal angle is dependent on the magnetic field strength, however, in this research the angle was kept constant for all measurements. The reason for this is that the goal of these experiments was to show the effects of magnetic field strength and load in isolation, not to find the most optimal configuration for this specific bearing.

Magnetic field strength variation

Figures 5.8a and 5.8b present experimental and numerical Stribeck curves for the MR-lubricated bearing as a function of magnetic field strength (with the magnets positioned as in figure 5.5 at $\theta = -22.5°$) for a constant load of 2.5kN/0.5MPa. Figures 5.8c and 5.8d present the corresponding film thickness plots, and all figures also show the curves for the bearing lubricated with the reference oil. For the experimental results, the dashed lines represent the average of the three repetitions of every measurement, and the shaded areas represent the maximum and minimum friction or film thickness values recorded during those three tests. The differences between the experimental and numerical results

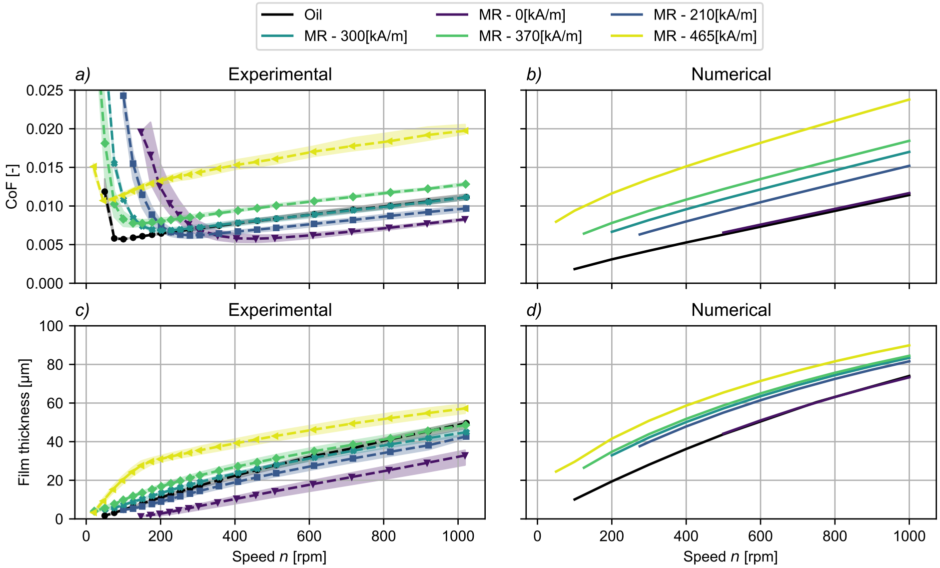

Figure 5.8: Experimental and numerical Stribeck curves and minimum film thickness plots for the bearing lubricated with oil and with MR with varying magnetic field strength (respectively *a* & *c* and *b* & *d*). The position of the magnets is constant, only the strength of the magnets is changed. A constant load of 2.5kN/0.5MPa is applied to the bearing.

are obviously large, especially for the film thickness, but this will be discussed further in section 5.3.3 as was mentioned before.

Both the experimental and numerical results do very clearly illustrate the effect that a magnetic field has on the viscosity of an MR lubricant. Increasing the strength of the magnetic field causes the lubricant viscosity to go up at the location of the magnets, which in turn causes thicker films and an associated reduction of the transition speed (defined as the speed where the friction coefficient has a minimum), but also an increase in the level of friction in the bearing. Furthermore, the results show that seemingly minor changes in the exact distribution of the field throughout the film can have large effects on the overall behaviour of the system. This can be seen by comparing the (experimental) Stribeck and film thickness curves for the field with peak a strength of 465kA m^{-1} and the curves with the lower peak field strengths. As an example, both the 370 and 465kA m^{-1} fields were created with three 20 × 20mm cylindrical magnets placed in a line in the axial direction, but where the 465kA m^{-1} field was generated by having the polarity of all three magnets in the same direction, the weaker field was generated with the central magnet rotated to have its polarity opposite to its neighbours. As discussed in section 5.2.4, this polarity change was implemented in an attempt to reduce the friction increase by focusing the magnetic field (and therefore the viscosity increase) on the area of the film directly beneath the magnets. As a side effect, the peak magnetic field strength was reduced and the shape of the magnetic field beneath the magnets was changed as well (see figure 5.6). One of these changes did seem to have the desired effect, at least at high speed, since at 1000rpm the film thickness with the 465kA m^{-1} field is around 18% higher than with the 370kA m^{-1} field, while the friction is more than 50% higher. However, at lower speeds the effects of these changes are different, and the 87% increase in film thickness is accompanied by an increase in friction of only 65%. It shows that it is very important to accurately determine exactly which parts of the film should be magnetised when designing an MR-lubricated bearing.

The friction and film thickness curves for the same bearing lubricated with the reference oil are shown in figure 5.8 as well. When comparing these curves with the ones for MR lubrication, it is interesting to notice that the MR-lubricated bearing can achieve either lower hydrodynamic friction and a higher transition speed (without a magnetic field), or a lower transition speed and higher hydrodynamic friction (with the 465kA m^{-1} field), but not both lower friction and a lower transition speed. Things become especially peculiar when looking at the curves of the bearing magnetised with the 300kA m^{-1} magnetic field. Even though the hydrodynamic friction coefficient is almost exactly the same as with oil lubrication, the transition speed is still more than 100rpm higher. In spite of that, the film thickness plot shows that the film thickness of the MR-lubricated bearing at its transition speed is actually slightly higher than that of the oil-lubricated bearing. Furthermore, the transition from hydrodynamic to mixed or boundary lubrication occurs relatively suddenly with oil lubrication, with a sharp increase in friction once the shaft touches the bearing surface. With MR lubrication on the other hand, this transition is much more gradual and there almost appears to be a transition region instead of a discrete, well-defined transition speed. It is hypothesised that all of these effects are related, and are caused by the presence of the large concentration of particles in the MR fluid (70% by mass or around 20% by volume).

At high speeds, the particles will be in suspension, but when the speed is lowered and the shaft starts approaching the bearing surface, it may be assumed that particles will be trapped between the two surfaces. Because there are so many particles, this could result in a layer that is multiple particles thick, with the shaft sinking further and further into this layer the lower the speed becomes. The gradual increase in the compressive forces would then correspond to the gradual transition increase in friction observed during the experiments. However, while wear tests using MR lubricant have shown that particles are present in the contact zone during boundary lubrication [54, 55], the behaviour of the particles during very low speed hydrodynamic lubrication is not known in literature. This will require further research.

Load variation

Figures 5.9a through c show the experimental and numerical Stribeck curves for oil and MR lubrication at three different loads, with figures 5.9d through f showing the corresponding film thicknesses. To illustrate the effect of the magnetic field under increasing load, the MR fluid was tested both without a magnetic field, and with the strongest magnetic field with a peak strength of $H = 465\text{kA m}^{-1}$.

Starting with the standard lubricating oil, the Stribeck curves and film thickness plots (figures 5.9a and 5.9c) show that the bearing exhibits the expected behaviour, with a higher load leading to a lower friction coefficient, a smaller film thickness, and a lower transition speed. Other than the transition speed, these trends are also captured by the hydrodynamic numerical model, although the absolute values clearly deviate, as was already

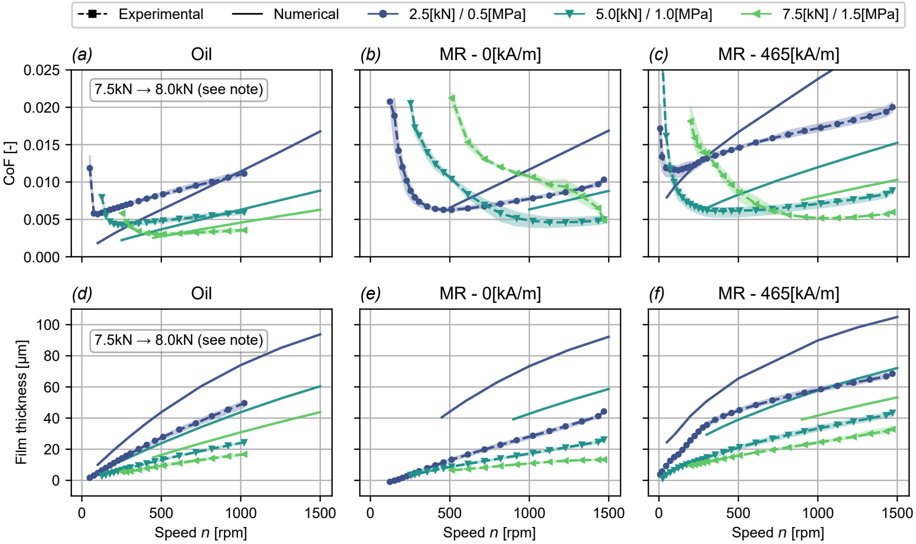

Figure 5.9: Experimental and numerical Stribeck curves and minimum film thickness plots for three different loads. As indicated in the legend, the line type specifies whether the Stribeck curve is experimental (dashed lines with markers) or numerical (solid lines), while the line colours indicate the applied loads. Tests were performed with oil lubrication (*a* & *d*), MR lubrication with zero magnetic field (*b* & *e*), and MR lubrication with a strong magnetic field (*c* & *f*).
Note that the high load oil measurements were accidentally performed at 8.0kN/1.6MPa instead of 7.5kN/1.5MPa.

observed in the previous section. Comparing these curves with those of the unmagnetised (figures 5.9b and 5.9e) and magnetised (figures 5.9c and 5.9f) MR-lubricated bearing does not immediately show any qualitative differences. It should be noted that all MR fluid measurements were performed with a higher starting speed of 1500rpm, the maximum speed of the motor. This was necessary for the measurements with unmagnetised MR lubricant loaded to 5.0kN and 7.5kN. Due to the low viscosity of the unmagnetised MR lubricant the bearing never reached hydrodynamic lubrication when starting at 1000rpm with these loads, and even 1500rpm was not high enough with a load of 7.5kN. Applying the magnetic field solved this issue by reducing the transition speed to around 1000rpm for this load, demonstrating once again the large effect of the magnetic field on the MR lubricant viscosity.

However, there does appear to be a difference in the way that the performance of the oil and MR-lubricated bearings scales with the applied load. This is especially obvious when comparing the transition speeds. At the lowest load, the transition speed of the MR-lubricated bearing goes from around 500rpm without magnetic field to around 75rpm with magnetic field, which is actually slightly lower than the 100rpm transition speed of the oil-lubricated bearing. In contrast, at the highest load the transition speed is only around 1000rpm with magnetised MR lubrication, compared to around 500rpm with oil. The medium load of 5kN falls in between these two extremes.

The reason for this difference in scaling can be likely attributed to the shear-thinning

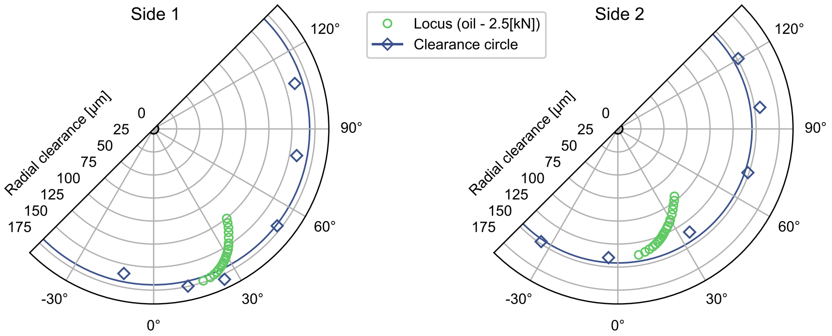

Figure 5.10: A representative example of the loci of the shaft as measured on the left and right sides of the bearing. The diamonds represent the data points obtained during the clearance circle measurement, the solid lines are the circles fitted through these data points, and the green circles represent the locus measurements for oil lubrication at 2.5kN / 0.5MPa.

characteristics of the MR fluid. Higher loads will lead to higher film pressures, and therefore to higher shear rates, in particular in the converging section of the film where the pressures are large. Higher shear rates will reduce both the viscosity itself, and the increase in viscosity due to the application of a magnetic field (see figure 5.3b). At a higher load, the bearing will therefore experience (relative to lower load) a smaller increase in film thickness and friction, meaning also a smaller reduction in the transition speed, which is exactly what was observed experimentally. Some of this could likely be mitigated by magnetising a larger amount of fluid in the film, for example by adding additional rows of permanent magnets parallel to the single row used in the experiments (see figure 5.5). This would increase the amount of magnetised, high viscosity lubricant, thereby increasing the pressure generation. Similarly, stronger magnetic fields could be used, although it should be taken into account that the particles in the fluid will saturate at some point. All in all, it seems that the shear-thinning properties of the MR lubricant used in this research may necessitate these additional measures when the load on the bearing increases, which is obviously not the case with standard Newtonian lubricating oils.

5.3.3 Discussion on the numerical model

As was remarked in the previous sections, there are clear and large deviations between the experimental and numerical results presented in figures 5.7 through 5.9, both for the friction coefficient and for the film thickness. Though the general trends in friction and film thickness are similar for both the experimental and numerical results, the quantitative differences are large enough to require additional investigation. Three main ways have been identified in which the numerical results differ from the experiments, these will be referred to as points 1, 2, and 3 hereafter:

1. The model overpredicts both the friction coefficient and the film thickness for all operating conditions, independent of the type of lubricant.
2. The model underpredicts the increase in film thickness due to an increase in mag-

netic field strength with the MR-lubricated bearing (figures 5.9e and 5.9f).

3. The model does not predict any differences between oil and unmagnetised MR lubrication, even though the experimental results clearly show that such a difference exists (figures 5.9d and 5.9e).

To explain these differences, an extensive investigation was performed into phenomena that were not included in the initial model, but could feasibly affect the experimental results. This included effects such as elastic deformation of the steel and polymer bearing sleeves and of the steel housing, actuator and bearing housing misalignment, wear or running-in of the polymer bearing sleeve, and the exact inlet boundary conditions used in the model. For the specific setup in this paper, all of these effects were found to have negligible influence on the film thickness and friction of the bearing. The rest of the section will discuss the remaining phenomena that are expected to play a larger role in the experiments.

Bearing sleeve shape errors

The first phenomenon that is expected to affect the performance of the bearing is related to the bearing geometry. As was mentioned in section 5.2, the film thickness in the bearing is determined as a function of shaft speed by averaging the film thickness measured on both sides of the bearing with two sets of two capacitive distance sensors mounted 90° apart. These sensors are calibrated by measuring the clearance circles of the bearing, which are effectively constructed by loading the bearing at zero speed such that the eccentricity of the shaft is set to $\varepsilon = 1$. The capacitive sensors are read out in this position, and this process is then repeated for a number of attitude angles $0 \leq \phi_a \leq 2\pi$ (12 positions were used in this paper). The resulting measurements form collections of points through which the clearance circles can be fitted, which will always bound the shaft locus measurements for non-zero speeds since $\varepsilon \leq 1$ in that case. Figure 5.10 shows a representative example of the loci and (one half of) the clearance circles measured on both sides of the bearing, examining the differences between side 1 and 2 immediately reveals two issues. First of all, the radial clearance on side 1 is 25µm larger than on side 2 (170µm vs 145µm) which means the bearing is tapered, this was also verified with a 3-point micrometer. Second, the collections of data points forming the clearance circles do not lie perfectly on the fitted circles, the fits have standard deviations of 9.0 and 6.0µm for sides 1 and 2 respectively, indicating cylindricity errors. Specifically, on side 1 the data points indicate the presence of a shallow groove between roughly 10 and 30°, with the locus showing that the shaft gets stuck in this groove at low speeds. On side 2 this groove is not present, the radial clearance in that location is instead smaller than predicted by the fitted circle, causing the shaft locus to move towards the 0° position as expected. Due to these shape errors, and due to the differences in shape between the two sides, the shaft and bearing are forced into a mostly horizontal misalignment at low speeds, with an 8.5° difference in attitude angle at the lowest speed. Compare this to the highest speed, where the attitude angles are effectively the same on both sides. In contrast, the amount of vertical misalignment seems minimal since the eccentricities on both sides are fairly similar at the lowest speeds, on both sides the loci approach the actual clearance circles implied by the data points when the speed is lowered. The lack of vertical misalignment in spite of the taper of the bearing means that the bearing has rotated such that it is parallel to the shaft around minimum film, which is possibly because the load is applied to hydrodynamic bearing housing through a hydrostatic bearing, which is not perfectly stiff against rotations.

The reasons for the existence of these shape errors are not known exactly, but similar issues have been observed before with polymer bearings for water lubrication [141]. Possible causes of the shape errors were stated to be machining or assembly errors, water soaking, thermal expansion, and/or progressive wear. Since the shape errors of the bearing in the current paper were already present before the start of the first measurement, machining or assembly errors seem the most likely.

The exact influence of these shape errors on the film thickness and friction coefficient in the model is difficult to determine without accurately measuring the entire geometry of the bearing sleeve, which is not a trivial task. However, it is known that shape errors can have a large (negative) effect on the film thickness of a journal bearing [142], which means it is feasible that these errors are at least part of the reason for the poor predictions of the model (specifically points 1 and 2 at the start of section 5.3.3). It is also feasible that the misalignment of the shaft at low speed affected the optimal position of the magnets (see figure 5.7), possibly explaining why the predicted optimum differed from the measured one. For these reasons it is recommended that future research using polymer bearings for MR lubrication focuses on careful machining and verification of the bearing shape, to minimise any errors in the geometry.

Film temperature

Another likely reason for some of the differences between the model and experiments relates to the temperature of the fluid film in the bearing. Based on the measurements of the thermocouples in the sleeve and in the outlet flow, the fluid film was assumed to be isothermal at 36°C for the purposes of the model. However, these thermocouple measurements are likely poor indicators of the actual film temperature. The reason for this is that thermocouples T0 through T2 in the sleeve (see figure 5.2 for their placement) only measure the temperature of the outer steel sleeve used to reinforce the inner polymer bearing bush. This was done to make manufacturing and assembly easier, but since polymers conduct heat poorly the thermocouples are separated from the fluid film by 4mm of what is effectively an insulator. After this was realised, thermocouples T3 and T4 were placed in the outlet flow in an attempt to get a better estimate. While the temperatures reported by these thermocouples were 1 to 2 degrees higher, these results were found to be poor indicators as well due to the design of the lubrication grooves. To simplify manufacturing, these grooves span the entire axial length of the bearing meaning that part of the $0.3\,\mathrm{L\,min^{-1}}$ inlet flow of cold 32°C lubricant will flow directly to the outlets. T3 and T4 therefore measure the temperature of a mixture of hot and cold lubricant, and cannot be used as an indication of the film temperature either.

All in all, it can be concluded that the thermocouples used in the setup underestimate the actual film temperature. Since higher film temperatures will result in lower friction and film thickness, this issue could address point 1 in section 5.3.3. To investigate this a bit more, figure 5.11 shows the experimental results for varying bearing load from figure 5.9, with updated model results for a constant temperature of 45°C. At this film temperature, the model was found to fit the experimental film thickness results for oil lubrication very

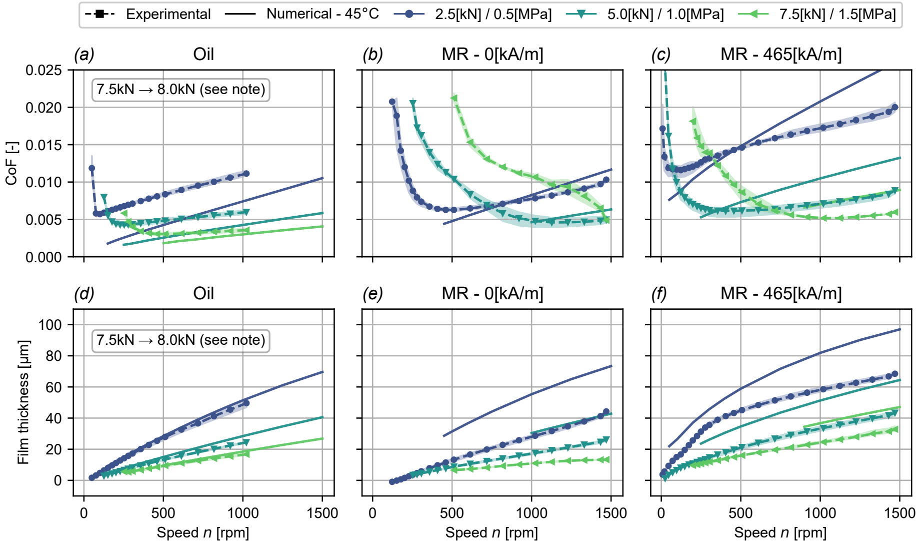

Figure 5.11: Experimental and numerical Stribeck curves and minimum film thickness plots for three different loads. As indicated in the legend, the line type specifies whether the Stribeck curve is experimental (dashed lines with markers) or numerical (solid lines), while the line colours indicate the applied loads. The experimental data in this figure is identical to the data in figure 5.9, but the numerical results are for an isothermal fluid film temperature of 45°C, instead of 36°C.
Note that the high load oil measurements were accidentally performed at 8.0kN/1.6MPa instead of 7.5kN/1.5MPa.

well (figure 5.11d), and predicts very similar slopes for the friction coefficients (figure 5.11a). A film temperature of around 45°C does not seem unreasonable based on the 36°C measured at the thermocouples, especially when considering that the film temperature could also be lower when the effects of the shape errors discussed in the previous section are taken into account.

The model results for MR lubrication at 45°C fit the experiments less well, especially for the film thickness, even though there are improvements. Specifically, the increase in film thickness due to the application of the magnetic field (point 2 at the start of section 5.3.3) matches the experimental results more closely at higher temperatures. For example, at 1500rpm the increase in film thickness changes from 12.8 to 23.5µm when the temperature goes from 36 to 45°C, with the experiments showing a 24.3µm increase. The reason for this is the dependence of the temperature-viscosity coefficient β on the magnetic field, with β rapidly becoming smaller with increasing field strength H (see section 5.2.3 and figure 5.3).

The absolute difference in film thickness is still large for the MR-lubricated bearing at 45°C. In fact, the isothermal temperature of the film would have to be 60°C for the unmagnetised bearing and 80°C for the magnetised bearing to have the model match the experiments. While it is to be expected that the magnetised bearing would have a higher film temperature due to the increased viscosity, these temperatures seem unrealistic considering the thermocouple measurements (despite their flaws). For the MR-lubricated bearings, temperature is therefore probably not the only effect with a significant influence on bearing performance.

Finally, it should be noted that the film temperature will not be isothermal in reality, which is something that can also affect the model results. With the model used in this research, determining the full 3D temperature profile inside the film requires solving an energy equation for the temperature in addition to the generalised Reynolds equation which is solved for the pressure, this has been done previously in literature [143]. The relation between viscosity and temperature is already defined by equation 5.4, meaning that the main difficulty lies with applying proper boundary conditions. For example, thermal conduction in the shaft would probably have to be taken into account, as well as the temperature distribution in the lubrication grooves.

MR fluids at very high shear rates

The final effect that could explain some of the differences between the model and the experiments is the behaviour of the MR fluid at very high shear rates. MR fluids are generally used in damping or braking systems where the shear rates are relatively low, and because of this commercially available rheometers for MR fluids focus on this low shear regime as well. For example, the cone-on-plate rheometer that was used for this paper is only capable of measuring shear rates up to 4000s^{-1}, at higher shear rates the fluid will be flung out of the gap due to the centrifugal forces. However, the numerical model shows that the shear rates in the film of the journal bearing setup are expected to have orders of magnitude of around 1×10^4 to $1 \times 10^5 \text{s}^{-1}$ (depending on the operating conditions), much larger than the shear rates that can be attained by any of the commercial magnetorheometers (which should be capable of both temperature and magnetic field control). The only high shear rate (up to $4 \times 10^4 \text{s}^{-1}$) viscosity measurements that could be found in literature were performed with custom-built magnetorheometers and different MR fluids [37, 144, 145].

In this paper, the high shear viscosity data required in the model was instead obtained by extrapolating the low shear rheometer data with the Herschel-Bulkely viscosity model (see equation 5.5). While the literature on custom high shear magnetorheometers found that this model can fit high shear rate MR viscosity curves quite well, that does not change the fact that the viscosity is still extrapolated over 1 to 2 orders of shear rate magnitude in our case. It is possible that errors resulting from this extrapolation could explain the differences between the model predictions for MR and oil lubrication as described by point 3 in section 5.3.3, since this issue does not affect the viscosity measurements of the Newtonian reference oil. However, this is impossible to find out without actually testing the MR fluid at these high shear rates using an appropriate (custom-built) magnetorheometer.

5.4 Conclusion

In the current research, the Stribeck curves and film thickness plots of a hydrodynamic journal bearing were compared experimentally and numerically for oil and MR fluid lubrication, under different loads and for different magnetic field strengths. Since the MR fluid used in this research had a lower viscosity than the oil when not magnetised, it was found experimentally that MR lubrication without a magnetic field resulted in thinner films and a higher transition speed, but also in lower hydrodynamic friction. On the other hand, a strong magnetic field caused a large increase in film viscosity and resulted in the thick films and low transition speeds frequently reported in literature, as well as the associated friction increase. Interestingly, it was not possible to obtain both a lower transition speed and lower high speed hydrodynamic friction with the MR lubricant compared to standard oil lubrication, irrespective of the magnetic field strength. This could be a negative influence of the presence of the MR particles in minimum film during low speed hydrodynamic lubrication. Finally, increasing the bearing load was found to lead to a reduction in the effect of the magnetic field on film thickness, transition speed, and friction coefficient, most likely because of the shear-thinning characteristics of the MR fluid combined with the higher shear rates due to the increased film pressures.

Designing a model to accurately capture all of these effects turned out to be difficult, with large deviations between the model predictions and the experimental findings. Part of this is probably related to the complex and only partially known rheology of an MR fluid, with a viscosity that depends on shear rate, magnetic field strength, and temperature. In this paper a basic relation was constructed for the apparent viscosity based on rheometer viscosity data as a function of these three parameters, showing this complexity. The other part of the deviations was likely caused by geometry errors in the polymer bearing used in the experiments. A polymer bearing was chosen for its wear properties under MR lubrication, but it has been found in literature that polymer bearings are more difficult to work with than traditional metal bearings, sometimes resulting in shape errors similar to those observed in the bearing used in this research. For that reason it is recommended that future research using MR-lubricated polymer bearings focuses on preventing geometry errors during the fabrication process.

Addendum – modified Hersey numbers for MR fluids

Throughout this dissertation all Stribeck curves show the friction coefficient as a function of the shaft speed instead of the Hersey number, because, as was stated in the introduction: ”Since MR fluids are shear-thinning and the shear stress varies throughout the film of a journal bearing, the viscosity of an MR film will vary throughout the bearing even when unmagnetised. The Hersey number, which is calculated with a single value for the viscosity in the entire bearing, is therefore no longer well defined” (see page 5). That claim is still correct, however, it might be possible to define a new Hersey number that depends on some other quantity that is representative of the viscosity in the bearing. If done correctly this quantity should reduce to the standard Hersey number for a Newtonian fluid, and would allow for a collapse of the MR Stribeck curves to one master curve. This addendum explores that concept for some of the experimental and numerical results shown in this chapter, and will present two possible choices for an alternative Hersey number.

The standard Hersey number is defined by equation 5.17, where η_{He} is the (usually Newtonian) fluid viscosity, n is the shaft speed, and P is the projected load.

$$\text{Hersey number} = \frac{\eta_{He}\; n}{P} \tag{5.17}$$

It seems reasonable to assume that with a non-Newtonian MR fluid the viscosity term in the Hersey number would in some way depend on the apparent viscosity η, meaning that $\eta_{He} = f(\eta) = g(H, n)$ with H the magnetic field strength. Since η_{He} should be a constant that represents the entire fluid film, a simple first approach would be to set η_{He} equal to the volumetric average of the apparent viscosity throughout the fluid film. The resulting modified Hersey number will be called ’variant 1’ from now on. The second approach, ’variant 2’, is very similar but will instead use one of the flow factors to get a measure of the film viscosity. For both variants the numerical model will be used to calculate η_{He} for the numerical and experimental Stribeck-Hersey curves.

Variant 1 – average viscosity

The volume-averaged apparent viscosity will always reflect any changes in the viscosity of the fluid film, even if only a small part of the film is magnetised. To obtain it, the height-averaged shear rate $|\vec{\dot\gamma}|_{avg}$ is calculated first by rewriting equation 5.5 using $|\vec{\tau}| = \eta|\vec{\dot\gamma}|$ to isolate the shear rate, which is then averaged over the film thickness resulting in equation 5.18.

$$|\vec{\dot\gamma}|_{avg} = \frac{1}{h}\int_0^h f\left(\frac{|\vec{\tau}| - \tau_y}{K}\right)^{\frac{1}{m}} \mathrm{d}z \tag{5.18}$$

Using equation 5.4 (at 36°C) then leads to the volume-averaged viscosity that will be used in the Hersey number, as shown by equation 5.19.

$$\eta_{He} = \frac{1}{S}\iint_S \frac{\tau_y + K\,|\vec{\dot\gamma}|_{avg}^m}{|\vec{\dot\gamma}|_{avg}}\,\mathrm{d}S \tag{5.19}$$

Note that it is not possible to average the apparent viscosity (equation 5.5) directly, since this term will go to infinity when the shear stress is lower than the yield stress at any point in he film. The height-averaged shear rate is determined first as a workaround, because it is zero at those locations (instead of infinity).

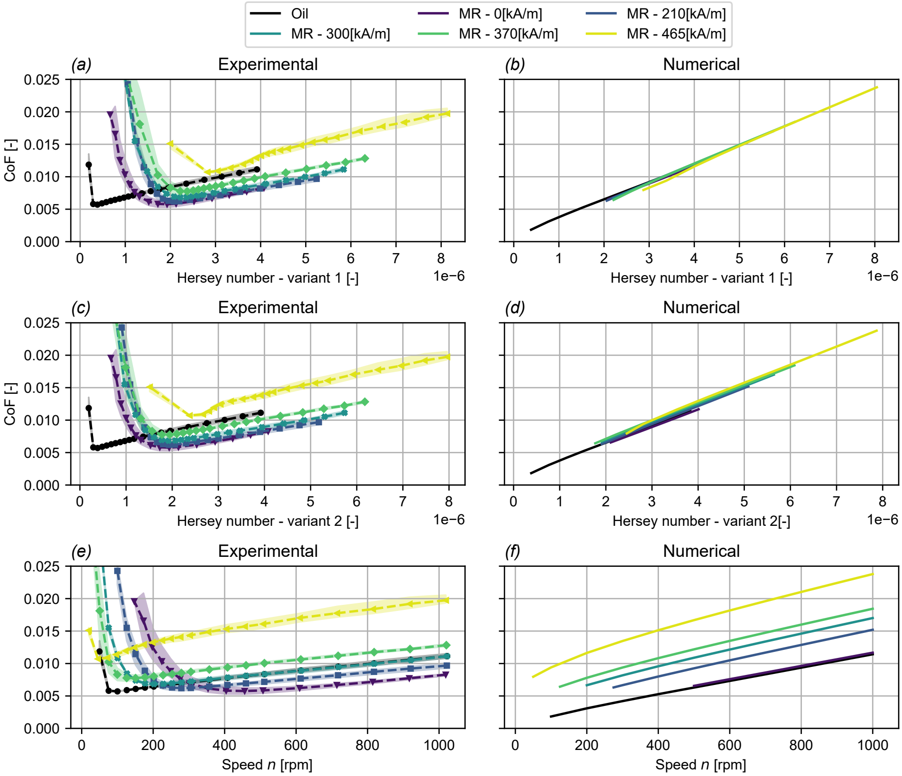

Figure 5.12: Stribeck-Hersey curves as a function of magnetic field strength for variant 1 (subfigures a and b) and variant 2 (subfigures c and d) of the modified Hersey numbers, as well as Stribeck curves as a function of the shaft speed *n* (subfigures e and f) which were previously presented in figure 5.8. All of these Stribeck curves were recorded with a constant load of 2.5kN.

Variant 2 – average flow factor

The second modified Hersey number was conceived after it was noticed that the flow factor F_0 (equation 5.20) is equal to the height-averaged inverse apparent viscosity when divided by the local film thickness. This approach therefore uses the average of the inverse of F_0 as a measure of the film viscosity, see equation 5.21. This is convenient since F_0 is calculated and stored during the FEM solution process, which means it is more easily and more quickly accessible than the volume-averaged apparent viscosity from variant 1.

$$F_0 = \int_0^h \frac{1}{\eta}\,\mathrm{d}z = \int_0^h \frac{f}{|\vec{\tau}|}\left(\frac{|\vec{\tau}| - \tau_y}{K}\right)^{\frac{1}{m}}\mathrm{d}z \tag{5.20}$$

$$\eta_{He} = \frac{1}{S}\iint_S \frac{1}{\frac{1}{h}F_0}\,\mathrm{d}S \tag{5.21}$$

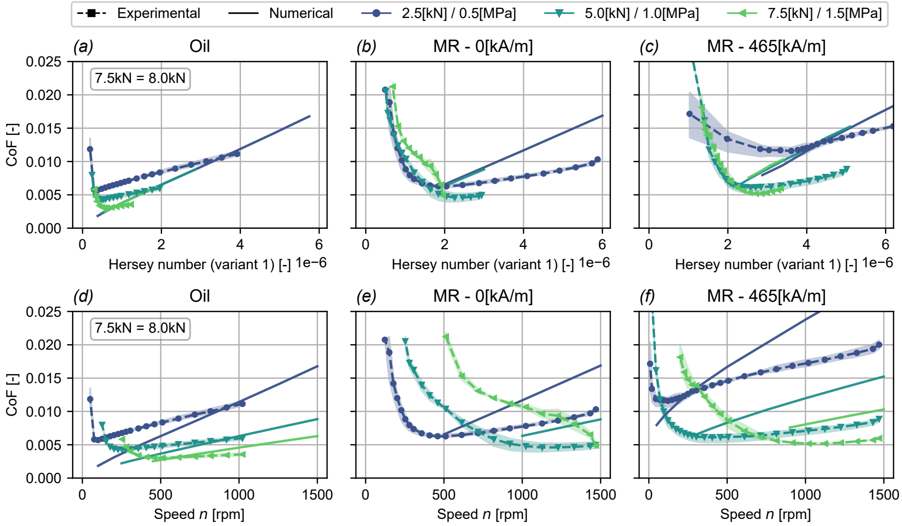

Figure 5.13: Stribeck-Hersey curves for variant 1 (subfigures a and b) of the modified Hersey number, and the Stribeck curves as a function of the shaft speed n (subfigures c and d) which were previously presented in figure 5.9. The results for variant 2 of the modified Hersey number are not presented here since they were very similar to the results with variant 1.

Results

Figure 5.12 shows experimental and numerical Stribeck-Hersey curves as a function of the magnetic field strength for both variants of the modified Hersey number using the friction data that was previously presented as a function of the n in figure 5.8. The viscosities η_{He} used to determine the Hersey numbers were calculated with the numerical model. As can be seen when comparing the experimental results in figure 5.8e with figures 5.8a and 5.8c, for both variants the curves with magnetic field strengths between 0 and 370kA m^{-1} more or less collapse to a single curve (variant 2 is especially effective here). However, in both cases the curves for oil lubrication and for lubrication with the strongest magnetic field (of 465kA m^{-1}) form clear outliers. Similar results are shown by the numerical curves. The fact that oil lubrication results in a lower transition point matches with earlier observations, and is likely caused by the presence of the particles in minimum film for speeds close to the transition speed, as discussed in section 5.3.2. A reason for why the 465kA m^{-1} curve forms an outlier is less readily available, though it could very well be related to the slightly different way in which this field was generated compared to the weaker fields (with the polarity of all magnets in the same direction, compared to the weaker fields where alternating polarity was used, see figure 5.6). Perhaps this difference is caused by the larger amount of fluid that is magnetised with the strongest magnetic field, or by the change in the shape of the area that is magnetised. At the very least it is clear that this result is not a fluke, figure 5.13 shows Stribeck-Hersey curves for various applied loads which reveals that the 465kA m^{-1} curves form outliers in those experiments as well. In fact, the curves do collapse to a single curve when looking at the figures for 0kA m^{-1} and

465kA m^{-1} individually, but not when taken together, meaning that the load dependence of the Hersey number is likely not affected by the non-Newtonian nature of the MR lubricant.

Overall, it is obvious that the suggested modified Hersey numbers are not capable of capturing all of the complexities of an MR-lubricated bearing. This is not entirely unexpected, since fundamentally both variants use an average of the apparent viscosity throughout the fluid film volume. Such an average cannot be expected to account for the large effect that the (angular) location of the magnets has on the performance of the bearing (see figure 5.7). For example, placing the magnets at the location where the film is maximum will have a large effect on the average viscosity and therefore on the modified Hersey numbers compared to the unmagnetised situation, but at the same time the transition speed will likely be similar or the same for both cases (meaning that the modified Hersey numbers should not change either). Next to that, the figures presented in this section indicate that even when location remains the same, changes to the size or shape of the magnetised area may also have effects on the Hersey number that are not captured by a simple viscosity average. In spite of all of this, it is interesting to see that the modified Hersey numbers do cause a collapse when the magnetic field strength is scaled without changes in shape or location, leading to the question of whether this result will hold when such an experiment is repeated with the magnets in a completely different location. In the end it is clear that the entire concept of a modified Hersey number for MR lubrication requires further investigation (such as a classical dimensional analysis), but the findings from this section might prove useful as a starting point.

6

MR-lubricated rubber bearings

After the conclusion of the wear tests of MR-lubricated hydrodynamic journal bearings as described in chapter 4, two promising sleeve materials had been found. Polymer sleeves showed a 3 to 7 times increase in the volumetric wear of the shaft and sleeve compared to the reference test, but despite the increase in wear this still meant a massive improvement over the 2 orders of magnitude increase observed with bronze sleeves. The hydrodynamic performance of these polymer sleeves has been discussed in chapter 5. The other promising material was rubber, with the steel shaft used in combination with the rubber sleeves showing minimal wear, even less than the shaft in the reference test. The amount of wear of the sleeve could not be determined properly due to the elasticity of the rubber, but based solely on the (lack of) shaft wear, it was still thought to be interesting to experimentally investigate the hydrodynamic performance of this bearing material. Those results will be discussed in this chapter.

6.1 Introduction

The use of rubber to create hydrodynamic (journal) bearings is a relatively old concept, which has been explored and applied since early in the 20th century [1]. The main advantage of rubber as a bearing material is its low elastic modulus compared to other, stiffer materials such as metals or polymers. In a bearing application this will result in large, non-negligible deformations of the bearing surface, frequently of the order of magnitude of the nominal film thickness [146]. Specifically, the rubber will deform to accommodate to the shape of the shaft, creating a very efficient fluid film with lower peak pressures and therefore an improved load capacity compared to stiffer materials [147]. An additional advantage is that this allows the system to function properly even in the case of geometry errors or misalignment. For example, in real world applications misalignment of the shaft and bearing can be a serious problem [148], resulting in higher and asymmetric film temperatures, reduced load capacity, and increased wear [149–152]. With a rubber bearing, the rubber surface will simply deform on the edge where the shaft is closest to the bearing, resulting in a better distribution of the load over the surface and preventing the worst of the problems mentioned above [141] (although it should be noted that misalignment is to be avoided for rubber bearings as well, since it will still reduce the load capacity [146, 153]). Because of these properties, rubber bearings have been especially popular when water is used as a hydrodynamic lubricant [154]. Water is frequently used when environmental pollution due to lubricant leakages should be eliminated, such as in stern tube bearings used in the maritime industry or in water pumps [1, 155]. However, because of its extremely low viscosity compared to traditional lubricating oils, water is not actually a very good lubricant and even minor geometry errors or misalignment will lead to contact and a catastrophic increase in wear. Water-lubricated rubber bearings are therefore used frequently, although even with rubber some of the disadvantages of water lubrication will remain (such as low load capacity and extremely thin hydrodynamic films [141]).

An additional advantage of the elasticity of rubber bearings is their resistance to abrasive wear due to contaminants such as dirt or sand in the water. This is especially relevant for open lubrication systems that use water from the environment as their lubricant. Research has shown that hard contaminant particles in the water will be pressed elastically into the rubber by the shaft at low speeds (boundary or mixed lubrication regime), preventing the severe third body abrasion that would occur with harder bearing materials [125, 141]. It is for this reason that rubber bearings were included in the MR lubrication wear tests described in chapter 4. While SEM imaging revealed some surface damage on the rubber after the wear tests, it was not possible to measure the bearing wear volume due to elastic deformation of the rubber surface when using the contact-based profilometer. However, the shaft wear was found to be minimal. That fact, combined with the knowledge of the wear process of rubber bearings lubricated with contaminated water, led to a decision to experimentally investigate the hydrodynamic performance of a rubber bearing lubricated with MR fluid. This chapter will present those results, and will compare them with the results obtained in chapter 5 for the polymer bearing sleeve (which also showed acceptable wear behaviour).

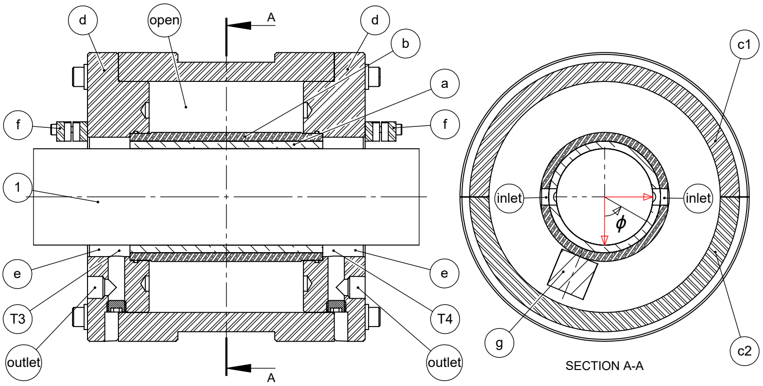

Figure 6.1: A section view of the bearing housing. 1 - shaft, a - rubber sleeve, b - non-magnetic steel outer sleeve, c1/c2/d - housing components, e - original location of seals, f - capacitive sensor clamps, g - magnets, T3-T4 - thermocouples. The lubricant inlets and outlets are marked as well. In the figure on the right, ϕ is defined as the angular coordinate inside the bearing. The shaft rotates in the positive ϕ direction, and for the magnetised tests the three magnets were placed at an angle of $\phi = -22.5°$.

6.2 Method

The hydrodynamic rubber bearing tests were executed on the test setup that was also used in chapters 2 and 5 for the tests with bronze and polymer sleeves respectively. Specifically, the rubber tests were intended to replicate the polymer Stribeck tests performed with and without magnetic field for three different loads, to allow for a comparison of the impact of these different materials on the hydrodynamic performance. The test setup and experimental procedure are therefore in principle the same as those described in section 5.2. Figure 6.1 shows a schematic overview of the bearing and bearing housing, with the most important components marked. Table 6.1 contains the main bearing properties and operating conditions, with the most important changes compared to the polymer bearing being a larger lubrication groove diameter and a larger tolerance on the nominal radial

Table 6.1: Overview of the bearing properties and operating conditions for the tests with a rubber sleeve.

Property	Symbol	Value
Bearing length / shaft diameter /	L/D	100mm/50mm
Nominal radial clearance	h_0	150-250µm
Shaft / bearing material		C45 steel/NBR rubber
Max. load / specific pressure	W_a/p_m	7.5kN/1.5MPa
Speed range	n	0 - 1500rpm
Lubricant		MR fluid MRHCCS4-A [119]
Lubricant flow rate	Q_{in}	$0.3\,\mathrm{L\,min^{-1}}$
Lubrication groove radius / length		3mm/100mm
Average inlet temperature		30-34°C
Average film temperature		36-40°C
Rubber hardness (shore-D)		70±3

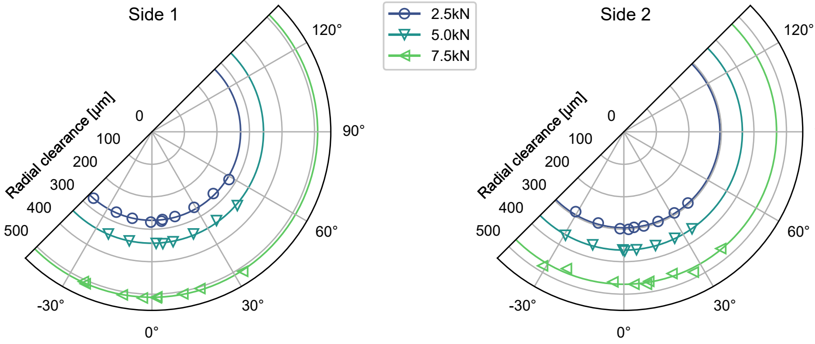

Figure 6.2: An example of the clearance circles measured with the rubber bearing sleeve for the three different loads that were tested. The circles shown in this figure were measured specifically for one of the tests without a magnetic field applied.

clearance. Both of these changes were needed because of the high costs associated with manufacturing rubber sleeves with tight tolerances and small features. Other than that, the same MR fluid was used (see section 5.2.3 for its properties) and the fluid was magnetised with the same magnetic field (see the $465\,\mathrm{kA\,m^{-1}}$ peak strength field in figure 5.6). However, the initial pilot tests did reveal some issues with the use of a rubber bearing in the test setup, requiring further changes. These will be discussed in the remainder of this section.

The main difference concerns the clearance circle and film thickness measurements using the capacitive distance sensors. Because of the very low elastic modulus of rubber, at least compared to bronze or polymer, the clearance circle diameter that is measured with the capacitive sensors scales with the applied load. For that reason this diameter will always be larger than the nominal clearance diameter given in table 6.1. During the measurements, it was therefore not surprising to find that the clearance circle diameters were larger than the 500µm range of the capacitive sensors, even at the lowest load of 2.5kN/0.5MPa, meaning it was not possible to measure the full 360° clearance circles. Instead, using the standard least-squares fitting procedure described at the end of section 2.2.4, they had to be inferred from points collected only near the bottom of the bearing. Figure 6.2 shows the clearance circles measured after a Stribeck test for the three tested loads (this figure can be compared with figure 5.10 on page 89, which shows the representative clearance circles for the polymer bearing). Because the number and location of the points used to fit the circles was limited, the accuracy of the clearance circle diameters and centre locations is possibly reduced compared to those measured for the stiffer bronze or polymer bearing sleeves. For example, cylindricity issues such as those caused by manufacturing errors or wear could lead to errors in the calculated clearance circles. A possible indication that this was indeed a problem could be the fact that the clearance circle measurements for repeated Stribeck tests sometimes (but not always) showed drastically different diameters, with seemingly random variations of up to ±50µm. This was never observed with the stiffer bronze and polymer bearings. However, while these variations will have an effect on the film thickness calculation, because the film thickness is determined by calculating the eccentricity of the shaft locus points with respect to the clearance circle centre, the resulting error will be much smaller than ±50μm. Since the points on the clearance circle were collected at the bottom of the bearing, near minimum film, the error on the calculated film thickness would only be that large if the shaft was ever at the top of the bearing, which should not happen during normal operation (and was indeed never observed).

Another issue related to the large degree of deformation of the rubber sleeve concerned the clearance in the contactless labyrinth seals, used to minimise leakage from the bearing housing. With a radial clearance of less than 440μm, the seals had to be removed to prevent the sealing rings from coming into contact and interfering with the operation of the hydrodynamic bearing. As shown in figure 6.1, this left two large holes (marked with 'e') at the sides of the bearing, right next to the outlet channels. Without the seals, the lubricant was no longer forced through the outlet channels, and mostly left the bearing through the larger holes instead. The flow rate of this leakage was found to depend on the speed of the shaft and on whether or not a magnetic field was applied (leading to fringe fields in the outlets), with lower speeds and a strong field (higher viscosity) leading to larger leakage flows. Since the capacitive sensors were placed only a few millimetres from these holes (the clamps holding the sensors are marked with 'f' in the figure), lubricant was found to frequently flow into the space between one or more of the capacitive sensors and their target, the rotating shaft. Capacitive distance sensors use the permittivity of air to calculate distance based on the measured capacitance, meaning that any contamination immediately invalidated the sensor readings. Furthermore, because the fluid did not always completely fill the space between sensor and shaft, it was not possible to correct for this by recalculating the distance with the permittivity of the lubricant either. In the end, this meant that the film thickness measurements could not be conducted successfully for all speeds of all Stribeck tests.

6.3 Results and discussion

Figure 6.3 shows the experimental Stribeck curves and minimum film thickness plots for the MR-lubricated rubber bearing, and for comparison figure 6.4 shows the same results for the polymer bearing (this is a modified variant of figure 5.9 which previously appeared in chapter 5). Comparing these two figures immediately shows some fundamental differences between the hydrodynamic performance of these two bearing materials. First of all, it should be noted that for repeated Stribeck tests under the same operating conditions, the film thickness measurements show more variance for the rubber bearing than for the polymer one (this variance is represented by the shaded areas surrounding the curves in the figure). This is likely the result of the clearance circle measurement issues discussed in the previous section, specifically the seemingly random variations on the calculated clearance circle diameters. Second, and more important, looking at the unmagnetised MR-lubricated rubber bearing shows that there is very little difference between the Stribeck curves for the three tested loads (figure 6.3a), with only the 7.5kN curve having a slightly larger overall friction coefficient. This is a result of the relatively low elastic modulus of the rubber, causing the rubber to deform in such a way that it accommodates to the shape of the shaft, reducing the peak pressure values and leading to an effective thin fluid film even at high loads and low speeds. As shown in figure 6.3c, the film thickness is fairly

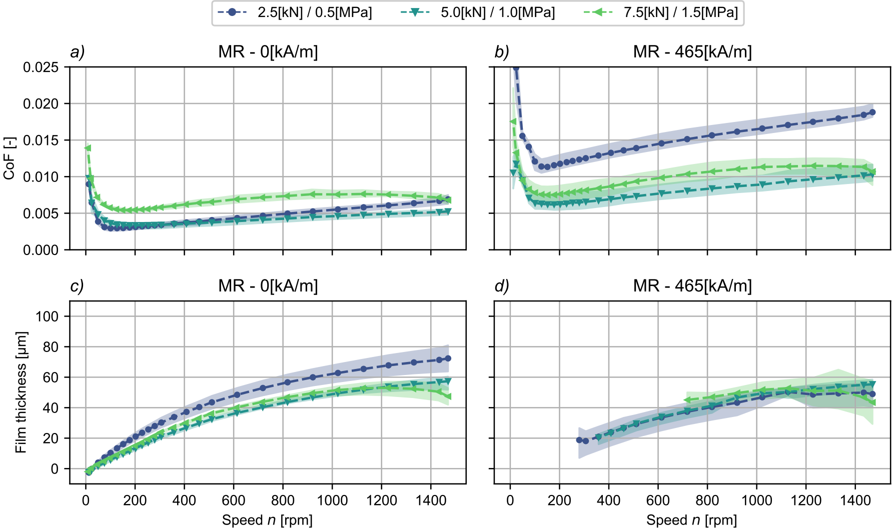

Figure 6.3: **Rubber bearing results** - Experimental Stribeck curves and minimum film thickness plots for the rubber bearing sleeve at three different loads. The dashed lines represent the average value over three repetitions of each test, the shaded regions indicate the minimum and maximum values that were measured over three repetitions. Tests were performed with MR lubrication with zero magnetic field (*a* & *c*) and MR lubrication with a strong magnetic field (*b* & *d*).

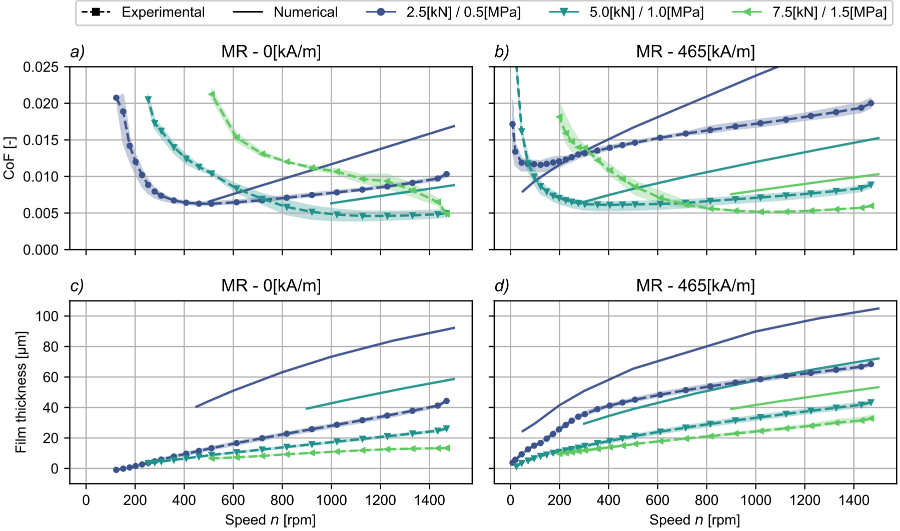

Figure 6.4: **Polymer bearing results** - Experimental (dashed lines with markers) and numerical (solid lines) Stribeck curves and minimum film thickness plots for the polymer bearing sleeve for three different loads. Tests were performed with MR lubrication with zero magnetic field (*a* & *c*) and MR lubrication with a strong magnetic field (*b* & *d*). This figure previously appeared in chapter 5 as figure 5.9, but note that the results for oil lubrication have been left out.

similar in all cases, with only a small reduction for the two higher loads. In contrast, the much stiffer polymer bearing (figures 6.4a and 6.4c) shows smaller film thicknesses and the expected variation with load when unmagnetised, with larger loads leading to thinner films and therefore to higher transition speeds, as well as lower friction coefficients. It should be noted that it is also because of these large deformations that the shear-thinning model from chapter 3 has not been applied to the rubber bearing, since the model cannot currently take deformations of the surfaces into account.

Surprisingly, very little changes when the magnetic field is applied to the rubber bearing, as shown in figures 6.3b and 6.3d. The Stribeck curves show the expected increase in friction coefficient but the transition speed is effectively unchanged, with the 2.5kN curve actually experiencing a small increase from 100 to 125rpm. At the same time the film thickness is reduced slightly for the higher loads and strongly for the lowest load, where it shows a reduction of more than 30% at 1500rpm (note that the film thickness for the magnetised bearing could only be measured at high speeds because of the leakage flow issue discussed in the previous section). The contrast with the magnetised polymer bearing is large (figures 6.4c and 6.4d), and the rubber bearing seems to show none of the improvements in transition speed and film thickness that were found when magnetising the stiffer bearing. However, the MR fluid itself still seems to function as expected, experiencing a viscosity increase due to the formation of particle structures when magnetised, which is implied by the fact that the friction coefficient does go up when a magnetic field is applied to the MR-lubricated rubber bearing. But in contrast to the stiffer polymer, this increase in viscosity does not translate to lower transition speeds or thicker films with the rubber. A reason for this could be the low elastic modulus of the rubber, with the rubber possibly being deformable enough to accommodate to the local change in viscosity at the location of the magnets, similar to how it accommodates to the shape of the shaft when the load is increased. For the magnetised MR bearing this could mean that any positive effects of a more efficient pressure profile due to the viscosity increase are cancelled out by local increases in film thickness due to deformation of the rubber. In fact, if this is indeed the case it seems that the positive effects of the MR viscosity increase are not simply cancelled out by the resulting deformation, but the combination of these effects actively worsens the performance of the bearing, since the activation of the magnetic field slightly reduces the minimum film thickness compared to the unmagnetised rubber bearing (compare figures 6.4c and 6.4d). Overall, if this hypothesis is indeed correct and the observed effects are caused by the low elastic modulus of the rubber, rubber journal bearing sleeves (or sleeves made out of equally deformable materials) would likely be fundamentally incompatible with MR lubrication if the aim is to change the friction or film thickness with a magnetic field.

Finally, an additional side note should be made regarding the validity of the film thickness measurements. The lack of a response to the activation of the magnetic field was shown by both the friction and film thickness measurements, in spite of the limitations of the clearance circle measurements for the rubber bearing that were described in section 6.2. However, next to those more practical issues, the existence of a more fundamental clearance circle problem caused by the deformable nature of rubber is suspected as well. With the experimental setup used during this research project, the clearance in the bearing is measured by pushing the shaft against the bearing at rest, with the assumption that the resulting position of the shaft has an eccentricity of 1. By repeating this measurement for a range of attitude angles, the full clearance circle can be constructed. It is then known that during hydrodynamic operation of the system, the shaft locus will always fall inside the clearance circle since the eccentricity of the shaft can never be larger than 1. This holds for bearings made from stiff materials where deformation can be neglected, but that may no longer be the case when deformation is not negligible. The reason for this is that the rubber bearing will be deformed by the generated hydrodynamic pressure profile while the system is operating in the hydrodynamic regime. But, this pressure profile will be different from the contact pressure profile when measuring the clearance circle at rest, even if the applied load is the same in both cases. This results in a difference between the actual deformation during hydrodynamic lubrication and the assumed deformation determined with the clearance circle measurement, leading to an error in the film thickness calculation. If it is assumed that the static contact pressures are higher, since the load is distributed over a smaller area than during hydrodynamic lubrication, the film thicknesses calculated for the rubber bearing would be an overestimation. In other words, in reality the rubber will deform less than assumed by the clearance circle, and the rubber surface will therefore be closer to the surface of the shaft. It is not known how large this effect could be, but the error is expected to be larger at higher speeds, where the hydrodynamic pressure profile differs the most from the contract pressure profile. In the end, these issues with the clearance circle method do not change the observations about MR lubrication in rubber journal bearings, since those conclusions are also supported by the friction measurements. However, they should be important considerations that require further investigation for future research that would consider applying this method to highly deformable bearings.

6.4 Conclusion

The choice was made to perform a set of Stribeck tests with an MR-lubricated rubber bearing sleeve because it was thought to have good wear qualities when used in combination with the abrasive MR particles. The results of these tests show that in general, the rubber bearing performs well and compares favourably with the polymer bearing due its low transition speed and low friction coefficient. The low elastic modulus of the rubber allows the bearing to accommodate to the shape of the shaft, thereby creating a very effective thin film. As a result, the performance of the rubber bearing is much less dependent on the applied load than the performance of the stiffer polymer bearing. However, this same property is suspected to be the cause of the minimal effect that applying a magnetic field has on the bearing, other than simply increasing the friction. While it is not possible to find the exact cause without a model and a more reliable film thickness measurement, the friction measurement on its own is enough to conclude that polymer is a more promising material to use in further investigations into MR-lubricated bearings with variable magnetic fields, irrespective of the wear performance of the rubber.

7

Discussion

This final chapter briefly summarises the individual discussions from the previous chapters, and expands on them by discussing their influence on the main objective of the dissertation. Multiple recommendations are made for possible future research directions.

The main objective of this dissertation was to investigate the use of MR fluid as a lubricant for hydrodynamic journal bearings, with the idea that this might lead to improvements in film thickness, transition speed, or hydrodynamic friction (or all of these) compared to traditional lubricating oils. Before the start of the research described in this dissertation, literature mostly contained articles showing how MR-lubricated bearings magnetised throughout the entire film would show thick films and high friction compared to unmagnetised MR or oil lubrication. In chapter 2 of this dissertation it was shown that this high friction could be reduced significantly by diluting the fluid and by locally magnetising the bearing. However, because the resulting viscosity increase was less strong and more localised, the increase in film thickness was reduced significantly as well. Contrary to the claim made in this chapter that ”the results that were obtained could not have been achieved with a standard commercial MR fluid” (implying that dilution and therefore a smaller number of particles was necessary for low friction MR bearings, see page 22), chapter 5 then showed that very similar results could be obtained with only local magnetisation and low field strength. In fact, by increasing the magnetic field strength the performance of the bearing could gradually be changed from low friction and thin films (similar to the performance of the bearing in chapter 2), to high friction and thick films (similar to the performance of most MR bearings presented in literature). These results provided a link between the results from chapter 2 and literature, and showed the effectiveness of local magnetisation. But, they also showed that it was not possible to obtain both lower hydrodynamic friction and a lower transition speed at the same time (compared to oil lubrication), which was initially thought to be a possibility with passive, localised magnetic fields (as described in section 1.2). It should be noted that these results were obtained for only a single configuration of the magnetic field, meaning that differently shaped magnetic fields could perhaps still have the hypothesised effect. However, it was also found that the transition to mixed lubrication actually occurred for thicker films with MR than with oil, almost irrespective of the applied magnetic field (see figure 7.1). For standard lubricants this should not be possible, since the film thickness at the transition point is known to depend solely on the roughness of the bearing surfaces. This led to the hypothesis that MR fluid particles might be getting stuck between the bearing surfaces when the film was thin, thereby causing the earlier and more gradual transition to mixed lubrication compared to the usual transition caused by contact of the surface roughness peaks[1]. If this is indeed the case, it seems like an inherent disadvantage of MR lubrication compared to lubrication using fluids without particles. It would mean that an unmagnetised MR-lubricated bearing would always transition earlier (at a higher film thickness) than a comparable oil-lubricated bearing, and activating the magnetic field to bring the transition speed in line would result in higher friction (exactly what was observed in section 5.3.2). Based on this reasoning, and on the relatively large influence this effect seems to have on the performance of the bearing close to the transition, passively magnetised MR bearings do not seem like a very effective option anymore if the goal is to lower both friction and transition speed, at least with the MR fluids/MR particles used for this dissertation.

However, despite the somewhat unexpected performance of passively magnetised MR bearings, it has still been confirmed that the performance characteristics of these bearings

---

[1] The effect of the particles could therefore be seen as an increase in the effective surface roughness.

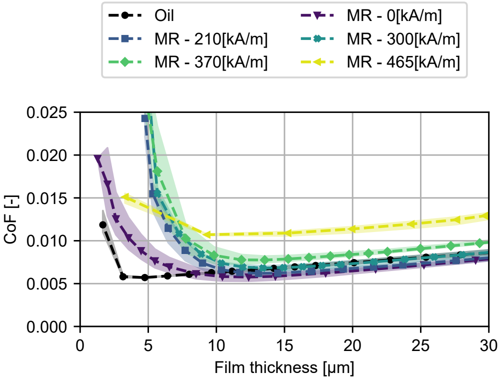

Figure 7.1: Friction coefficient as a function of film thickness for the experimental results of the oil- and MR-lubricated polymer journal bearing tests with varying magnetic field strength, these quantities were previously presented as a function of the shaft speed in figures 5.8a and c. It is clearly shown that the oil-lubricated bearing has a transition once the film thickness reaches 3 to 5μm, whereas the MR-lubricated bearings have this transition between 10 to 15μm. There is little dependence on the magnetic field strength, and similar results are found at higher loads. Note that this effect cannot be shown for the results from chapter 2 due to the significant wear damage of the bearing sleeve.

can be changed dramatically depending on the magnitude and location of the magnetic field. As described in the introduction, this ability to modify the viscosity of the fluid film still has the potential to be a large advantage of MR lubricants compared to standard lubricants, especially when considering active control of the magnetic field (which has not been investigated in this dissertation). The remainder of this discussion will touch on several aspects of lubricating with MR fluids that the author thinks require further investigation and development for the full potential of MR lubrication to be realised. These aspects concern the lubrication properties of the MR fluid, the modelling and optimisation of MR-lubricated bearings, and finally the active control of the magnetic field as a function of the operating conditions.

7.1 MR fluid as a lubricant

It is clear that MR fluids exhibit important differences compared to standard lubricating oils, both positive and negative, which is all the result of the iron microparticles suspended in the fluid. Their variable viscosity is the main attraction, but during the research performed for this dissertation it has also become apparent that the shear-thinning and wear characteristics of these fluids are important as well, and these mostly make MR fluids more difficult to work with compared to standard lubricating oils. While these characteristics may be partially inherent to a lubricant consisting of a suspension of particles, this section will suggest some possible research directions for improving the lubrication properties of MR fluids and MR-lubricated bearings.

At first glance, a shear-thinning lubricant seems to offer some advantage compared to a Newtonian lubricant. Because of shear-thinning, the viscosity of the lubricant will be higher at lower speeds (i.e. close to the transition speed) which is exactly when high viscosity is useful for creating thick films to postpone the transition to mixed lubrication.

However, shear rates are also higher at high loads which means that unlike a Newtonian lubricant, a shear-thinning lubricant performs worse when the load on the bearing is increased. As documented in chapter 5 this is even more problematic for MR lubrication, since here the degree of shear-thinning is also proportional to the strength of the magnetic field. While it may be possible to compensate for this effect by actively increasing the size or strength of the magnetic field as a function of the applied load, this is an additional complication in the implementation of MR-lubricated bearings that is not present when using Newtonian lubricants. At higher loads this may be a necessity however, since shear-thinning is likely a fundamental property of MR fluids because it is mostly caused by the gradual breakdown of the magnetised particle structures at higher shear rates [12].

The particles are not the only source of MR fluid shear-thinning however. Due to the use of thixotropic additives intended to prevent sedimentation of the particles, most (if not all) commercial MR fluids are shear-thinning even when not magnetised and when no particle structures are present. This mainly affects the lubrication system of the bearing where the shear rates are much lower than in the hydrodynamic bearing itself, making MR fluids significantly more viscous than standard lubricating oils while ouside the bearing. As a result, lubricant supply and drain lines may have to be pressurised, since a purely gravitational system may not achieve sufficiently high lubricant flow rates. These higher pressures could also cause larger leakage flows through the seals. Fortunately, there are other methods of reducing particle sedimentation rates in MR fluids, which may be capable of minimising the amount of shear-thinning in the unmagnetised fluid. A relatively simple way of preventing sedimentation would be some form of active agitation, for example by stirring the lubricant inside the lubricant supply tank. While this method can be very effective [156], it does nothing to prevent sedimentation while the MR fluid is being stored (for example in a warehouse), which is an important consideration for real world use of these fluids and may mean that additional passive anti-sedimentation measures are required as well [14]. Various effective passive methods have been investigated in literature, such as the use of coatings on the particles to reduce their density, the use of non-spherical particles (such as rods or flakes), or the use of smaller iron nanoparticles [13–15], though it should be noted that all of these measures can lead to modifications of the magnitude of the MR viscosity change or the wear behaviour of the fluid.

Especially when considering both sedimentation and wear, the use of nanoparticles seems like it could potentially be a very interesting research direction. While it is known that the magnitude of the viscosity change decreases when the particle size is reduced [11], it has been shown in literature that even a magnetic fluid containing only 3.8 vol% 12.5nm iron particles can still produce a roughly one order of magnitude increase in viscosity with a magnetic field strength of $160\,\mathrm{kA\,m^{-1}}$ and a shear rate of $1000\,\mathrm{s^{-1}}$ [9]. Compare this to the MR fluid used in chapter 5, which contains roughly 20 vol% iron particles with an average diameter of 2µm, which produces slightly less than 2 orders of magnitude increase in viscosity for a $145\,\mathrm{kA\,m^{-1}}$ magnetic field and the same shear rate (see figure 5.3). Furthermore, due to the small size of the nanoparticles this magnetic fluid was completely stable against sedimentation, without the use of any thixotropic additives (although the fluid was still shear-thinning when magnetised due to the presence of the particle structures). Next to this it is known that ferrofluids, which generally use particles of around 1 to 10nm but do not show significant changes in rheology for variations in the magnetic field[2], have very good wear performance, sometimes even better than standard lubricating oils [116, 158, 159]. In comparison, chapter 4 showed that the wear with MR lubrication was only acceptable when using softer polymer bearing sleeves, and even then the amount of wear was still about 4 times larger than with a standard lubricating oil. Research on bearings lubricated with contaminated water pointed to rubber bearings for even lower wear, but the hydrodynamic performance of these bearings was found to be independent from the magnetic field strength when lubricated with MR fluid in chapter 6. The use of smaller magnetisable particles may therefore be the most promising method for reducing wear even further. The main disadvantage of using nanoparticles is that iron particles generally get more expensive the smaller they are, making nanoparticle-based magnetic fluids more expensive than standard MR fluids (which are already much more expensive than standard lubricants). Still, the potential benefits seem promising enough to merit further investigation into the particle size (between 10nm and 1µm) that would lead to an MR fluid with a good balance between the magnitude of the magnetic viscosity increase, the sedimentation rate, the wear rate of the lubricated surfaces, and the cost.

7.2 Modelling MR lubrication

The main goal during the development of the model was to obtain relatively short solution times to enable fast, large scale optimisation studies. Considering the lack of literature about the optimal magnitude and shape of magnetic fields used to activate MR-lubricated bearings, numerical optimisation was thought of as an efficient way to discover promising magnetic fields that could subsequently be evaluated experimentally. Furthermore, it was thought that faster models could aid an eventual propagation of MR bearings to industrial applications, with fast models enabling designers to easily find efficient bearing designs for various operating conditions. For these reasons, the model was based on the Reynolds equation instead of the much more computationally complex Navier-Stokes equations. However, the shear-thinning effects described in the previous section, in combination with the effects of the magnetic field, made the modelling of MR lubrication significantly more complicated than the modelling of the standard (Newtonian) lubricant. While the initial Newtonian model described in chapter 2 managed to provide a reasonable indication of the trends in the performance of the MR bearing, the fact that this result required the selection of a constant viscosity value to represent the entire shear-thinning fluid film was far from ideal. Especially since this value was determined at the (completely unrelated) maximum shear rate that could be achieved in the rheometer; the Herschel-Bulkley viscosity model had not yet been developed to allow extrapolation to higher shear rates, nor was there a way to determine which shear rate value would have been more suitable in the first place. In that regard the shear-thinning model developed in chapter 3 was a large improvement, with the addendum of chapter 2 showing that this model had improved accuracy over the Newtonian model. The model was also used in chapter 5, though the differences between the experimental and numerical results were relatively large in that case. As discussed in that chapter, these differences were likely caused by the poor quality of the experimental temperature data, and possibly by the lack of high shear MR viscosity data to verify the accuracy of the Herschel-Bulkley extrapolation with. Because the accuracy of the shear-

---

[2] See Odenbach [157] for the differences between ferrofluids and MR fluids with nanoparticles

thinning models has already been discussed in these previous chapters, the remainder of this section will instead focus on the suitability of the shear-thinning model for fast optimisation, and possible directions for further research.

In chapter 3 it was shown that the analytical method for the evaluation of the flow factor integrals in the generalised Reynolds equation resulted in an approximately 50% reduction of the solution time, without any loss in accuracy. While this was a good result, the speedup was not large enough to bring the shear-thinning model (which takes minutes to solve) to the level of the standard Reynolds equation (which takes seconds to solve). This is partially inevitable, the shear-thinning problem is simply more complicated due to the non-linear viscosity, resulting in a denser Jacobian. The problem also solves for a larger number of unknowns because the current implementation required solving for the flow factor integrals explicitly for proper convergence, though it is possible that other ways of implementing this problem do not require such a step. Furthermore, the sub-optimal implementation of the Appell hypergeometric function could also be improved which might lead to a faster solution time. The Appell function appears in the analytical solution of the flow factors, and is a complicated mathematical function defined by an infinite series that has not yet been implemented in a fast and robust manner in any programming language[3]. There is one relatively old Fortran implementation of the Appell function in literature [83, 161], but this implementation was found to fail for certain combinations of input arguments that are relevant for the shear-thinning problem. For this reason lookup tables were used to approximate this function, but while these are relatively fast a native implementation is expected to be faster and easier to use (since the lookup tables require communication between Matlab and COMSOL). Furthermore, due to the use of lookup tables the derivatives of the Appell function were not available, and the flow factors had to be excluded from the Jacobian matrix. It is possible that the model would be faster with access to these derivatives, since a more accurate Jacobian generally means that fewer solver iterations are needed, but the increased amount of data in the Jacobian and the larger amount of time to compute it mean that a speedup is not guaranteed. While it would technically have been possible to create lookup tables for the derivatives as well, this was complicated by the fact that the partial derivatives of the Appell function AppellF1$(\alpha,\beta,\beta',\gamma,x',y')$ are generally only presented for x' and y' in literature (α, β, β' and γ are usually constants). The other partial derivatives do exist but only in the form of infinite series [162], not in the simple integral form used to create the lookup tables. These series could quite possibly be transformed to a simple integral form as well though some mathematical procedure, but as far as the author could find this has not yet been done in literature for these specific series.

The lack of derivatives is especially problematic when using the shear-thinning model for optimisation. While section 5.3.1 presents the results of an optimisation process, this was a simple 1D optimisation where the position of a set of magnets with fixed size and strength was varied in only one direction, which is quite easily done with a gradient-free optimiser. It would however be much more interesting to optimise for the ideal values of the magnetic field strength at all places throughout the entire (2D) fluid film, as a function of the operating conditions. In principle this optimisation could be done with a gradient-

---

[3] Matlab has a interesting article about the complex process of properly implementing these types of functions in computer code [160]

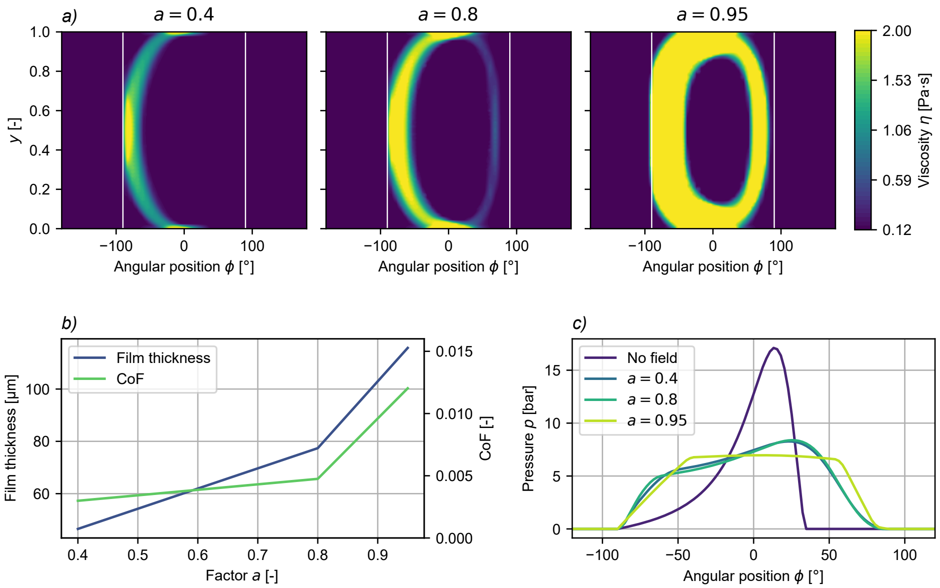

Figure 7.2: a) Optimised Newtonian viscosity profiles for three different values of the factor a, with low a corresponding to a focus on minimising friction, and high a to a focus on maximising film thickness. The vertical white lines at −90° and 90° indicate the inlets. b) The trends in film thickness and friction coefficient as a function of the factor a. c) The corresponding pressure profiles at the bearing centreline.

free optimiser since it is technically a 'simple' optimisation of n variables, where each variable is the magnetic field strength at one of the nodes/integration points of the mesh elements. The problem is of course that n would be extremely large, as an example the simulations in chapter 5 use 10 000 mesh elements with cubic shape functions. COMSOL does not even allow gradient-free optimisation of variables that vary throughout the problem geometry, and if it did it would probably be a very slow optimisation. As a result, a gradient-based optimiser is preferred for the proposed optimisation, and the derivatives of the Appell function are therefore required (numerical differentiation would be extremely slow as well, and therefore not a solution). However, even with the derivatives known it is still possible that the non-linear shear-thinning model would require an extremely long time for optimisation of the magnetic field strength, simply because of the computational complexity of the problem.

An alternative could therefore be to optimise the viscosity of the fluid film directly, using a Newtonian model. This optimisation is guaranteed to be much faster, and while the disadvantages of the Newtonian model are known, it was found in chapter 5 that the results of the 1D magnet location optimisation were qualitatively similar between the Newtonian and shear-thinning models, even when the constant shear rate value in the Newtonian model was varied. To illustrate this idea, and the typical results it can produce, a simple optimisation has been performed. Basically, this optimisation uses the same operating conditions as were used for the 1D optimisation of the magnet angle (see section 5.3.1 for more details), with the only differences being the specifics of the optimiser, and the use of the Newtonian viscosity model (as described in chapter 2). The optimiser is allowed to vary the viscosity between its values at magnetic fields strengths of 0 and $370\,\mathrm{kA\,m^{-1}}$ (the peak field strength in the 1D simulation) for a constant shear rate of $1 \times 10^4\,\mathrm{s^{-1}}$. This means the fluid film viscosity can be varied between 0.12 and 2.0Pa s. The optimisation objective is the minimisation of the sum of the eccentricity ε and friction coefficient f_w (normalised with their values without any magnetic field, ε_0 and $f_{w,0}$ respectively), with a factor a that was varied between 0 and 1 determining the relative importance (see equation 7.1).

$$\begin{aligned} \text{given} \quad & \eta \in \mathbb{R} \\ \text{minimise} \quad & f(\eta) = \left(a \cdot \frac{\varepsilon}{\varepsilon_0} + (1-a) \frac{f_w}{f_{w,0}} \right) \\ \text{with} \quad & 0.12 \leq \eta \leq 2.0 \end{aligned} \tag{7.1}$$

Figure 7.2a shows the resulting optimal Newtonian viscosity profiles for three different values of a, figure 7.2b shows the corresponding film thickness and friction coefficient values, and figure 7.2c shows the pressure profiles at the centreline. As can be seen in the figures, for $a = 0.4$ there is relatively little change in the viscosity, with the objective being skewed towards minimal friction. Changing to $a = 0.8$ results in a larger difference and the resulting viscosity profile, with a curved line of high viscosity lubricant upstream from minimum film, is actually somewhat similar to the profiles created by the axial rows of magnets tested in chapter 5. Finally, with $a = 0.95$ the optimiser mostly focuses on minimising eccentricity (equivalent to maximising film thickness) and the viscosity profile seems to form some sort of pocket. A similar concept of an MR-lubricated journal bearing with pocket-like magnetisation has previously been explored numerically in literature [46]. Figure 7.2c shows that the optimised viscosity profiles actually have lower peak pressure, but offer increased load capacity because the pressure profiles cover a larger area of the lubricating film. Something similar was observed with the 1D optimisation, see figure 5.7.

In the end, it should be repeated that these results were obtained with a Newtonian model and can therefore at most give a qualitative prediction that should always be checked with the shear-thinning model. The Newtonian optimisation model is fast however, solving in only few minutes, and could possibly be used to construct better initial guesses for an eventual (slower) shear-thinning optimisation process. It is still recommended to further investigate the use of that model for optimisation, not only because of its increased accuracy, but also because an optimal magnetic field can be adapted for a direct implementation in the real world, whereas an optimal viscosity profile could only ever act as a guide for the creation of the magnetic field. However, until that time the Newtonian model could perhaps be used to inspire magnetic field configurations to validate experimentally.

7.3 Active vs passive control of the magnetic field

As was already mentioned in the first paragraph of this discussion, the experiments performed in this dissertation with constant/passive magnetic fields have shown that for the chosen bearing geometry, MR fluid, and operating conditions, the MR-lubricated bearing could not achieve both lower hydrodynamic friction and a lower transition speed compared to the oil-lubricated bearing. Based on these experiments, there does not seem to be any advantage in using passively magnetised MR lubrication over Newtonian lubricants

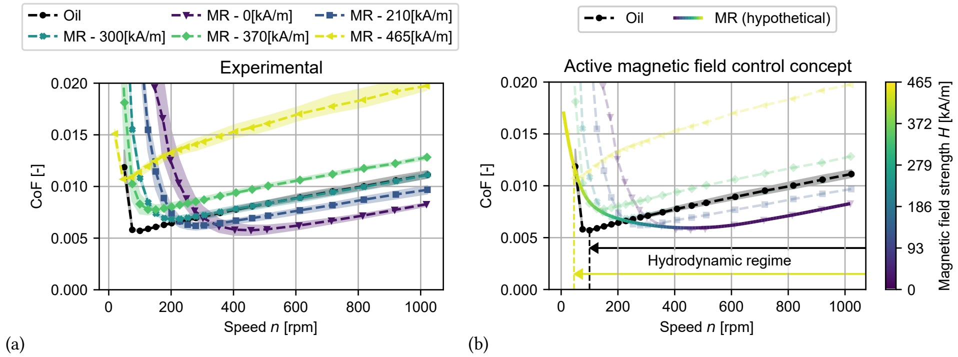

Figure 7.3: a) The experimental Stribeck curves for the polymer bearing lubricated with oil and MR fluid with varying magnetic field strength. The data in this figure previously appeared in chapter 5 as figure 5.8a. b) A hypothetical Stribeck curve considering active control of the magnetic field strength as a function of the speed of the shaft. The colour of the hypothetical Stribeck curve indicates the strength of the magnetic field at that speed. This hypothetical curve is based on the experimental results for MR lubrication from figure a), the outlines of those Stribeck curves are shown in the background of this figure. The experimental result for oil lubrication is shown as well, and for this result and the hypothetical curve it is indicated for which speeds the bearing would be in the hydrodynamic regime.

that are simply more or less viscous. However, this may change when considering the use of controllable magnets, such as electromagnets, to actively control the viscosity of the fluid film as a function of the operating conditions, something that would obviously never be possible with standard lubricants. Figure 7.3a shows the experimental MR Stribeck curves as a function of the (constant) magnetic field strength in the fluid film, these are results from chapter 5. While the MR bearing is not unambiguously better than the oil bearing for any one field strength value, it does have lower high-speed friction when unmagnetised (purple line, MR - 0[kA/m]) and a lower transition speed when strongly magnetised (yellow line, MR - 465[kA/m]). Therefore, instead of using a passive magnetic field that magnetises the fluid film in the same way at all speeds, it seems much more useful to instead only magnetise the film when the bearing would otherwise enter the mixed or boundary lubrication regimes, thereby minimising friction at all speeds. As a hypothetical example, figure 7.3b shows the hypothetical MR Stribeck curve that could likely be obtained by changing the strength of the magnetic field as a function of the speed of the shaft (creating a feedforward system). With this concept the magnetic field is turned off at high speed to minimise friction and it is not activated until the speed dips below around 500rpm, which is when the unmagnetised MR bearing would start transitioning to mixed lubrication. Below that speed the magnetic field strength is gradually increased in such a way that the film thickness is always just large enough to prevent mechanical contact between the bearing surfaces (with the presence of the particles taken into account as well), thereby keeping the bearing in the hydrodynamic regime and simultaneously minimising friction. It is not until the strongest (experimentally tested) magnetic field strength value of $465 \mathrm{kA\,m^{-1}}$ is reached that this hypothetical bearing would finally transition to mixed lubrication. The final Stribeck curve looks very similar to a traditional Stribeck curve, though it is interesting to note that the friction actually starts increasing (when reducing the speed) before the bearing transitions into mixed lubrication, which does not happen in a normal journal bearing. This is of course the result of the magnetically induced viscosity increase of the fluid film, making this Stribeck curve subtly different from the traditional ones.

Looking at this hypothetical Stribeck curve as a whole shows that an actively controlled MR bearing would likely be a lot more competitive with oil lubrication than the experimentally tested passive variants. With a lower transition speed (which could probably be lowered somewhat further with even stronger fields) and significantly lower high-speed friction, it seems that only the higher friction between 200 and 50rpm is not in favour of the MR bearing. However, the Stribeck curve does not tell the entire story, even in the best case scenario the wear rates for the MR-lubricated bearing are higher than the wear rates for oil once the system reaches boundary lubrication, as was mentioned in section 7.1 (and shown in chapter 4). This means that the magnitude of the transition speed decrease and the resulting reduction of the amount of time the bearing spends in the boundary lubrication regime will determine whether the final wear rate goes up or down. Finding ways of reducing the wear rates of MR-lubricated bearings even further would therefore make them more widely applicable, once again emphasising the importance of further research into for example the alternative fluid formulations proposed earlier in this discussion (see section 7.1).

That leaves the question of whether an actively controlled MR bearing could actually perform like the hypothetical example in figure 7.3b. In other words, is the proposed concept in any way realistic? While this can only be proven definitively by testing the concept experimentally, the author thinks there is a very high likelihood that it is indeed possible to create an actively controlled MR bearing with performance similar to that shown by the hypothetical Stribeck curve. First of all, the hypothetical curve was drawn based on the experiments with passive magnetisation, meaning that at the very least a quasi-static approach (slowly changing the magnetic field and speed) is very likely to work. Second, there is actually a single article in literature that describes the implementation of an actively controlled MR thrust bearing where closed loop control was successfully used to keep the film thickness constant when the load was changed [45]. For these reasons, not only feedforward, but even feedback control of an MR journal bearing seems like a very promising direction for future research. In fact, the main challenges with active control may actually be of a more practical nature. Electromagnets typically require more space to produce the same magnetic field strength as a permanent magnet, as well as requiring a constant supply of power and constantly generating heat. This heat could leak into the fluid film, deteriorating bearing performance, and a constant power draw may not be desirable for critical systems that should keep working in case of a power failure. Furthermore, the power required to activate the electromagnet could possibly even cancel out or exceed the power savings made by reducing friction in the bearing. Because of this, the use of standard electromagnets may not be optimal, but there could be alternatives. Switchable permanent magnets only consume power when the magnetic field is changed, but have the disadvantage of only allowing two states (magnetic field on or off) [163]. This could perhaps work for very simple feedforward control, where these two states correspond to low friction (off), or thick films (on), but it is much less flexible than an electromagnet and would probably only be suitable for quasi-static changes. Another option could be the use of tuneable magnets, which are electromagnets that use a low coercivity permanent magnet as a core. By changing the current through the electromagnet the magnetisation of the permanent magnet changes as well, with the advantage that the permanent magnet will remain magnetised when the electromagnet is turned off [164, 165]. Similar to switchable magnets, tuneable magnets therefore consume power only when their magnetisation is changed, and they generate very little heat. These magnets seem like a potential solution to the problems of general electromagnets, and it is recommended to investigate their use when looking into the active control of MR-lubricated bearings.

Overall, actively controlled MR-lubricated bearings seem like the most promising next step for research into MR lubrication. The ability to modify fluid film viscosity depending on the operating conditions can simply not be obtained with traditional lubricants, and based on the experiments with passive magnetisation it is deemed likely that active control could result in improved performance.

7.4 Recommendations

In summary, this dissertation has made several advances in the field of MR lubrication for hydrodynamic journal bearings, but it has also raised new questions that require an answer if MR bearings are to be a viable alternative for existing oil-lubricated bearings. Based on the findings of the research, the following recommendations have been made:

- Design a magnetorheometer capable of measuring MR viscosity at the high shear rates typical for journal bearings.
- Continue development of numerical (shear-thinning) models, especially for use in optimisation studies of the magnetic field.
- Research additional methods for reducing wear caused by the particles in the MR fluid, for example by modifying the fluid composition.
- Investigate active control of the magnetic field as a function of the operating conditions of the MR bearing.

8

Conclusion

In this final chapter, the main conclusions of the research project are given.

Magnetorheological (MR) fluids are not traditionally known for their qualities as lubricants in hydrodynamic bearings, but their unique magnetically adjustable rheology is what raised interest in the potential of using them for this application. MR lubrication has been explored in literature previously, but almost all of these investigations focused on fully and strongly magnetised fluid films with high viscosity, resulting in bearings with thick films but also high friction. Proof for the existence of low friction MR bearings was not found anywhere, even though lower friction and therefore higher efficiency is generally desirable in the real world. For these reasons, the main objective of this dissertation was stated to be the experimental and numerical investigation into the use of MR lubricants in journal bearings with the aim of improving bearing performance, with high performance bearings having thick films (at low speeds) and low friction.

Following the proposed research approach it was shown in chapter 2 that the friction increase of an MR bearing due to the activation of the magnetic field could indeed be minimised (to about a 14% increase at high speed) without losing the low speed film thickness increase, but the investigation was hampered by the high wear rates of the bearing. In chapter 4 this was shown to be the result of abrasive wear caused by the particles in the MR fluid, and softer polymer bearing sleeves were found to be an acceptable replacement for the standard bronze. Even more soft rubber sleeves were thought to be promising as well, but these were found to be unsuitable for use with MR lubrication in chapter 6. Simultaneously, a new numerical method for modelling shear-thinning lubricants (such as MR fluids) was implemented as described in chapter 3, and it was found to be 50% faster than existing methods. With this model, a simple optimisation of the magnetic field was calculated, and together with the other findings this led to a comprehensive experimental investigation of MR lubrication for a variety of operating conditions in chapter 5. Here it was shown that while the behaviour of the MR bearing could be varied from low high-speed friction and thinner films, to high friction and thick films by increasing the magnetic field strength, it was not possible to achieve both low friction (at high speeds) and thicker films (at low speeds) simultaneously. Based on these results, it was concluded that passively magnetised MR bearings did not provide significant advantages in friction, film thickness, or wear, compared to regular oil-lubricated bearings. However, the results with passive magnetisation do strongly indicate that active magnetisation, where the magnetic field is changed as a function of the operating conditions of the bearing, has the potential to achieve both low high-speed friction and thick low-speed films in the same bearing, making this a very interesting topic for further research.

Bibliography

Bibliography

[1] R. L. Orndorff Jr, “Water-Lubricated Rubber Bearings, History and New Developments,” *Naval Engineers Journal*, vol. 97, no. 7, pp. 39–52, 1985. _eprint: https://onlinelibrary.wiley.com/doi/pdf/10.1111/j.1559-3584.1985.tb01877.x.

[2] A. Dhanola and H. C. Garg, “Tribological challenges and advancements in wind turbine bearings: A review,” *Engineering Failure Analysis*, vol. 118, p. 104885, Dec. 2020.

[3] G. W. Stachowiak and A. W. Batchelor, *Engineering tribology*, vol. 9780521609. Butterworth-Heinemann, 2005.

[4] R. Stribeck, “Die wesentlichen eigenschaften der gleit- und rollenlager,” *Zeitschrift des Vereines Deutscher Ingenieure*, vol. 36, pp. 1341–1348, 1902.

[5] G. Bossis, O. Volkova, S. Lacis, and A. Meunier, “Magnetorheology: Fluids, Structures and Rheology,” in *Ferrofluids: Magnetically Controllable Fluids and Their Applications* (S. Odenbach, ed.), pp. 202–230, Berlin, Heidelberg: Springer Berlin Heidelberg, 2002.

[6] J. de Vicente, D. J. Klingenberg, and R. Hidalgo-Alvarez, “Magnetorheological fluids: A review,” *Soft Matter*, vol. 7, no. 8, pp. 3701–3710, 2011.

[7] S. Genc and B. Derin, “Synthesis and rheology of ferrofluids: A review,” *Current Opinion in Chemical Engineering*, vol. 3, pp. 118–124, 2014. Publisher: Elsevier Ltd.

[8] S. Odenbach, “Ferrofluids and their applications,” *MRS Bulletin*, vol. 38, no. 11, pp. 921–924, 2013.

[9] L. J. Felicia and J. Philip, “Probing of Field-Induced Structures and Tunable Rheological Properties of Surfactant Capped Magnetically Polarizable Nanofluids,” *Langmuir*, vol. 29, pp. 110–120, Jan. 2013. Publisher: American Chemical Society.

[10] S. Lampaert, *Magnetic fluid bearings & seals*. PhD thesis, Delft University of Technology, 2020.

[11] A. Ghaffari, S. H. Hashemabadi, and M. Ashtiani, “A review on the simulation and modeling of magnetorheological fluids,” *Journal of Intelligent Material Systems and Structures*, vol. 26, no. 8, pp. 881–904, 2015.

[12] S. Odenbach and H. Störk, “Shear dependence of field-induced contributions to the viscosity of magnetic fluids at low shear rates,” *Journal of Magnetism and Magnetic Materials*, vol. 183, no. 1-2, pp. 188–194, 1998.

[13] M. Ashtiani, S. H. Hashemabadi, and A. Ghaffari, "A review on the magnetorheological fluid preparation and stabilization," *Journal of Magnetism and Magnetic Materials*, vol. 374, pp. 711–715, 2015.

[14] S.-B. Choi, "Sedimentation Stability of Magnetorheological Fluids: The State of the Art and Challenging Issues," *Micromachines*, vol. 13, p. 1904, Nov. 2022. Number: 11 Publisher: Multidisciplinary Digital Publishing Institute.

[15] S. Kumar, R. Sehgal, M. F. Wani, and M. D. Sharma, "Stabilization and tribological properties of magnetorheological (MR) fluids: A review," *Journal of Magnetism and Magnetic Materials*, vol. 538, p. 168295, nov 2021.

[16] G. Yang, J. Pan, and D. Wang, "A review on the magnetorheological materials and applications," *International Journal of Applied Electromagnetics and Mechanics*, vol. 75, pp. 407–443, Aug. 2024. Publisher: SAGE Publications.

[17] X. Zhu, X. Jing, and L. Cheng, "Magnetorheological fluid dampers: A review on structure design and analysis," *Journal of Intelligent Material Systems and Structures*, vol. 23, no. 8, pp. 839–873, 2012.

[18] D. Patrascu, "How magnetorheological suspension works," *autoevolution.com*, 2009. `https://www.autoevolution.com/news/how-magnetorheological-suspension-works-8947.html`. retrieved on 06-03-2025.

[19] R. Ahamed, S.-B. Choi, and M. M. Ferdaus, "A state of art on magneto-rheological materials and their potential applications," *Journal of Intelligent Material Systems and Structures*, vol. 29, pp. 2051–2095, June 2018. Publisher: SAGE Publications Ltd STM.

[20] A. K. Bhat, N. Vaz, Y. Kumar, R. D'Silva, P. Kumar, and K. G. Binu, "Comparative study of journal bearing performance with ferrofluid and MR fluid as lubricant," *AIP Conference Proceedings*, vol. 2080, mar 2019.

[21] D. A. Bompos and P. G. Nikolakopoulos, "CFD simulation of magnetorheological fluid journal bearings," *Simulation Modelling Practice and Theory*, vol. 19, no. 4, pp. 1035–1060, 2011.

[22] C. A. Laukiavich, M. J. Braun, and A. J. Chandy, "A comparison between the performance of ferro- and magnetorheological fluids in a hydrodynamic bearing," *Proceedings of the Institution of Mechanical Engineers, Part J: Journal of Engineering Tribology*, vol. 228, pp. 649–666, feb 2014.

[23] K. Sahu and S. C. Sharma, "A Simulation Study on the Behavior of Magnetorheological Fluid on Herringbone-Grooved Hybrid Slot-Entry Bearing," *Tribology Transactions*, vol. 62, pp. 1099–1118, Nov. 2019. Publisher: Taylor and Francis Inc.

[24] S. A. Vaziri, M. Norouzi, P. Akbarzadeh, M. Kim, and K. C. Kim, "Numerical analysis of conical hydrodynamic bearing lubricated with magnetorheological fluid," *Journal of the Brazilian Society of Mechanical Sciences and Engineering*, vol. 46, p. 67, Jan. 2024.

[25] D. A. Bompos and P. G. Nikolakopoulos, “Experimental and Analytical Investigations of Dynamic Characteristics of Magnetorheological and Nanomagnetorheological Fluid Film Journal Bearing,” *Journal of Vibration and Acoustics, Transactions of the ASME*, vol. 138, jun 2016.

[26] J. Hesselbach and C. Abel-Keilhack, “Active hydrostatic bearing with magnetorheological fluid,” *Journal of Applied Physics*, vol. 93, no. 10 3, pp. 8441–8443, 2003.

[27] H. Urreta, Z. Leicht, A. Sanchez, A. Agirre, P. Kuzhir, and G. Magnac, “Hydrodynamic bearing lubricated with magnetic fluids,” *Journal of Intelligent Material Systems and Structures*, vol. 21, pp. 1491–1499, dec 2010.

[28] N. Vaz, K. G. Binu, P. Serrao, M. P. Hemanth, J. Jacob, N. Roy, and E. Dias, “Experimental Investigation of Frictional Force in a Hydrodynamic Journal Bearing Lubricated with Magnetorheological Fluid,” *Journal of Mechanical Engineering and Automation*, vol. 7, no. 5, pp. 131–134, 2017.

[29] X. Wang, H. Li, and G. Meng, “Rotordynamic coefficients of a controllable magnetorheological fluid lubricated floating ring bearing,” *Tribology International*, vol. 114, pp. 1–14, Oct. 2017.

[30] F. Quinci, W. Litwin, M. Wodtke, and R. van den Nieuwendijk, “A comparative performance assessment of a hydrodynamic journal bearing lubricated with oil and magnetorheological fluid,” *Tribology International*, vol. 162, no. April, p. 107143, 2021.

[31] A. van Beek, *Advanced engineering design lifetime performance and reliability.* TU Delft, 2010.

[32] W. Rowe, *Hydrostatic, Aerostatic and Hybrid Bearing Design.* Butterworth-Heinemann, 2013.

[33] C. Gachot, A. Rosenkranz, S. M. Hsu, and H. L. Costa, “A critical assessment of surface texturing for friction and wear improvement,” *Wear*, vol. 372-373, pp. 21–41, 2017.

[34] D. Gropper, L. Wang, and T. J. Harvey, “Hydrodynamic lubrication of textured surfaces: A review of modeling techniques and key findings,” *Tribology International*, vol. 94, pp. 509–529, 2016.

[35] M. Michalec, P. Svoboda, I. Krupka, and M. Hartl, “Tribological behaviour of smart fluids influenced by magnetic and electric field – A review,” *Tribology in Industry*, vol. 40, pp. 515–528, dec 2018.

[36] M. Zubieta, S. Eceolaza, M. J. Elejabarrieta, and M. M. Bou-Ali, “Magnetorheological fluids: Characterization and modeling of magnetization,” *Smart Materials and Structures*, vol. 18, no. 9, 2009.

[37] A. C. Becnel, W. Hu, and N. M. Wereley, “Measurement of magnetorheological fluid properties at shear rates of up to 25000 s -1,” *IEEE Transactions on Magnetics*, vol. 48, no. 11, pp. 3525–3528, 2012.

[38] A. Farjoud, N. Vahdati, and Y. F. Fah, “Mathematical model of drum-type MR brakes using herschel-bulkley shear model,” *Journal of Intelligent Material Systems and Structures*, vol. 19, no. 5, pp. 565–572, 2008.

[39] K. P. Gertzos, P. G. Nikolakopoulos, and C. A. Papadopoulos, “CFD analysis of journal bearing hydrodynamic lubrication by Bingham lubricant,” *Tribology International*, vol. 41, no. 12, pp. 1190–1204, 2008.

[40] C. Dorier and J. Tichy, “Behavior of a Bingham-like in lubrication flows,” *Journal of Non-Newtonian Fluid Mechanics*, vol. 45, no. 3, pp. 291–310, 1992.

[41] S. G. Lampaert and R. A. van Ostayen, “Lubrication theory for bingham plastics,” *Tribology International*, vol. 147, p. 106160, 2020.

[42] B. J. Hamrock, *Fundamental of Fluid Film Lubrication Second Edition.* CRC Press, 2004.

[43] M. Rahman, Z. C. Ong, S. Julai, M. M. Ferdaus, and R. Ahamed, “A review of advances in magnetorheological dampers: their design optimization and applications,” *Journal of Zhejiang University: Science A*, vol. 18, pp. 991–1010, dec 2017.

[44] M. R. Jolly, J. W. Bender, and J. D. Carlson, “Properties and Applications of Commercial Magnetorheological Fluids,” *Journal of Intelligent Material Systems and Structures*, vol. 10, pp. 5–13, jan 1999.

[45] J. M. Guldbakke and J. Hesselbach, “Development of bearings and a damper based on magnetically controllable fluids,” *Journal of Physics Condensed Matter*, vol. 18, p. S2959, sep 2006.

[46] S. G. Lampaert, F. Quinci, and R. A. van Ostayen, “Rheological texture in a journal bearing with magnetorheological fluids,” *Journal of Magnetism and Magnetic Materials*, vol. 499, p. 166218, apr 2020.

[47] “Futek model lsb201 data sheet.” `https://media.futek.com/content/futek/files/pdf/productdrawings/lsb201.pdf`. accessed on 24-08-2023.

[48] M. Hemmatian, R. Sedaghati, and S. Rakheja, “Temperature dependency of magnetorheological fluids’ properties under varying strain amplitude and rate,” *Journal of Magnetism and Magnetic Materials*, vol. 498, 2020.

[49] X. Liu, Z. Shi, N. Mo, J. Zhao, and G. Yang, “Calculation and experiment of electromagnetic force of the axial AMB used in HTR-PM main helium blower prototype and its dual material selection method,” *Applied Computational Electromagnetics Society Journal*, vol. 34, no. 4, pp. 584–590, 2019.

[50] W. Litwin, "Experimental research on marine oil-lubricated stern tube bearing," *Proceedings of the Institution of Mechanical Engineers, Part J: Journal of Engineering Tribology*, vol. 233, pp. 1773–1781, nov 2019.

[51] COMSOL AB, "Comsol multiphysics® version 6.1." `https://www.comsol.com/`, 1986-2023.

[52] S. Alakhramsing, R. van Ostayen, and R. Eling, "Thermo-hydrodynamic analysis of a plain journal bearing on the basis of a new mass conserving cavitation algorithm," *Lubricants*, vol. 3, no. 2, pp. 256–280, 2015.

[53] J. C. Nicolas, "Hydrodynamic Journal Bearings - Types Characteristics And Applications," in *Mini Course Notes, 20th Annual Meeting, Vibration Institute*, pp. 81–100, 1996. Issue: July.

[54] W. C. Leung, W. A. Bullough, P. L. Wong, and C. Feng, "The effect of particle concentration in a magneto rheological suspension on the performance of a boundary lubricated contact," *Proceedings of the Institution of Mechanical Engineers, Part J: Journal of Engineering Tribology*, vol. 218, pp. 251–263, aug 2004.

[55] P. L. Wong, W. A. Bullough, C. Feng, and S. Lingard, "Tribological performance of a magneto-rheological suspension," *Wear*, vol. 247, pp. 33–40, jan 2001.

[56] B. A. Gecim, "Non-Newtonian Effects of Multigrade Oils on Journal Bearing Performance," *Tribology Transactions*, vol. 33, pp. 384–394, Jan. 1990. Publisher: Taylor & Francis.

[57] M. M. Khonsari and E. R. Booser, *Applied tribology : bearing design and lubrication.* Hoboken, NJ: John Wiley & Sons Inc., 2017.

[58] A. A. Milne, "A theory of rheodynamic lubrication lubrication and wear division: Lubrication and wear division," *Kolloid-Zeitschrift*, vol. 139, pp. 96–101, Nov. 1954.

[59] O. Pinkus and B. Sternlicht, *Theory of Hydrodynamic Lubrication.* McGraw-Hill, 1961.

[60] R. B. Bird, G. C. Dai, and B. J. Yarusso, "The Rheology and Flow of Viscoplastic Materials," *Reviews in Chemical Engineering*, vol. 1, pp. 1–70, Mar. 1983.

[61] R. B. Bird, *Dynamics of Polymeric Liquids, Volume 1: Fluid Mechanics.* Wiley, May 1987.

[62] R. K. Dang, D. Goyal, A. Chauhan, and S. S. Dhami, "Effect of non-newtonian lubricants on static and dynamic characteristics of journal bearings," *Materials Today: Proceedings*, vol. 28, pp. 1345–1349, Jan. 2020.

[63] F. Bouyahia, M. Hajjam, M. El Khlifi, and D. Souchet, "Three-dimensional non-Newtonian lubricants flows in sector-shaped, tilting-pads thrust bearings," *Proceedings of the Institution of Mechanical Engineers, Part J: Journal of Engineering Tribology*, vol. 220, no. 4, pp. 375–384, 2006. Publisher: Professional Engineering Publishing.

[64] J. J. Kauzlarich and J. A. Greenwood, “Elastohydrodynamic Lubrication With Herschel-Bulkley Model Greases,” *A S L E Transactions*, vol. 15, pp. 269–277, Jan. 1972.

[65] X. Wang, H. Li, M. Li, H. Bai, G. Meng, and H. Zhang, “Dynamic characteristics of magnetorheological fluid lubricated journal bearing and its application to rotor vibration control,” *Journal of Vibroengineering*, vol. 17, pp. 1912–1928, June 2015. Number: 4 Publisher: JVE International Ltd.

[66] S. Wada, H. Hayashi, and K. Haga, “Behavior of a Bingham Solid in Hydrodynamic Lubrication - 1. General Theory.,” *Bull JSME*, vol. 16, no. 92, pp. 422–431, 1973.

[67] S. Wada, H. Hayashi, and K. Haga, “Behavior of a Bingham Solid in Hydrodynamic Lubrication - 2. Application To Step Bearing.,” *Bull JSME*, vol. 16, no. 92, pp. 432–440, 1973.

[68] S. Wada, H. Hayashi, and K. Haga, “Behavior of a Bingham Solid in Hydrodynamic Lubrication : Part 3, Application to Journal Bearing,” *Bulletin of JSME*, vol. 17, no. 111, pp. 1182–1191, 1974.

[69] J. A. Tichy, “Hydrodynamic lubrication theory for the Bingham plastic flow model,” *Journal of Rheology*, vol. 35, no. 4, pp. 477–496, 1991.

[70] D. Dowson, “A generalized Reynolds equation for fluid-film lubrication,” *International Journal of Mechanical Sciences*, vol. 4, no. 2, pp. 159–170, 1962.

[71] M. E. Khlifi, D. Souchet, M. Hajjam, and F. Bouyahia, “Numerical Modeling of Non-Newtonian Fluids in Slider Bearings and Channel Thermohydrodynamic Flow,” *J. Tribol.*, vol. 129, no. July, pp. 695–699, 2007.

[72] J. H. Kim and A. A. Seireg, “Thermohydrodynamic Lubrication Analysis Incorporating Bingham Rheological Model,” *Journal of Tribology*, vol. 122, pp. 137–146, Dec. 1998.

[73] S. C. Sharma and S. K. Yadav, “Performance analysis of a fully textured hybrid circular thrust pad bearing system operating with non-Newtonian lubricant,” *Tribology International*, vol. 77, pp. 50–64, Sept. 2014.

[74] S. C. Sharma and C. B. Khatri, “Electro-rheological fluid lubricated textured multi-lobe hole-entry hybrid journal bearing system,” *Journal of Intelligent Material Systems and Structures*, vol. 29, no. 8, pp. 1600–1619, 2018.

[75] I. A. Frigaard and C. Nouar, “On the usage of viscosity regularisation methods for visco-plastic fluid flow computation,” *Journal of Non-Newtonian Fluid Mechanics*, vol. 127, pp. 1–26, Apr. 2005.

[76] S. G. E. Lampaert and R. A. J. van Ostayen, “Lubrication theory for Bingham plastics,” *Tribology International*, vol. 147, p. 106160, July 2020.

[77] H. Urreta and G. Aguirre, “Hydrostatic journal bearing and pressurized seals for machine tool spindles based on active magnetic fluids: magnetorheological fluids and ferrofluids,” in *Proceedings of the 18th international conference of the European Society for Precision Engineering and Nanotechnology*, p. 530, 2018.

[78] J. B. Shukla, S. Kumar, and P. Chandra, “Generalized reynolds equation with slip at bearing surfaces: Multiple-layer lubrication theory,” *Wear*, vol. 60, pp. 253–268, May 1980.

[79] Wolfram Research, Inc., “Mathematica, Version 13.3.” `https://www.wolfram.com/mathematica/`, 2023.

[80] F. W. Olver, D. W. Lozier, R. Boisvert, and C. W. Clark, “The NIST Handbook of Mathematical Functions,” *NIST*, May 2010.

[81] L. G. Cabral-Rosetti and M. A. Sanchis-Lozano, “Generalized Hypergeometric Functions and the Evaluation of Scalar One-loop Integrals in Feynman Diagrams,” Nov. 1998.

[82] M. N. Barber and B. W. Ninham, *Random and restricted walks: theory and applications.* No. vol. 10 in Mathematics and its applications, New York: Gordon and Breach, 1970.

[83] F. D. Colavecchia and G. Gasaneo, “f1: a code to compute Appell’s $F1$ hypergeometric function,” *Computer Physics Communications*, vol. 157, pp. 32–38, Feb. 2004.

[84] W. N. Bailey, 1893, *Generalized hypergeometric series.* Cambridge tracts in mathematics and mathematical physics; no. 32, London: Cambridge University Press, 1935.

[85] E. W. Weisstein, “Appell hypergeometric function. From MathWorld—A Wolfram Web Resource.” `https://mathworld.wolfram.com/AppellHypergeometricFunction.html`. accessed on 22-04-2024.

[86] The MathWorks Inc., “Matlab version: 9.11.0 (r2021b).” `https://www.mathworks.com`, 2021.

[87] C. Arcadia, “Bivariate appel hypergeometric function of the first kind.” `https://www.mathworks.com/matlabcentral/fileexchange/61066-bivariate-appel-hypergeometric-function-of-the-first-kind`, 2017. accessed on 29-04-2024.

[88] G. H. G. van der Meer, “Appell f1 hypergeometric function.” `https://nl.mathworks.com/matlabcentral/fileexchange/174390-appell-f1-hypergeometric-function`, 2024. accessed on 24-10-2024.

[89] D. E. Brewe, “Theoretical Modeling of the Vapor Cavitation in Dynamically Loaded Journal Bearings,” *Journal of Tribology*, vol. 108, pp. 628–637, Oct. 1986.

[90] H. G. Elrod, “A Cavitation Algorithm,” *Journal of Lubrication Technology*, vol. 103, pp. 350–354, July 1981.

[91] B. Jakobsson and L. Floberg, *The finite Journal Bearing, considering vaporization*. Chalmers tekniska högskola, Göteborg: Gumperts Förlag, 1957. OCLC: 718857301.

[92] M. Abramowitz, I. A. Stegun, and United States National Bureau of Standards, *Handbook of mathematical functions with formulas, graphs, and mathematical tables*. No. 55 in Applied mathematics series, Washington, D.C.: National Bureau of Standards, 1964.

[93] C. S. Maurya and C. Sarkar, "Magnetorheological fluids: a comprehensive review of operational modes and performance under varied circumstances," *Rheologica Acta*, vol. 63, pp. 765–785, Dec. 2024.

[94] K. Nagaya, A. Suda, H. Yoshida, Y. Ohashi, H. Ogiwara, and R. Wakamatsu, "MR fluid viscous coupling and its torque delivery control," *Tribology International*, vol. 40, pp. 89–97, Jan. 2007.

[95] F. Bucchi, P. Forte, F. Frendo, and R. Squarcini, "A magnetorheological clutch for efficient automotive auxiliary device actuation," *Fracture and Structural Integrity*, vol. 7, no. 23, pp. 62–74, 2013. Number: 23.

[96] M. Asadi Varnusfaderani, M. Irannejad Parizi, M. Hemmatian, and A. Ohadi, "Experimental parameters identification of a flexible rotor system equipped with smart magneto-rheological bearing," *Mechatronics*, vol. 87, p. 102880, Nov. 2022.

[97] L. Wu, X. Dong, and B. Yang, "Performance enhancement of a rotary magnetorheological damper induced by needle roller structure," *Tribology International*, vol. 201, p. 110204, Jan. 2025.

[98] R. K. Singh and C. Sarkar, "Tribological and braking performance study of additive-based MR fluids in shear and hybrid mode using MR drum brake," *Tribology International*, vol. 192, p. 109284, Apr. 2024.

[99] P. Turabimana and J. W. Sohn, "Optimal Design and Control Performance Evaluation of a Magnetorheological Fluid Brake Featuring a T-Shape Grooved Disc," *Actuators*, vol. 12, p. 315, Aug. 2023. Number: 8 Publisher: Multidisciplinary Digital Publishing Institute.

[100] I. F. Santos, "Controllable Sliding Bearings and Controllable Lubrication Principles—An Overview," *Lubricants*, vol. 6, p. 16, Mar. 2018. Number: 1 Publisher: Multidisciplinary Digital Publishing Institute.

[101] L. Breńkacz, L. Witanowski, M. Drosińska-Komor, and N. Szewczuk-Krypa, "Research and applications of active bearings: A state-of-the-art review," *Mechanical Systems and Signal Processing*, vol. 151, p. 107423, Apr. 2021.

[102] W. Ochoński, "Sliding bearings lubricated with magnetic fluids," *Industrial Lubrication and Tribology*, vol. 59, pp. 252–265, Jan. 2007. Publisher: Emerald Group Publishing Limited.

[103] W. Horak, J. Salwiński, and M. Szczęch, “Analysis of the influence of selected factors on the capacity of thrust sliding bearings lubricated with magnetic fluids,” *Tribologia*, vol. 274, no. 4, pp. 33–38, 2017.

[104] S. G. E. Lampaert and R. A. J. van Ostayen, “Experimental results on a hydrostatic bearing lubricated with a magnetorheological fluid,” *Current Applied Physics*, vol. 19, pp. 1441–1448, Dec. 2019.

[105] G. H. G. van der Meer, F. Quinci, W. Litwin, M. Wodtke, and R. A. J. van Ostayen, “Experimental comparison of the transition speed of a hydrodynamic journal bearing lubricated with oil and magnetorheological fluid,” *Tribology International*, vol. 189, p. 108976, Nov. 2023.

[106] S. Li, S. Xiu, W. Song, C. Sun, and H. Yang, “Research on the wear characteristics of magnetorheological fluid in sealing interface considering the interaction between surface roughness and magnetic particles,” *Tribology International*, vol. 185, p. 108496, July 2023.

[107] M. M. Khonsari and E. R. Booser, “Effect of Contamination on the Performance of Hydrodynamic Bearings,” *Proceedings of the Institution of Mechanical Engineers, Part J: Journal of Engineering Tribology*, vol. 220, pp. 419–428, May 2006.

[108] G. K. Nikas, “A state-of-the-art review on the effects of particulate contamination and related topics in machine-element contacts,” *Proceedings of the Institution of Mechanical Engineers, Part J: Journal of Engineering Tribology*, vol. 224, pp. 453–479, May 2010.

[109] W. Dmochowski, J. Duchowski, and G. Collins, “Experimental Evaluation of Filtration Requirements for Journal Bearings Operating Under Different Contaminant Levels,” *Lubrication Engineering*, vol. 58, June 2002.

[110] R. Elwell, “Foreign Object Damage in Journal Bearings,” *Lubrication Engineering*, vol. 34, pp. 187–192, 1978.

[111] V. Wikström, E. Höglund, and R. Larsson, “Wear of bearing liners at low speed rotation of shafts with contaminated oil,” *Wear*, vol. 162-164, pp. 996–1001, 1993.

[112] J. L. Xuan, I. T. Hong, and E. C. Fitch, “Hardness Effect on Three-Body Abrasive Wear Under Fluid Film Lubrication,” *Journal of Tribology*, vol. 111, pp. 35–40, Jan. 1989.

[113] W.-L. Song, S.-B. Choi, J.-Y. Choi, and C.-H. Lee, “Wear and Friction Characteristics of Magnetorheological Fluid under Magnetic Field Activation,” *Tribology Transactions*, vol. 54, pp. 616–624, July 2011. Publisher: Taylor & Francis _eprint: https://doi.org/10.1080/10402004.2011.584365.

[114] Z. D. Hu, H. Yan, H. Z. Qiu, P. Zhang, and Q. Liu, “Friction and wear of magnetorheological fluid under magnetic field,” *Wear*, vol. 278-279, pp. 48–52, Mar. 2012.

[115] A. J. F. Bombard and J. de Vicente, "Boundary lubrication of magnetorheological fluids in PTFE/steel point contacts," *Wear*, vol. 296, pp. 484–490, Aug. 2012.

[116] K. Shahrivar, A. L. Ortiz, and J. de Vicente, "A comparative study of the tribological performance of ferrofluids and magnetorheological fluids within steel–steel point contacts," *Tribology International*, vol. 78, pp. 125–133, Oct. 2014.

[117] Z. Hu, H. Zhang, H. Zhao, and D. Wang, "The friction and Wear behavior of Silicon oil-based Magnetorheological fluid with Solid lubricant," *Journal of Physics: Conference Series*, vol. 2174, p. 012029, Jan. 2022. Publisher: IOP Publishing.

[118] S. Zhang, Z. Long, and X. Yang, "Lubrication performance of magnetorheological fluid-lubricated rubber stern bearing test ring," *Journal of the Brazilian Society of Mechanical Sciences and Engineering*, vol. 43, p. 56, Jan. 2021.

[119] Liquids Research Ltd., "Magneto-rheological fluids.pdf." `https://liquidsresearch.com/en-GB/document_download-58.aspx`. accessed on 27-11-2024.

[120] C. A. Schneider, W. S. Rasband, and K. W. Eliceiri, "NIH Image to ImageJ: 25 years of image analysis," *Nature Methods*, vol. 9, pp. 671–675, July 2012. Publisher: Nature Publishing Group.

[121] C. H. Li and P. K. S. Tam, "An iterative algorithm for minimum cross entropy thresholding," *Pattern Recognition Letters*, vol. 19, pp. 771–776, June 1998.

[122] C. Dong, C. Yuan, X. Bai, Y. Yang, and X. Yan, "Study on wear behaviours for NBR/stainless steel under sand water-lubricated conditions," *Wear*, vol. 332-333, pp. 1012–1020, May 2015.

[123] M.-x. Shen, B. Li, S. Li, G.-y. Xiong, D.-h. Ji, and Z.-n. Zhang, "Effect of particle concentration on the tribological properties of NBR sealing pairs under contaminated water lubrication conditions," *Wear*, vol. 456-457, p. 203381, Sept. 2020.

[124] G. Hu, J. Ma, G. Yuan, K. Shen, and H. Wang, "Effect of hard particles on the tribological properties of hydrogenated nitrile butadiene rubber under different lubricated conditions," *Tribology International*, vol. 169, p. 107457, May 2022.

[125] R. Zuo, G. Wang, G. Hu, S. Zhao, and G. Wei, "Tribological properties of hydrogenated nitrile rubber in confrontation with hard particles under different axial loads," *Tribology International*, vol. 153, p. 106649, Jan. 2021.

[126] G. van der Meer and R. van Ostayen, "Investigating Film Thickness and Friction of an MR-Lubricated Journal Bearing," *Lubricants*, vol. 13, p. 171, Apr. 2025. Number: 4 Publisher: Multidisciplinary Digital Publishing Institute.

[127] S.-B. Choi, "Thermal Conductivity and Temperature Dependency of Magnetorheological Fluids and Application Systems—A Chronological Review," *Micromachines*, vol. 14, p. 2096, Nov. 2023. Number: 11 Publisher: Multidisciplinary Digital Publishing Institute.

[128] H. Eshgarf, A. Ahmadi Nadooshan, and A. Raisi, "An overview on properties and applications of magnetorheological fluids: Dampers, batteries, valves and brakes," *Journal of Energy Storage*, vol. 50, p. 104648, June 2022.

[129] D. J. Klingenberg, "Magnetorheology: Applications and challenges," *AIChE Journal*, vol. 47, no. 2, pp. 246–249, 2001.

[130] J. Zapoměl and P. Ferfecki, "A new concept of a hydrodynamic bearing lubricated by composite magnetic fluid for controlling the bearing load capacity," *Mechanical Systems and Signal Processing*, vol. 168, p. 108678, Apr. 2022.

[131] D. A. Bompos and P. G. Nikolakopoulos, "Rotordynamic Analysis of a Shaft Using Magnetorheological and Nanomagnetorheological Fluid Journal Bearings," *Tribology Transactions*, vol. 59, pp. 108–118, Jan. 2016. Publisher: Taylor & Francis _eprint: https://doi.org/10.1080/10402004.2015.1050137.

[132] S. C. Sharma and A. Kumar, "On the behaviour of roughened conical hybrid journal bearing system operating with MR lubricant," *Tribology International*, vol. 156, p. 106824, Apr. 2021.

[133] S. A. Vaziri, M. Norouzi, P. Akbarzadeh, K. C. Kim, and M. Kim, "Thermohydrodynamic analysis of magnetorheological conical bearings with conjugated heat transfer," *Scientific Reports*, vol. 14, p. 20596, Sept. 2024. Publisher: Nature Publishing Group.

[134] N. C. Moles, *Actively Controllable Hydrodynamic Journal Bearing Design Using Magnetorheological Fluids*. PhD thesis, University of Akron, 2015.

[135] M. Wodtke, W. Litwin, G. van der Meer, and R. van Ostayen, "Wear tests of hydrodynamic journal bearings lubricated with magnetorheological fluid," *Wear*, p. 206404, Oct. 2025.

[136] Anton Paar Netherlands B.V., "The modular compact rheometer series." `https://www.mtbrandao.com/files/products/MCR_1.pdf`. accessed on 7 April 2025.

[137] F. Zschunke, R. Rivas, and P. O. Brunn, "Temperature Behavior of Magnetorheological Fluids," *Applied Rheology*, vol. 15, pp. 116–121, Apr. 2005. Publisher: De Gruyter Open Access.

[138] G. Mörée and M. Leijon, "Review of Hysteresis Models for Magnetic Materials," *Energies*, vol. 16, p. 3908, Jan. 2023. Number: 9 Publisher: Multidisciplinary Digital Publishing Institute.

[139] L. Petrescu, E. Cazacu, and C. Petrescu, "Sigmoid functions used in hysteresis phenomenon modeling," in *2015 9th International Symposium on Advanced Topics in Electrical Engineering (ATEE)*, pp. 521–524, May 2015. ISSN: 2068-7966.

[140] G. H. G. van der Meer and R. A. J. van Ostayen, "Efficient solution method for the Reynolds equation with Herschel–Bulkley fluids," *Tribology International*, vol. 204, p. 110460, Apr. 2025.

[141] W. Litwin, *Water-Lubricated Journal Bearings, Marine Applications, Design, and Operational Problems and Solutions.* Elsevier, Aug. 2023.

[142] K. Sahu, S. C. Sharma, and N. Ram, "Misalignment and Surface Irregularities Effect in MR Fluid Journal Bearing," *International Journal of Mechanical Sciences*, vol. 221, p. 107196, May 2022.

[143] T. Lohner, A. Ziegltrum, J. P. Stemplinger, and K. Stahl, "Engineering Software Solution for Thermal Elastohydrodynamic Lubrication Using Multiphysics Software," *Advances in Tribology*, vol. 2016, no. February, 2016.

[144] W. Hu and N. M. Wereley, "Behavior of MR fluids at high shear rate," *International Journal of Modern Physics B*, vol. 25, no. 7, pp. 979–985, 2011. ISBN: 0217979211058.

[145] X. Wang and F. Gordaninejad, "Study of magnetorheological fluids at high shear rates," *Rheologica Acta*, vol. 45, pp. 899–908, Aug. 2006.

[146] W. Litwin, "Properties comparison of rubber and three layer PTFE-NBR-bronze water lubricated bearings with lubricating grooves along entire bush circumference based on experimental tests," *Tribology International*, vol. 90, pp. 404–411, Oct. 2015.

[147] D. L. Cabrera, N. H. Woolley, D. R. Allanson, and Y. D. Tridimas, "Film pressure distribution in water-lubricated rubber journal bearings," *Proceedings of the Institution of Mechanical Engineers, Part J: Journal of Engineering Tribology*, vol. 219, no. 2, pp. 125–132, 2005.

[148] W. Litwin, "Water-lubricated bearings of ship propeller shafts - problems, experimental tests and theoretical investigations," *Polish Maritime Research*, vol. 16, pp. 41–49, Mar. 2010.

[149] J. Bouyer and M. Fillon, "An Experimental Analysis of Misalignment Effects on Hydrodynamic Plain Journal Bearing Performances," *Journal of Tribology*, vol. 124, pp. 313–319, July 2001.

[150] I. Pierre, J. Bouyer, and M. Fillon, "Thermohydrodynamic Behavior of Misaligned Plain Journal Bearings: Theoretical and Experimental Approaches," *Tribology Transactions*, vol. 47, pp. 594–604, Oct. 2004. Publisher: Taylor & Francis.

[151] J. Sun, M. Deng, Y. Fu, and C. Gui, "Thermohydrodynamic Lubrication Analysis of Misaligned Plain Journal Bearing With Rough Surface," *Journal of Tribology*, vol. 132, Dec. 2009.

[152] J. Y. Jang and M. M. Khonsari, "On the Characteristics of Misaligned Journal Bearings," *Lubricants*, vol. 3, pp. 27–53, Mar. 2015. Number: 1 Publisher: Multidisciplinary Digital Publishing Institute.

[153] F. Lv, C. Jiao, D. Zou, N. Ta, and Z.-s. Rao, "Analysis of misaligned water-lubricated polymer bearing with axial grooves," *Industrial Lubrication and Tribology*, vol. 71, pp. 411–419, Nov. 2018. Publisher: Emerald Publishing Limited.

[154] W. V. Smith, “Material selection criteria for water lubrication,” *Wear*, vol. 25, pp. 139–153, Aug. 1973.

[155] S. Hother-Lushington, “Water lubricated bearings,” *Tribology International*, vol. 9, pp. 257–260, Dec. 1976. Publisher: Elsevier.

[156] Z. Zou, H. Zhang, C. Liao, N. Wang, and S.-B. Choi, “Hydrodynamic behaviors of settled magnetorheological fluid redispersion under active dispersing mechanism: simulation and experiment,” *Smart Materials and Structures*, vol. 31, p. 097001, Aug. 2022. Publisher: IOP Publishing.

[157] S. Odenbach, “Magnetoviscous and viscoelastic effects in ferrofluids,” *International Journal of Modern Physics B*, vol. 14, no. 16, pp. 1615–1631, 2000.

[158] W. Huang and X. Wang, “Ferrofluids lubrication: a status report,” *Lubrication Science*, vol. 28, no. 1, pp. 3–26, 2016. _eprint: https://onlinelibrary.wiley.com/doi/pdf/10.1002/ls.1291.

[159] N. S. Patel, D. P. Vakharia, G. M. Deheri, and H. C. Patel, “Experimental performance analysis of ferrofluid based hydrodynamic journal bearing with different combination of materials,” *Wear*, vol. 376-377, pp. 1877–1884, Apr. 2017.

[160] C. Moler, “The tetragamma function and numerical craftsmanship.” `https://nl.mathworks.com/company/technical-articles/the-tetragamma-function-and-numerical-craftsmanship.html`, 2002. Accessed: 24-03-2025.

[161] F. D. Colavecchia, G. Gasaneo, and J. E. Miraglia, “Numerical evaluation of Appell’s F1 hypergeometric function,” *Computer Physics Communications*, vol. 138, pp. 29–43, July 2001.

[162] V. Sahai and A. Verma, “DERIVATIVES OF APPELL FUNCTIONS WITH RESPECT TO PARAMETERS,” *J. Inequal. Spec. Funct.*, vol. 6, pp. 2217–4303, Jan. 2015.

[163] A. Garcia and M. Mehrubeoglu, “Switchable Magnets as a Power-Efficient Alternative for Electromagnets in a Mobile Robotic System,” in *2020 IEEE Green Technologies Conference(GreenTech)*, pp. 212–216, Apr. 2020. ISSN: 2166-5478.

[164] E. Ronaes, A. Hunt, and H. HosseinNia, “Remnant Magnetisation State Control for Positioning of a Hybrid Tunable Magnet Actuator,” *Energies*, vol. 16, p. 4548, June 2023.

[165] S. G. Viëtor, J. W. Spronck, and S. H. HosseinNia, “Tunable Magnets: modeling and validation for dynamic and precision applications,” 2022. Publisher: arXiv Version Number: 1.

Acknowledgments

Even though the PhD is an individual project, the end result would not have been possible without the aid and assistance of many others. I would like to use this opportunity to express my thanks to all of those I worked or spent time with during the last four years.

First of all I want to thank my promotors Ron and Just. In particular I would like to thank Ron, my daily supervisor, for giving me the opportunity to start this PhD in the first place. I have learned a lot during these past four years, in no small part due to your support and guidance along the way.

During the PhD it was possible to cooperate intensively with the company AEGIR-Marine, and I want to thank the people at AEGIR for this collaboration and for all of the aid I received during my research. I want to thank Federico in particular for the (hands-on) support and advice during the first 2.5 years, you continuously pushed me towards excellence. I also want to thank Dennis for the weekly group meetings and the support during the final year.

Next I want to thank Michał and Wojciech from the university of Gdańsk for the collaboration during this project, I really enjoyed working with you and listening to all of your stories. Thanks as well for inviting me to your university and for showing me around the beautiful city of Gdańsk, I'd love to visit the city, and Poland in general, again some day.

A large part of the experimental research conducted for this project was performed in the labs of the department of PME. For that reason I want to thank everyone from lab support: Rob, Patrick, Alex, Bradley, Gideon, and Spiridon, thank you for all of the practical assistance you gave me in trying to realise that enormous setup (enormous for the Precision and Microsystems engineering department).

I would like to thank the students whom I supervised during their masterprojects. Thobias, Martijn, Jonatan, Daan, I liked discussing with you during our weekly meetings and brainstorming about your projects. Your work challenged me as well, and has been a big contribution to this PhD journey.

Many thanks to all of my colleagues from PME, and especially from the MSD group, for the great atmosphere at the department. Thank you for all of the discussions about our projects, and for the fun trips, conferences, and events.

Als laatste wil ik graag mijn ouders bedanken, zonder jullie vertrouwen en steun was deze PhD niet mogelijk geweest.

Gerben
Alphen aan den Rijn, April 2025

Curriculum Vitæ

Gerben Hugo Geert van der Meer

June 15, 1997	Born in Leiderdorp, The Netherlands
2009-2015	**VWO** - Natuur & Techniek Groene Hart Lyceum, Alphen aan den Rijn, The Netherlands
2015-2018	**BSc.** Mechanical Engineering (Werktuigbouwkunde) Delft University of Technology, Delft, The Netherlands *Degree Cum Laude*
	Minor Physics
2018-2020	**MSc.** Mechanical Engineering Delft University of Technology, Delft, The Netherlands *Specialisation: Mechatronic System Design* *Topic: Modelling self-healing magnetic textures in hydrodynamic bearings* *Degree Cum Laude*
2021-2025	**PhD.** Mechanical Engineering / Tribology Delft University of Technology, Delft, The Netherlands *Topic: Hydrodynamic Lubrication with Magnetorheological Fluids* *Promotors: Dr. ir. R.A.J. van Ostayen & Prof. dr. ir. J.L. Herder*

List of Publications

Journal Articles

🗎 4. G. van der Meer and R. van Ostayen, ‘Investigating Film Thickness and Friction of an MR-Lubricated Journal Bearing’, Lubricants, vol. 13, no. 4, Art. no. 4, Apr. 2025, doi:10.3390/lubricants13040171.

🗎 3. M. Wodtke, W. Litwin, G. van der Meer, and R. van Ostayen, ’Wear tests of hydrodynamic journal bearings lubricated with magnetorheological fluid’, Wear, p. 206404, Oct. 2025, doi:10.1016/j.wear.2025.206404

🗎 2. G. H. G. van der Meer and R. A. J. van Ostayen, ‘Efficient solution method for the Reynolds equation with Herschel–Bulkley fluids’, Tribology International, vol. 204, p. 110460, Apr. 2025, doi:10.1016/j.triboint.2024.110460.

🗎 1. G. H. G. van der Meer, F. Quinci, W. Litwin, M. Wodtke, and R. A. J. van Ostayen, ‘Experimental comparison of the transition speed of a hydrodynamic journal bearing lubricated with oil and magnetorheological fluid’, Tribology International, vol. 189, p. 108976, Nov. 2023, doi:10.1016/j.triboint.2023.108976.

Conference Presentations

7. Poster presentation. NORDTRIB - Nordic Tribology Symposium. Copenhagen 2024.
6. Oral presentation. Tribology of the Low Countries. Enschede 2024.
5. Oral presentation. COMSOL Conference. Munich 2023
4. Oral presentation. 22nd Pprime Workshop. Poitiers 2023
3. Oral presentation. 48th Leeds-Lyon Symposium on Tribology. Leeds 2023.
2. Oral presentation. 7th World Tribology Congress. Lyon 2022.
1. Oral presentation. Tribology of the Low Countries. Gent 2022.

🗎 Included in this thesis.

MSc thesis projects supervised

- T.L. van Kuik. The transition from structures to textures in magnetorheological fluids. 2022.
- M.J. Loonen. Demonstrator setup for semi-active control of a hydrodynamic journal bearing lubricated with magnetorheological fluid. 2024.
- J. Naaktgeboren. Topic: Comparing the influences of textures, surface slip, and MR lubrication on hydrodynamic thrust bearing performance. *Thesis not yet finished.*
- D. C. Boersema. Topic: Designing a high shear rate capillary rheometer for magnetorheological fluids. *Thesis not yet finished.*

BSc thesis projects supervised

- A. Aziz, W.D. Remmelzwaan, J.C.T.F. Geerlofs, R. Geerts. Modifying magnetorheological fluids for use in hydrodynamic bearings used by ships. 2023.

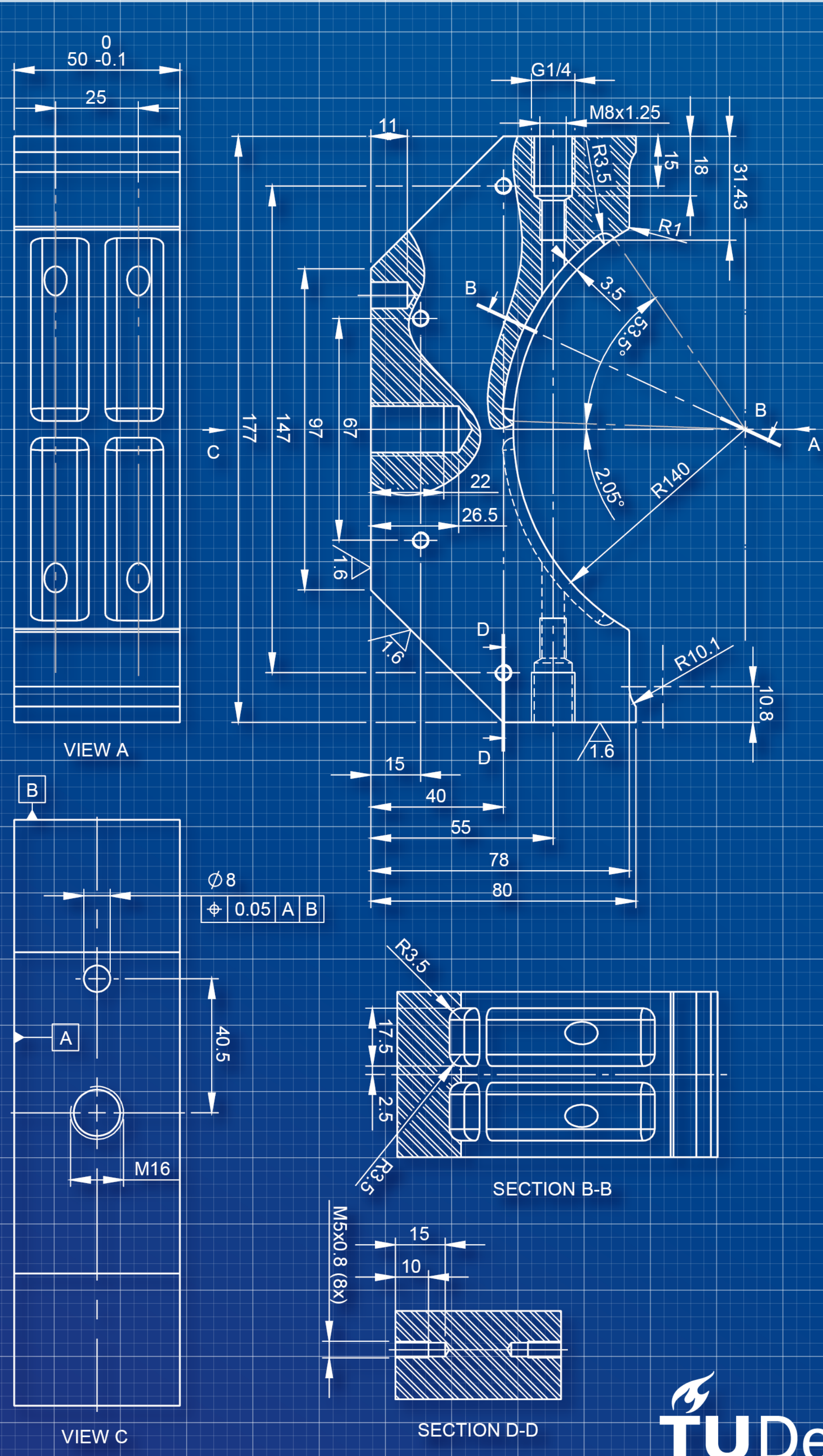
0
50 -0.1
25
VIEW A
B
A
C
VIEW C
∅8
⌖ 0.05 A B
40.5
M16
G1/4
M8x1.25
11
R3.5
15
18
31.43
R1
3.5
B
53.5°
B
A
177
147
97
67
2.05°
R140
22
26.5
1.6
1.6
D
R10.1
10.8
1.6
D
15
40
55
78
80
R3.5
17.5
2.5
R3.5
SECTION B-B
M5x0.8 (8x)
15
10
SECTION D-D

TUDelft